THE DYNAMICS AND PREDICTABILITY OF TROPICAL CYCLONES

A Dissertation

by

JASON ALLEN SIPPEL

Submitted to the Office of Graduate Studies of
Texas A&M University
in partial fulfillment of the requirements for the degree of

DOCTOR OF PHILOSOPHY

December 2008

Major Subject: Atmospheric Sciences

THE DYNAMICS AND PREDICTABILITY OF TROPICAL CYCLONES

A Dissertation

by

JASON ALLEN SIPPEL

Submitted to the Office of Graduate Studies of
Texas A&M University
in partial fulfillment of the requirements for the degree of

DOCTOR OF PHILOSOPHY

Approved by:

Chair of Committee,	Fuqing Zhang
Committee Members,	Larry D. Carey
	Craig C. Epifanio
	Jianhua Huang
	John W. Nielsen-Gammon
Head of Department,	Kenneth P. Bowman

December 2008

Major Subject: Atmospheric Sciences

ABSTRACT

The Dynamics and Predictability of Tropical Cyclones. (December 2008)

Jason Allen Sippel, B.S., Texas A&M University;
M.S., Texas A&M University
Chair of Advisory Committee: Dr. Fuqing Zhang

Through methodology unique for tropical cyclones in peer-reviewed literature, this study explores how the dynamics of moist convection affects the predictability of tropical cyclogenesis. Mesoscale models are used to perform short-range ensemble forecasts of a non-developing disturbance in 2004 and Hurricane Humberto in 2007; both of these cases were highly unpredictable.

Taking advantage of discrepancies between ensemble members in short-range ensemble forecasts, statistical correlation is used to pinpoint sources of error in forecasts of tropical cyclone formation and intensification. Despite significant differences in methodology, storm environment and development, it is found in both situations that high convective instability (CAPE) and mid-level moisture are two of the most important factors for genesis. In the gulf low, differences in CAPE are related to variance in quasi-geostrophic lift, and in Humberto the differences are related to the degree of interaction between the cyclone and a nearby front. Regardless of the source of CAPE variance, higher CAPE and mid-level moisture combine to yield more active initial convection and more numerous and strong vortical hot towers (VHTs), which incrementally contribute to a stronger vortex. In both cases, strength differences between ensemble members are further amplified by differences in convection that are related to oceanic heat fluxes. Eventually the WISHE mechanism results in even larger ensemble spread, and in the case of Humberto, uncertainty related to the time of landfall drives spread even higher.

It is also shown that initial condition differences much smaller than current analysis error can ultimately control whether or not a tropical cyclone forms. Furthermore, even smaller differences govern how the initial vortex is built. Differences in maximum winds and/or vorticity vary nonlinearly with initial condition differences and depend on the timing and intensity of small mesoscale features such as VHTs and cold pools.

Finally, the strong sensitivity to initial condition differences in both cases exemplifies the inherent uncertainties in hurricane intensity prediction. This study illustrates the need for implementing advanced data analysis schemes and ensemble prediction systems to provide more accurate and event-dependent probabilistic forecasts.

ACKNOWLEDGEMENTS

Of course I have a lot of acknowledgements, but before I get started I have a bit of an anecdote. I feel compelled to share this because it's one of the best things that happened to me in the past five years, and it's a direct result of my employment under Dr. Fuqing Zhang. The story begins when I first started working for Fuqing. As many people know, Fuqing and I did not get along for the first year and a half that I worked for him. I consistently frustrated him, and he consistently frustrated me, and I was convinced that he was to blame. After about a year and a half of this, I was worn out. Then, out of the blue, the Lord revealed to me that the problem wasn't with Fuqing, but with me. Quite simply, the reason why Fuqing and I weren't getting along was because I didn't want to be told what to do. I had discovered that I was not immune to man's most common flaw, which is pride. Now considering my faith and seeing as how pride is implicitly something Christ spoke against day in and day out, it was quite humbling for me to come face to face with my own struggle with it. Nevertheless, that discovery has led to a transformation of my relationship with God and everyone else around me, including Fuqing. I think we have had a good to excellent working relationship since that point. So I thank the Lord for bringing me to this point and under Fuqing's authority, and I sincerely thank Fuqing for being an instrument of this change.

In addition, I want to acknowledge Fuqing for his guidance and direction as an advisor and for his contribution to the ideas and work that will be shown today. I also thank my committee for their guidance, and in particular John Nielsen-Gammon, who

served as my master's advisor. In Fuqing's absence during much of the last year of my dissertation, I was fortunate to be able to go down the hall to John's office and have a number of lengthy conversations with him about my results. I also thank my peers and office mates, in particular Ellie Meng and Yonghui Weng. Ellie taught me much of what I know about data assimilation, and conversations with her about research were always beneficial. Yonghui is largely the computational workhorse for our group, and I am especially grateful for his contribution of running the numerical simulations I needed, always in a timely fashion.

I also want to thank my family and friends for their support and encouragement. In particular, I thank my wife, Kelsey. She has been a tremendous support for me, and the Lord has truly blessed me in marriage to her.

TABLE OF CONTENTS

Page

CHAPTER Page

LIST OF FIGURES

FIGURE Page

FIGURE Page

FIGURE Page

LIST OF TABLES

CHAPTER I

INTRODUCTION

1.1. Motivation and objectives

Accurate predictions and forecast uncertainty estimations of tropical cyclones have enormous economic value, but today's operational predictions continue to have significant error and lack case-dependent uncertainty specification. With total hurricane-related losses topping $100 billion for the first time in 2005 (Pielke et al. 2005), demand is increasing for better accuracy, longer lead times and more precise warnings to minimize losses in hurricane preparation, evacuation and destruction. Though significant progress has been made in short-range track forecasts of tropical cyclones (Franklin 2005), forecasting cyclogenesis remains a challenge, and intensity forecast skill significantly lags that of track forecasts (e.g., DeMaria and Gross 2003; Emanuel 2003; DeMaria et al. 2005 and others). Thus, predictions of tropical cyclone formation, rapid intensification and decay remain particularly problematic (Houze et al 2007). In addition, more work is needed in order to assess and address sources of forecast uncertainty with tropical cyclones, which can ultimately lead to more precise watches and warnings.

This dissertation follows the style of *Journal of Atmospheric Sciences*.

This doctoral study seeks to investigate tropical cyclone formation and intensification with ensemble forecasts and sensitivity studies. The main objectives are to:

1. Document error growth in ensemble forecasts of both non-developing and developing tropical disturbances that were considered to be unpredictable by operational forecasters;
2. Use a previously developed statistical dynamic analysis technique to pinpoint precise mechanisms by which ensemble intensity spread (error) originates in forecasts of tropical cyclones;
3. Contribute to the general understanding of how tropical cyclones form and evolve; and
4. Determine possible effects of very minute changes to initial conditions on both the large and small scale evolution of a developing tropical cyclone;

In addition, some attention is paid to how forecast model error, in the form of cumulus parameterization, can affect forecasts of genesis and intensification. This work is the first extensive examination of the source of forecast error in tropical cyclone forecasts, and the techniques used here have never before been used on tropical cyclones.

1.2. Background

The primary reason for lagging intensity forecast skill appears to be deep moist convection. Warm-season precipitation, whose associated dynamics play a critical role in tropical cyclone genesis and intensification (e.g., Krishnamurti et al. 2005; Hendricks et al. 2004; Montgomery et al. 2006), generally remains the least accurate forecast element at all scales (Olson et al. 1995). Islam et al. (1993) and Snyder and Zhang (2003) demonstrated that errors grow rapidly at convective scales in weakly forced warm-season events, and such error growth in the presence of moist convection can significantly impact mesoscale predictability (Zhang et al. 2002, 2003, 2006a, 2007). Focusing on an extreme warm-season precipitation event, Zhang et al. (2006a) showed that undetectable random noise contaminates deterministic warm-season mesoscale forecasts within as few as 36 h. They concluded that this error, in combination with the error associated with inadequate initial analyses and forecast models, necessitates the use of probabilistic (ensemble) forecasts for mesoscale systems.

1.2.1. The usefulness of ensembles

Ensemble forecasts have indeed shown great potential for forecasting tropical cyclones. For example, some studies (e.g., Krishnamurti et al. 2000; Goerss 2000; Aberson 2001; Kumar et al. 2003; Williford et al. 2003; Weber 2003, 2005a, 2005b) have demonstrated that scalar position and intensity forecasts computed from multi-model ensembles are better than those from individual ensemble members. Additional work (e.g., Krishnamurti et al. 1997; Zhang and Krishnamurti 1999; Mackey and Krishnamurti 2001) has shown that the ensemble mean from an individual model can significantly improve upon deterministic forecasts of tropical cyclones.

Ensemble forecasts have also proven useful for investigating dynamics in a wide variety of atmospheric systems, and they might be useful for investigating and diagnosing the source of forecast uncertainty in tropical cyclogenesis. Zhang (2005) used ensembles to investigate a winter coastal cyclone and found that initially random perturbations evolved into coherent structures with spatial correlation (and covariance) between forecast variables. The correlation (covariance) was highly structured and found to be greatest in the region of strong cyclogenesis and along the upper level front. In another example, Hakim and Torn (2008) expanded upon the methods of Zhang (2005) to investigate the formation dynamics of a spring continental cyclone. They used the strong covariance between variables to infer relationships between the surface cyclone and preceding upper level disturbances and to predict changes in the cyclone strength given certain changes to the initial conditions. Finally, Hawblitzel et al. (2007) (hereafter H07) examined mesoscale convective vortex (MCV) formation dynamics and predictability using an ensemble. They found that small initial perturbations of model forecast variables resulted in large ensemble spread such that some members produced a very strong MCV while others produced no MCV at all. The ensemble members that produced a stronger MCV had more prolific convection as early as 24 h before the MCV developed. They concluded that the intimate dependence of every aspect of MCV development on moist convection largely explained the significant forecast uncertainty associated with this event.

1.2.2. Tropical cyclone formation: Observations and theory

The environments in which tropical cyclones form and intensify are well documented. Riehl (1954) recognized that tropical cyclones form from pre-existing disturbances over a relatively warm ocean, and Gray (1968, 1975) noted that developing disturbances are associated with large values of absolute vorticity, weak vertical wind shear, and mean upward motion. McBride and Zehr (1981) also found that tropical cyclones proceed from cloud clusters in an environment of high low-level vorticity, and Emanuel (1989) demonstrated the importance of deep moisture. In a more recent study, DeMaria et al. (2001) found that tropical cyclones are able to intensify when the 200-850 hPa zonal wind shear is less than 12.5 $m\ s^{-1}$. Other studies, such as Dunion and Velden (2004), have shown how regional phenomena (e.g., Saharan air layers in the Atlantic basin) can affect a number of the above factors and strongly modulate tropical cyclone formation and intensification. In addition to using measures of vertical wind shear, low-level vorticity, and deep moisture, National Oceanic and Atmospheric Administration (NOAA) Satellite Services Division (SSD) also uses cloud top temperature, a proxy for sustained deep convection, and vertical instability (NOAA SSD, 2008) to operationally predict tropical cyclone formation.

Emanuel (1986) and Rotunno and Emauel (1987) pioneered a theory in which tropical cyclones intensify from an initial vortex due to positive feedback between oceanic heat fluxes and surface wind speeds. In this theory, coined wind-induced surface heat exchange (WISHE; e.g., Emanuel et al. 1994), winds associated with a surface vortex enhance fluxes of sensible and latent heat from the ocean surface. This can lead to more vigorous convection, stronger diabatic heating, and a greater surface pressure deficit due to hydrostatic pressure falls in the vicinity of the convection. With a stronger surface pressure gradient, wind speeds and heat fluxes are higher, thus completing the loop.

While WISHE adequately describes cyclone maintenance and intensification, several requirements must be met for the process to proceed efficiently. In particular, an initial warm-core vortex of sufficient amplitude must be present. In addition, the vortex must be encompassed by ample deep-layer moisture (Rotunno and Emanuel 1987; Emanuel 1989). If sufficient moisture is not present through the mid-troposphere, then convection will have the propensity to produce cold convective downdrafts and stabilize the lower troposphere.

A number of observational studies have proposed mid-level vortex merger as a means to strengthen surface vorticity and initiate WISHE. Harr et al. (1996), Simpson et al. (1997), and Ritchie and Holland (1997) observed that MCVs that form in stratiform precipitation areas of tropical mesoscale convective systems sometimes merge to produce stronger, deeper, and wider circulations than those associated with any individual vortex. This process can enhance low-level vorticity and strengthen a tropical disturbance.

Hendricks et al. (2004) and Montgomery et al. (2006) presented a different view in which surface-based convection is key to generating the pre-WISHE tropical cyclone vortex. In this view, system-scale deep convection drives a toroidal circulation, which itself organizes the vortex angular momentum. Individual mesoscale, low-level vortices generated by intense sub-system-scale convection (coined vortical hot towers, or VHTs), can also enhance the genesis process during the pre-WISHE stage. Reasor et al. (2005) and Sippel et al. (2006) provided observational evidence of VHTs during tropical cyclogenesis, and the results of Tory et al. (2006a,b) support the idea that organized, surface based convection may be sufficient to generate a tropical cyclone vortex.

Finally, an alternative view sharing common ideas with each of the preceding theories focuses on the thermodynamics of the incipient vortex. In this view, first proposed by Bister and Emanuel (1997) and supported by Raymond et al. (1998), convection increases mid-level relative humidity and vorticity *before* the establishment of the tropical cyclone vortex. Furthermore, the modeling study of Nolan (2007) suggests that such changes are *necessary* before any VHT process can establish a sustained, small-sale, low-level vortex. Increasing mid-level moisture allows the ratio of downdrafts to updrafts to lower significantly before genesis, and increasing mid-level vorticity allows deep convective towers to more efficiently heat the atmosphere and create a vortex. Finally, Nolan et al. (2007) similarly found in a modeling study that large-scale thermodynamics determine the rate of tropical cyclone formation.

1.3. General methodology

This section is devoted to describing techniques used to address objectives 1-3, listed in section 1.1. These objectives are addressed in Chapters II and III, which follow the underlying H07 method of investigating probabilistic dynamics in order to explain predictability. Specialized methods are also employed at times in the text to address smaller points, and they will be discussed as they are used.

1.3.1. Uncertainty and/or predictability

The root-mean of difference total energy (RM-DTE) is used to investigate forecast uncertainty. The form of DTE employed here is a commonly used measure of the predictability in ensembles (e.g., Mitchell et al. 2002; Zhang et al. 2006b; Meng and Zhang 2007; H07), and it is calculated as

$$\mathrm{DTE} = 0.5(u'u' + v'v' + kT'T'). \qquad (1)$$

In this equation the prime denotes the difference between a member and the ensemble mean, u and v are the zonal and meridional velocity components, T is the temperature, and $k = C_p / T_r$ (C_p= 1004.9 J kg^{-1} K^{-1} and T_r = 270 K). RM-DTE is calculated via

$$\mathrm{RM-DTE}_{i,j} = \sqrt{\frac{1}{N_e}\sum_{N=1}^{N_e}\frac{1}{k_{\max}}\sum_{k=1}^{k_{\max}}\mathrm{DTE}_{i,j,k,N}}\ , \qquad (2)$$

where i and j are horizontal grid point indices, $k_{\max}$ is maximum vertical extent of the model domain, and N is the ensemble member index. Although this form of DTE does not account for differences in mixing ratio or vertical velocity, the spatial distribution of ensemble spread in these variables is qualitatively similar to that in u, v, and T. Therefore, alternate forms of DTE that account for differences in these variables are qualitatively similar to that shown here.

1.3.2. Correlation analysis

As in H07, the correlation between different forecast variables is investigated to understand the predictability and study relationships between variables within the ensembles. The linear correlation coefficient *r* is calculated among a set of *N* data points using

$$r(x_{ijk},y_{ijk})=\frac{\frac{1}{N-1}\sum_{n=1}^{N}(x_{ijk,n}-\overline{x_{ijk}})(y_{ijk,n}-\overline{y_{ijk}})}{\left[\frac{1}{N-1}\sum_{n=1}^{N}(x_{ijk,n}-\overline{x_{ijk}})^2\right]^{1/2}\left[\frac{1}{N-1}\sum_{n=1}^{N}(y_{ijk,n}-\overline{y_{ijk}})^2\right]^{1/2}}, \qquad (3)$$

where *x* and *y* denote two model-state variables and *i*, *j*, and *k* represent three-dimensional grid points. In order to simplify writing, we will use standard notation for correlation. First, (*A*:*B*) is used to denote correlation between variables *A* and *B*. Because many of the variables investigated in this study are correlated with multiple other variables, statistical control is sometimes used to elucidate the correlation between two variables while effectively holding a third variable constant. For example, if variables *A*, *B*, and *C* are all correlated, then (*A*:*B*) is the correlation between *A* and *B*, and (*A*:*B* | *C*) is the correlation between *A* and *B* when controlling for *C*. The controlled correlation is calculated by removing the variation in *B* that results from its relationship with *C*. In other words, linear regression between *B* and *C* is first used to predict values of *B* given *C*, and the residuals between the actual and predicted values of *B* are then calculated. Finally, *A* is correlated to the residuals to compute the controlled correlation (*A*:*B* | *C*).

Chapters II and III commonly use correlation of variables averaged over spatial areas in order to gain insight into dynamics. For example, in many cases correlation is between area-average sea-level pressure (SLP) at a time when storms in the ensembles are mature and variables at earlier times. Since surface pressure falls are related to net latent heat release (and thus net precipitation) in each conceptual model for tropical cyclone development, much of the correlation analysis here also focuses on the correlation between precipitation totals and various fields (e.g., SLP) that are affected by or affect precipitation and/or latent heating. The area averaging of variables is somewhat different in each chapter and will be discussed in further detail later.

Because the developing cyclones take different tracks, much of the correlation analysis is completed in a Lagrangian framework wherein the subjectively determined meso-α circulation center within every ensemble member is centered upon the same point. At some times in various ensemble members, a closed circulation center does not exist. In that circumstance, the center of the problematic member(s) is (are) defined by the low-level vorticity maximum that is also consistent with the track of the cyclone at previous and later times. Note that the analysis herein is not particularly sensitive to the *exact* definition of the center, so subjective errors have little or no impact on the results.

Finally, the reader should be aware of semantics and convention that affect interpretation. For example, because tropical cyclone intensity is generally negatively correlated with SLP, the correlation analyses here use the negative of SLP instead of SLP so that the correlation will be in a positive sense to the intensity of the storm.

CHAPTER II

PROBABILISTIC DYNAMIC ANALYSIS OF A NON-DEVELOPING GULF LOW*

2.1. Introduction

This chapter uses ensemble forecasts to study the predictability and dynamics of a non-developing low-pressure system near the Florida Keys in July 2004. The lack of predictability associated with the 2004 system (assessed from very strong divergence of numerical simulations of its evolution) provides much of the motivation for this research.

The low was associated with a disturbance that appeared in surface observations as a shear axis beginning on 27 July as it approached the Bahamas (not shown). The shear axis, which was the surface reflection of an mid-tropospheric potential vorticity (PV) anomaly (Fig. 2.1g), continued westward and crossed the Florida peninsula into the Gulf of Mexico on 28 July. The National Center for Environmental Prediction (NCEP) global final (FNL) analysis from 00 UTC 29 July clearly shows the surface (Fig. 2.1a) and 500-hPa (Fig. 2.1g) troughs moving over the west coast of Florida.

The synoptic background was somewhat favorable for tropical cyclogenesis from 29-30 July, and the National Hurricane Center (NHC) mentioned the potential for development in their tropical weather outlooks. The disturbance was encompassed by ample moisture at 700 hPa (Fig. 2.1d-e), and a similar moisture distribution was present

---

* Reprinted with permission from "A probabilistic analysis of the dynamics and predictability of tropical cyclogenesis" by J. A. Sippel and F. Zhang, 2008. *J. Atmos. Sci.*, in press.

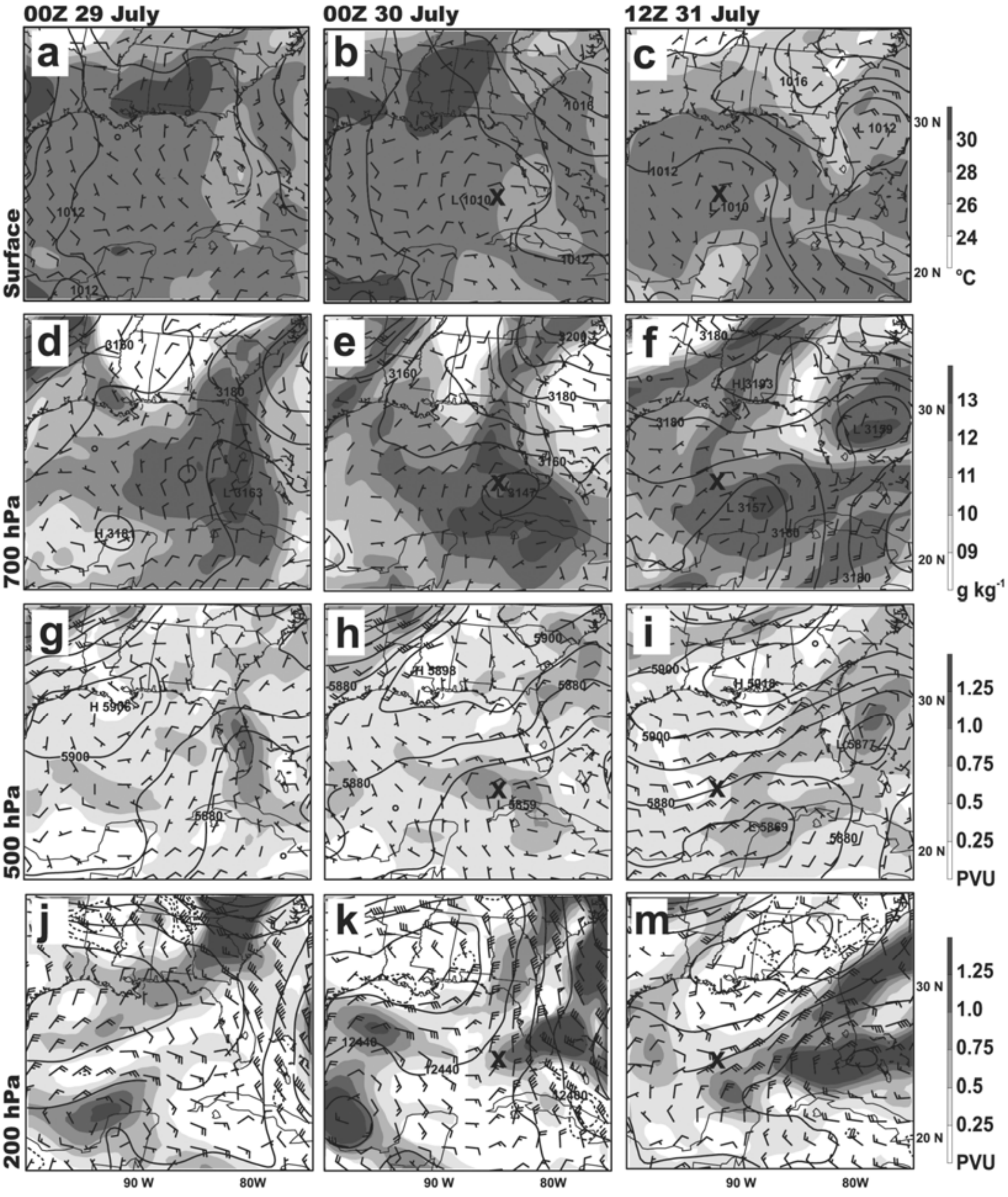

Figure 2.1. FNL analyses from 29-31 July, 2004. The first row shows SLP (contoured every 1 hPa), surface winds (full barb represents 5 $\mathrm{m\,s^{-1}}$), and surface temperature (filled every 2 C). The second row shows 700-hPa heights (contoured every 10 m), cloud water mixing ratio (filled every 1 $\mathrm{g\,kg^{-1}}$), and winds. The third row shows 500-hPa heights (contoured every 10 m), PV (filled every 0.25 PVU), and winds. The fourth row shows 200-hPa heights (contoured every 20 m), PV, and 200-850-hPa wind shear. The bold 'x' in the two rightmost columns represents the location of the surface circulation center.

from the surface through 500 hPa (not shown) over the southern and southeastern Gulf. Rawinsondes from the Florida peninsula and Key West (not shown) taken on 29-30 July reveal that the environment was also unstable and favorable for deep convection. Convective available potential energy (CAPE) was generally between 1500 and 2000 J kg^{-1}, and weak quasi-geostrophic (QG) ascent (~0.5 cm s^{-1})[1] associated with the disturbance helped reduce convective inhibition to less than 10 J kg^{-1} over the southern Florida peninsula and Florida Keys. FNL analyses during the same period show that CAPE over the Gulf of Mexico was generally between 1000 and 2000 J kg^{-1} (not shown). In response to the presence of the disturbance in a favorable thermodynamic environment, widespread convection was evident in infrared satellite imagery (not shown) as the system moved from east of Florida into the Gulf of Mexico. Finally, one neutral to slightly negative factor affecting possible genesis was that 200-850-hPa wind shear values near circulation center were between 12.5 and 15.0 m s^{-1} (Fig. 2.1k-m), which is just above the favorable limit for wind shear according to DeMaria et al. (2001).

Although the 2004 disturbance appeared to be in a marginally favorable environment, it never became a tropical depression. Amidst prolific deep convection, the system intensified somewhat on 29 July when 700-hPa heights fell slightly (compare Fig. 2.1d-e) and a closed low-level circulation developed (compare Fig. 2.1a-b). Despite the closed circulation and continuing convection, the system was never sufficiently organized to attain depression classification, and by 00 UTC 1 August it degenerated into an open

---

[1] QG omega is calculated via 3-D inversion of the Q-vector form of the QG omega equation using the domain-average Coriolis parameter and vertical stability profile. Q-vector forcing, topographic boundary condition forcing, and Ekman forcing are all considered in the inversion. For more details, see the source code of the RIP4 post-processing program (see http://www.mmm.ucar.edu/wrf/users/docs/ripug.htm).

wave (not shown). The failure to develop after 30 July might be related to a possible decrease in mid-level moisture over the center (Fig. 2.1f) and the nearby slightly unfavorable shear values (Fig. 2.1k-m).

2.2. Methodology

This section describes the forecast model, ensemble initialization, and other methods that are only used in the current chapter.

2.2.1. Forecast model

All experiments in this chapter utilize version 3 of the Pennsylvania State University – National Center for Atmospheric Research MM5 mesoscale model (Dudhia 1993) to capture the evolution of the gulf low. With the exception of the addition of a third nested domain, the model setup and physics in this study closely follows that of H07. The control experiment (CTRL) uses an outer domain with 30-km horizontal grid spacing and two two-way nested domains with 10-km and 3.3-km grid spacing. The outer domain has 190×120 grid points, the middle nest uses 241×181 grid points, and the fine nest uses 316×361 grid points. The size and location of the nests (shown in Fig. 2.2a) are such that the 3.3-km nest adequately encompasses the genesis and subsequent tracks of the MM5-generated storms. All domains have 27 terrain-following vertical layers, and the initial and boundary conditions are supplied by the $1° \times 1°$ FNL analysis. The Mellor-Yamada planetary boundary layer (PBL) scheme (Mellor and Yamada 1982) and Reisner microphysics scheme (Reisner et al. 1998) are used, and the model is

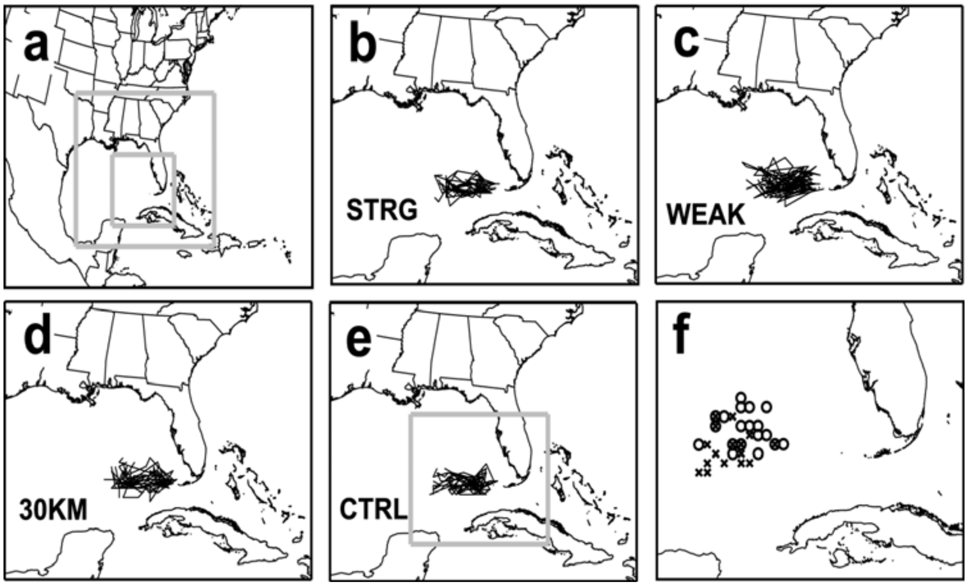

Figure 2.2. The model domain and ensemble forecast tracks of the Gulf low. Panel (a) shows the model domain for all experiments and nests for the high resolution experiment such that the panel exactly encompasses the coarse grid and the fine grids are shown in gray. Panels (b)-(e) exactly encompass the 10-km grid area and respectively show the tracks of circulation centers in STRG, WEAK, 30KM, and CTRL. The gray box in panel (e) represents the 3-km domain. Panel (f) shows 36-h positions in 30KM (demarked with 'o') and CTRL (demarked with 'x') and exactly encompasses the 3.3-km domain.

initialized at 00 UTC 30 July 2004 and integrated for 36 h. While choosing a different start time does not seem to appreciably affect ensemble spread discussed in section 2.3, the results of sections 2.4 and 2.5 might change with model initiation time due to the possibility of flow-dependent dynamics. Investigating this possibility is beyond the scope of the current study. Finally, to be consistent with other experiments, all post-analysis of CTRL is performed on its coarse domain.

Sea surface temperatures are prescribed according to the FNL skin temperature. It is well known that skin temperatures can overestimate the effective mean temperature of the ocean mixed layer, which might explain why many ensemble members forecast more strengthening than observed. Also, tropical cyclones have been observed to decrease sea surface temperatures by 1° to 6°C (Black 1983; Bender et al. 1993) in their wakes. While the wake effect should generally be negligible for very weak storms, it is possible that it would change results for a few of the ensemble members with stronger cyclones discussed in section 2.4.

Another shortcoming of the ensemble initiation method used here is the absence of initial convection in the analysis. This method is typically called a “cold start”, and employing such methodology typically results in a spin up period in which the model quickly forms convection as a reaction to initial convective instability or other factors that favor convection (S. Braun 2008, personal communication). As will be seen, this very likely has some impact upon the results herein.

Sensitivity experiment 30KM utilizes only the outer 30-km domain in order to investigate whether qualitatively similar results to CTRL can be obtained with cumulus parameterization. Integration again starts at 00 UTC 30 July 2004, and the model physics are the same as in CTRL with the exception that the Grell cumulus scheme (Grell et al. 1991; Grell 1993) is used to simulate the storm (since there are no nested domains). As with the other physics options, the Grell scheme was chosen to be consistent with H07. This scheme has been successfully used in simulations of tropical cyclones in the past (e.g., Park and Zou 2004; Braun et al. 2006; Bruan 2006; Wu et al. 2006).

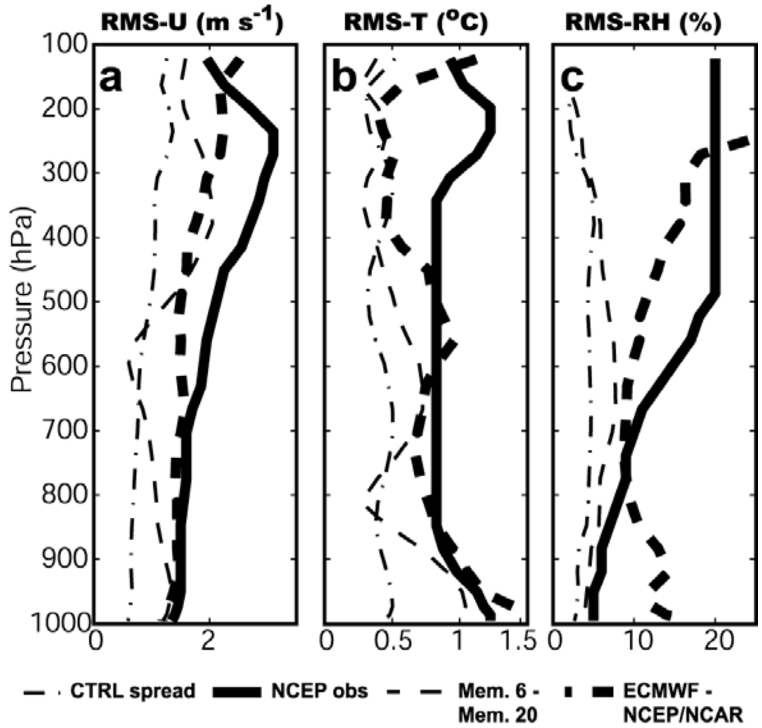

Figure 2.3. The initial RMS spread in comparison with observation error and analysis differences. Initial RMS spread of zonal wind (a), temperature (b), and relative humidity (c) for CTRL over domain 1 is shown in thin dash-dot lines. Shown over the same domain is the RMS difference between the ECMWF operational analysis and the NCEP/NCAR reanalysis (thick dashed lines) and the RMS difference between members 6 and 20 of CTRL (thin dashed lines).

2.2.2. Ensemble initialization

This chapter uses ensembles of 20 members, which is a sufficient number according to the results of Zhang (2005). The ensemble initial conditions of CTRL/30KM were created by perturbing the FNL analysis with random, balanced noise derived from the NCEP background error statistics implanted in the MM5 three-dimensional variational data assimilation system (Barker et al. 2004). Figure 2.3 shows the vertical distribution of the initial ensemble spread in CTRL/30KM, which is 0.7-1.2 $\mathrm{m\,s^{-1}}$ for zonal wind, 0.3-0.6 K for temperature and 2-4% for relative humidity.

The initial spread of CTRL/30KM in Fig. 2.3 appears conservative when compared to other measures of error. For example, the spread is smaller than both NCEP-assumed sounding observational error and the root-mean square (RMS) difference between the NCEP-NCAR $2.5^\circ \times 2.5^\circ$ reanalysis and the ECMWF $2.5^\circ \times 2.5^\circ$ operational analysis over the MM5 domain at the initial time. The RMS difference between the FNL analysis and both the ECMWF analysis and the NCEP-NCAR reanalysis (not shown) is also significantly larger than the spread of CTRL/30KM. Since the RMS difference between various analyses can be used as a rough estimate of typical analysis error at leading operational centers, the spread is also smaller than typical analysis error. In addition, model error is not considered, and boundary conditions are not perturbed here. These additional sources of error imply that this study provides only an upper limit on predictability.

In addition to 30KM, sensitivity experiments WEAK and STRG were created to determine the effect of changing the initial conditions to produce weaker and stronger cyclones. These experiments use the same 30-km domain and model physics as 30KM. In WEAK and STRG, ensembles of initial conditions were generated by respectively perturbing (in the same manner as CTRL/30KM were created) the initial conditions of members 20 and 6 from ensemble CTRL/30KM. Members 6 and 20 are on opposite ends of CTRL/30KM in terms of cyclone strength, and their relative strengths can be judged by the forecasts of surface pressure, wind, and reflectivity shown in Fig. 2.4. The

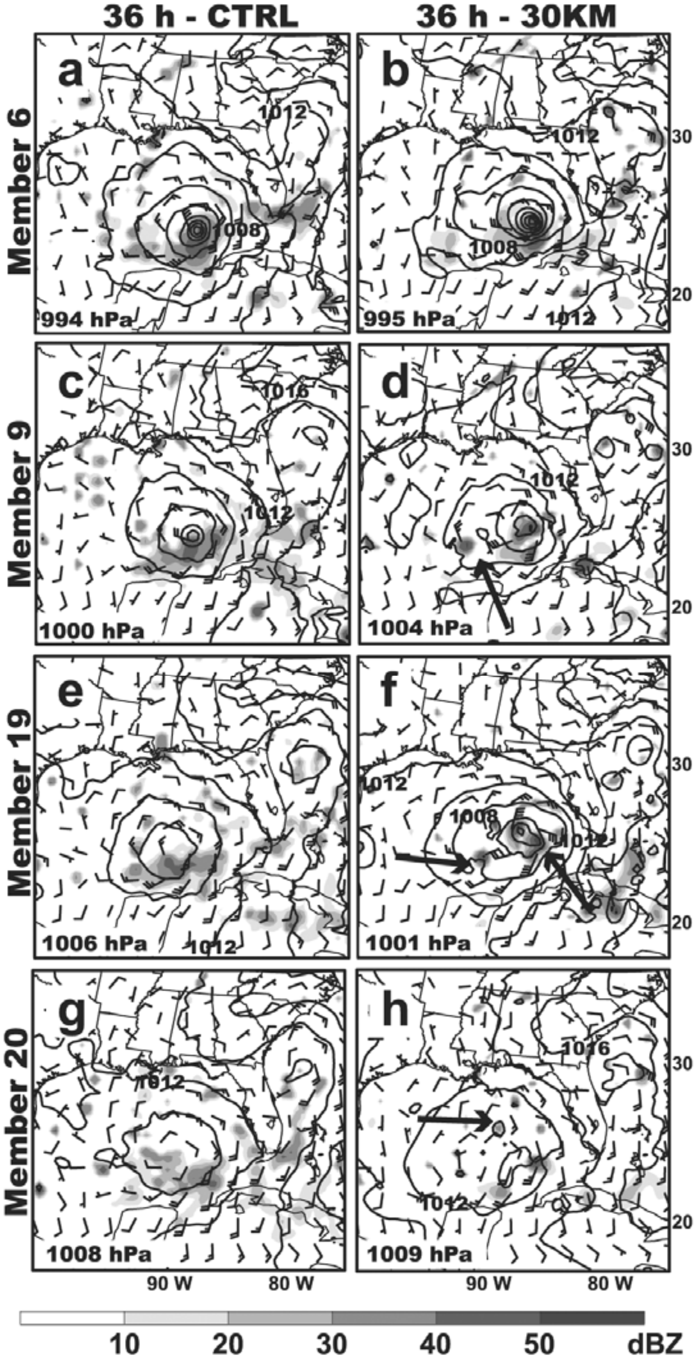

Figure 2.4. Surface forecasts from select members of CTRL and 30KM. Simulated radar reflectivity (shaded every 10 dBZ), sea-level pressure (contoured every 10 hPa) and surface winds (full barb represents 5 $\mathrm{m\,s^{-1}}$) are shown at 36 h. Arrows point to intense convective towers mentioned in text that significantly alter the local environment. The minimum SLP for each member is shown in the bottom-left corner of each panel.

cyclone in member 6 (Fig. 2.4a-b) is generally one of the strongest in the ensemble, while the storm in member 20 (Fig. 2.4g-h) is generally the weakest.

2.2.3. Correlation analysis

Verbal descriptions of linear correlation will follow those of H07 with the exception that correlation above 0.85 is described as very strong. Correlation between 0.7 and 0.85 is described as strong, correlation between 0.5 and 0.7 as moderate, and correlation between 0.3 and 0.5 as weak. Values below 0.3 are described as uncorrelated. In the framework of statistical significance with a sample size of 20, a correlation of 0.7 is statistically different from 0 with over 99% confidence, while 0.5 and 0.3 are respectively different from 0 with roughly 95% and 80% confidence.

Because this particular chapter compares statistics of different ensembles, it is useful to understand which differences in correlation are statistically significant and which are not. Because correlation confidence interval (CI) lengths vary with correlation, and the intervals themselves are not symmetric for smaller sample sizes, Table 2.1 has been included to give CIs for relevant correlation values with a sample size of 20. Generally speaking, differences between strong and weak correlation are associated with fairly high confidence, as are differences between moderate and very strong correlation. However, differences between moderate and strong correlation have lower confidence, and differences between weak and moderate correlation are insignificant. With this the case, care must be taken not to draw conclusions based on small differences, especially for weaker correlation.

TABLE 2.1. Confidence intervals for varying degrees of statistical confidence for correlation (r) values of 0.1, 0.3, 0.5, 0.7 and 0.85 and a sample size of 20.

	r = 0.1	r = 0.3	r = 0.5	r = 0.7	r=0.85
99% CI	(-0.48,0.62)	(-0.30,0.73)	(-0.07,0.83)	(0.24,0.90)	(0.56,0.95)
95% CI	(-0.36,0.52)	(-0.16,0.66)	(0.07,0.77)	(0.37,0.87)	(0.65,0.94)
90% CI	(-0.29,0.46)	(-0.09,0.61)	(0.15,0.74)	(0.44,0.85)	(0.69,0.93)
80% CI	(-0.21,0.39)	(0.00,0.55)	(0.23,0.70)	(0.51,0.74)	(0.74,0.92)

The correlation analysis in this chapter makes frequent use of correlation between area-average SLP at 36 h (hereafter in this chapter, *SLPf*) and variables averaged over spatial areas in order to gain insight into dynamics. Other metrics of storm intensity (i.e., surface vorticity and wind speed) are also occasionally used in correlation analysis at other times. In any case, SLP and other intensity metrics are averaged over an 11×11 grid-point, 300×300 km^2 area surrounding the center. Unless otherwise specified, other variables are horizontally averaged over a 21×21 grid-point, 600×600 km^2 area also centered on the storm center.

2.3. Ensemble performance and predictability

Ensemble spread in CTRL grows rapidly as a result of ensemble members strengthening the incipient cyclone at different rates and moving it in different directions. The left column of Fig. 2.4 shows that by 36 h, there is a wide variety of forecasts within the ensemble. Recall that member 20 forecasts minimal pressure falls up until this time Fig. 2.4g), and member 6 has a strong tropical storm (Fig. 2.4a). The evolution of RM-DTE in CTRL (Fig. 2.5) shows that ensemble spread grows substantially in the vicinity

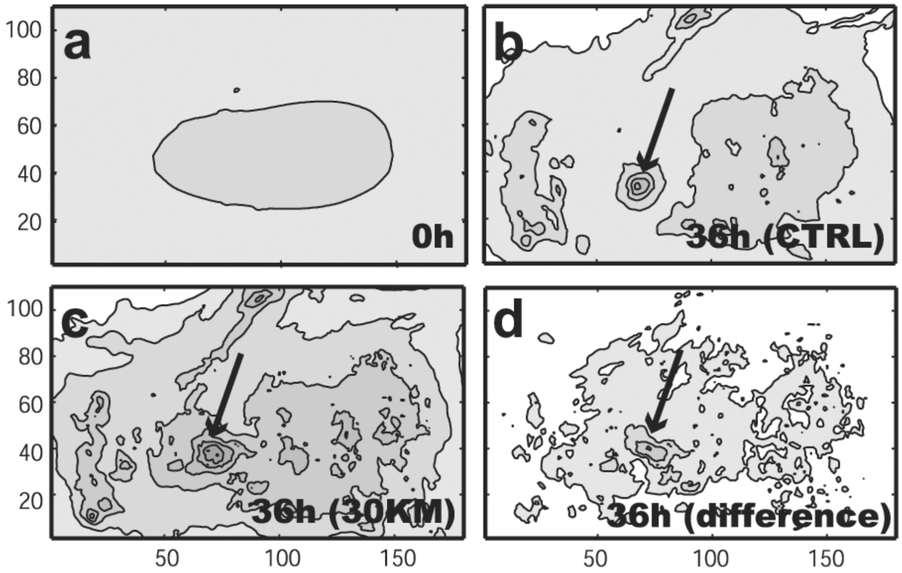

Figure 2.5. RM-DTE of CTRL and 30KM. RM-DTE is calculated according to Eq. 2 and contoured every 1 $\mathrm{m\,s^{-1}}$ starting at 1 $\mathrm{m\,s^{-1}}$ over domain 1. Axis scales are in model grid points. Panel (a) shows the analysis (0-h) RM-DTE for both ensembles. Panels (b) and (c) show 36-h RM-DTE, and panel (d) shows 36-h difference in RM-DTE between the two ensembles. The arrows point to the genesis region.

of the cyclone forecast track (the arrows in Fig. 2.5 point to the genesis region). For example, the absolute maximum horizontal RM-DTE increases from about 2 $\mathrm{m\,s^{-1}}$ at the analysis time (Fig. 2.5a) to over 5 $\mathrm{m\,s^{-1}}$ at 36 h (Fig. 2.5b). Vertical profiles of RM-DTE (not shown) indicate that error growth is similar through the entire lower troposphere and somewhat stronger above 200 hPa.

RM-DTE at 36 h is significantly less in CTRL than in 30KM in the vicinity of the cyclone (Fig. 5), a likely result of how Grell cumulus parameterization treats convection. Low-resolution runs with Grell produce more intense convective cells and less stratiform precipitation than simulations with only explicit convection. For example, Fig. 2.6 shows that far more grid points in CTRL attain the weaker values of reflectivity (i.e., 25-

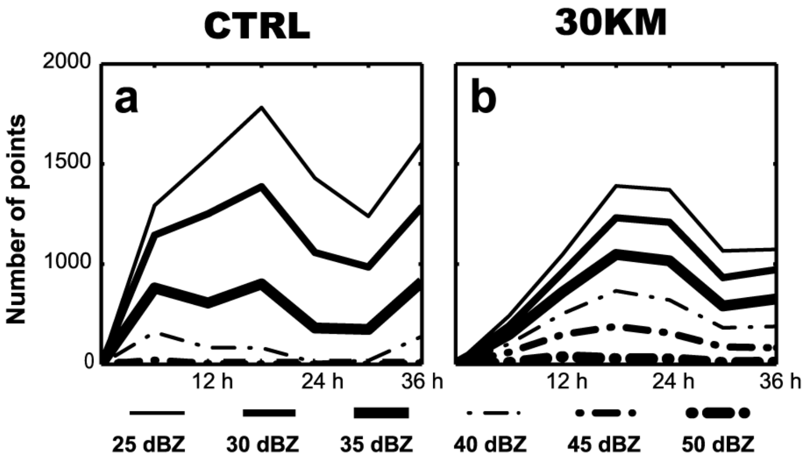

Figure 2.6. The number of grid points summed over all ensemble members that attain threshold values of maximum reflectivity near the cyclone center in CTRL and 30KM. The analysis is completed in a 21×21 grid-point box that is centered on the cyclone center in each member. Maximum reflectivity is calculated by finding the maximum reflectivity value in a vertical column above a given point.

35 dBZ) expected in stratiform precipitation, while more points in 30KM attain the higher values of reflectivity expected in convective cells. One result is that the variance of precipitation totals in the vicinity of the cyclone is much higher in 30KM than CTRL (e.g., Fig. 2.7d). Also, the wind field around deep convective towers in the low-resolution runs is altered over a larger area than that in the high-resolution run (the arrows in Fig. 2.4 point to a few such examples). This is qualitatively similar to findings in Davis and Bosart (2002) and Mapes et al. (2004) that the Grell scheme is often reluctant to activate, but after activation it tends to produce very intense rainfall and excessive perturbations to model variables.

There are slight differences in ensemble-mean cyclone intensity between CTRL and 30KM and much larger differences between WEAK and STRG. The ensemble-

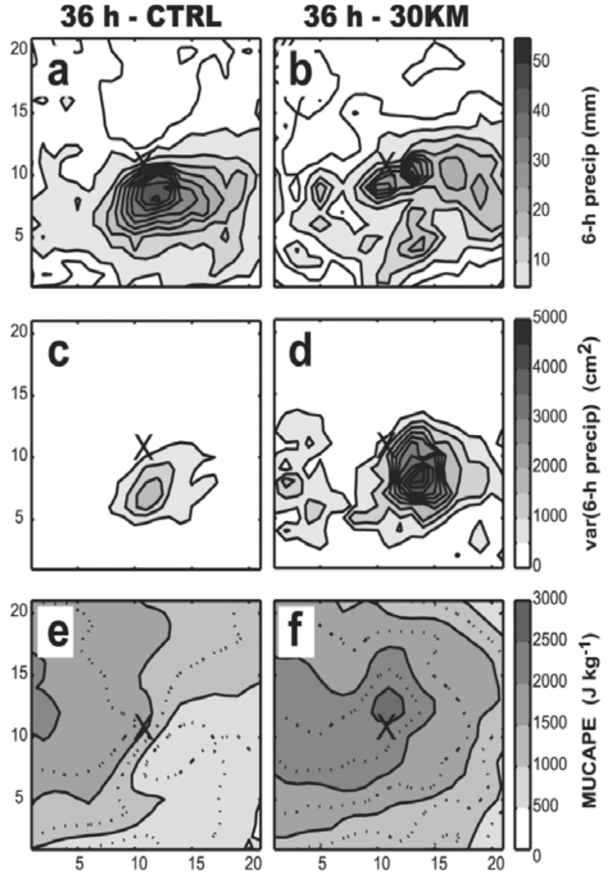

Figure 2.7. Ensemble-mean 6-h precipitation ending at 36 h (a-b), the variance of the same 6-h precipitation (c-d), and ensemble-mean MUCAPE at 36 h (e-f) for CTRL and 30KM. The analysis is completed in a Lagrangian framework, and the 'X' marks the location of the Lagrangian cyclone center. The additional line outside the shaded regions in (a-b) encircles areas where mean precipitation is greater than 2 mm, and the dotted lines in (e-f) indicate intermediate values of MUCAPE in multiples of 250 $\mathrm{J\ kg^{-1}}$.

mean minimum 36-h SLP is 1005.2 hPa in CTRL and 1003.9 hPa in 30KM. Meanwhile, in WEAK and STRG the ensemble-mean SLP is respectively 1008.2 hPa and 998.3 hPa. The discrepancy between WEAK and STRG can also be seen in the relative accuracy of their forecasts. Roughly 25% of the members in WEAK produce quite good forecasts of no cyclogenesis out to 36 h. For example, the 36-h SLP, reflectivity and surface wind forecast of member 14 in WEAK (Fig. 2.8a) shows only a weak, disorganized low in the

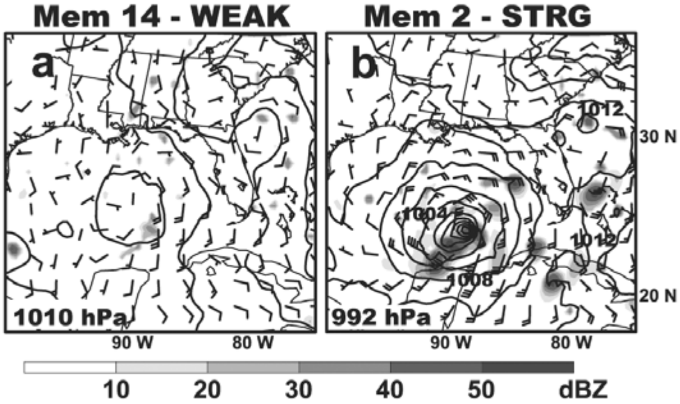

Figure 2.8. As in Fig. 2.4, but for member 14 of WEAK (a) and member 2 of STRG (b) at 36 h.

Gulf of Mexico. The only apparent surface difference between this member and the analysis for the same time (Fig. 2.1c) is that the 1012 hPa isobar is closed in member 14. The impact of the closed isobar on the wind field in member 14 must be minimal since both surface circulations are similar. Meanwhile, no members of STRG produce 36-h forecasts with as weak a surface low as member 20 in CTRL/30KM (i.e., Fig. 2.4g-h) or the several members in WEAK (not shown) that resemble member 14. In fact, four members in STRG have storms of hurricane intensity by 36 h (e.g., Fig. 2.8b).

2.4. Correlation analysis: The basic dynamics in CTRL

Cyclone intensity at 36 h is largely dependent upon the net latent heating and intensity of cyclogenesis during the first 12-24 h. For example, Fig. 2.9b shows the time evolution of correlation between instantaneous SLP (hereafter *SLPi*) and *SLPf*, instantaneous and final surface wind speeds, and instantaneous and final surface vorticity in CTRL. By 12 h, all three variables show strong correlation with their values

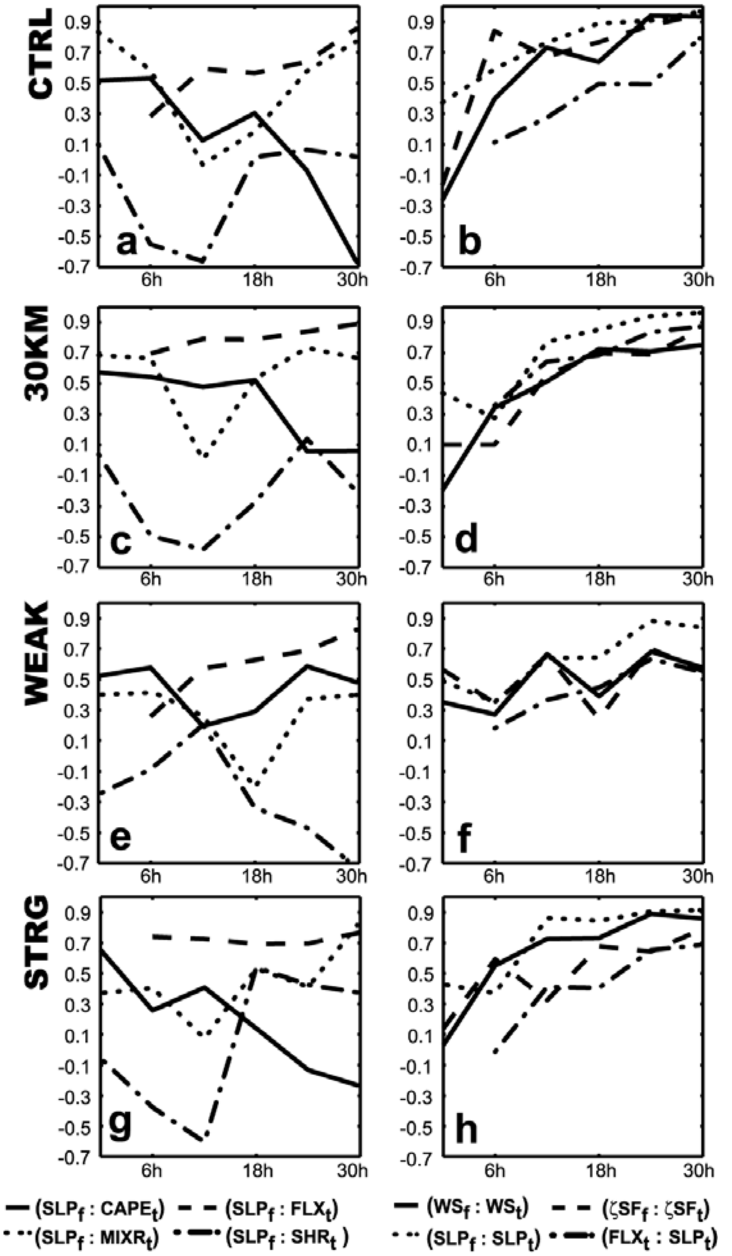

Figure 2.9. The time evolution of correlation between different variables in CTRL (a-b), 30KM (c-d), WEAK (e-f), and STRG (g-h). In the above legends, CAPE refers to MUCAPE, FLX refers to latent heat fluxes, SHR refers to 200-850-hPa wind shear, MIXR refers to 500-850-hPa mean mixing ratio, WS refers to wind speed, ζSF refers to surface vorticity, the ‘f’ subscript represents the final forecast time, and the 't' subscript represents time. CAPE, FLX, and SHR are averaged over a 21×21 grid-point Lagrangian area, and MIXR, SLP, WS, and ζSF are averaged over an 11×11 grid-point Lagrangian area.

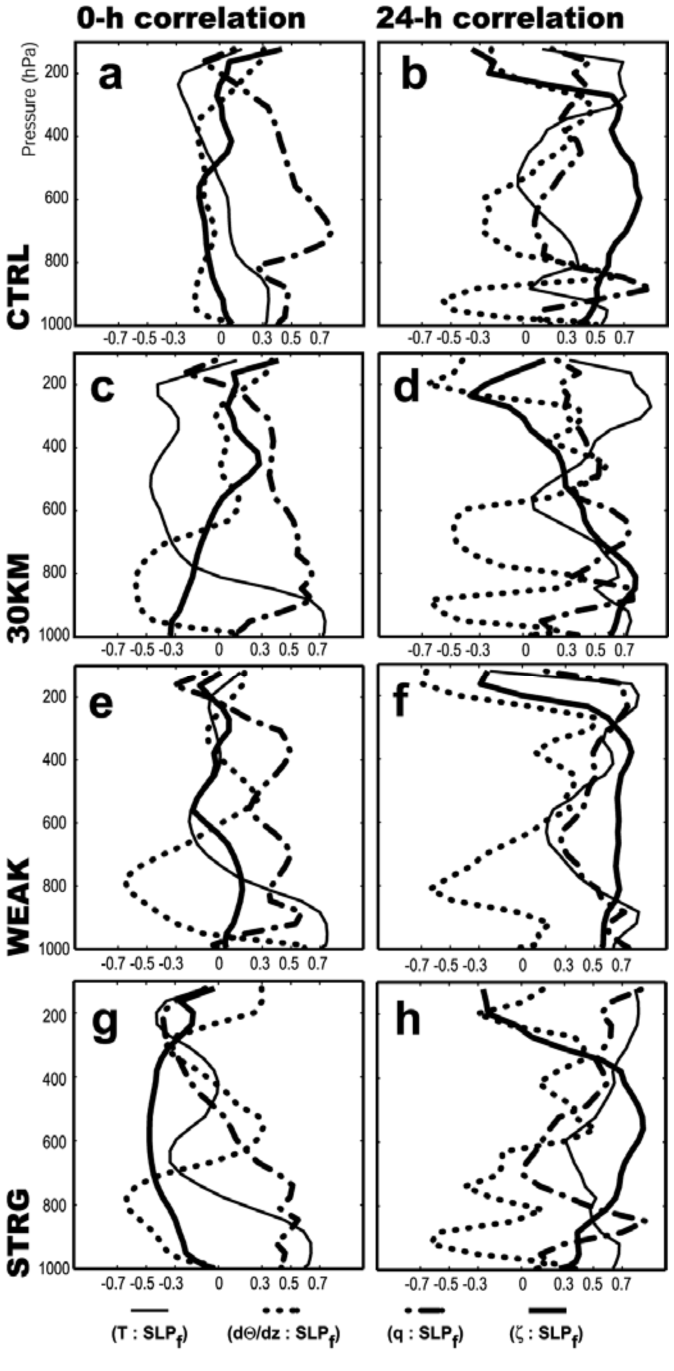

Figure 2.10. The vertical profiles of correlation between final storm intensity ($\mathrm{SLP_f}$) and area-averaged temperature (T), mixing ratio (q), static stability ($\partial\theta / \partial z$), and vorticity ($\zeta$). Time of correlation is indicated at the top of the columns. Variables are averaged over a 21×21 grid-point Lagrangian area, and SLP is averaged over an 11×11 grid-point Lagrangian area. Results are shown for CTRL (a-b), 30KM (c-d), WEAK (e-f), and STRG(g-h).

at 36 h, and by 24 h the correlation is very strong. Similarly, the correlation between *SLPf* and 12-h precipitation totals (not shown) is strong, and it becomes very strong for 24-h precipitation totals. Because differences during the first 24 h crucially determine later differences, the remainder of this study focuses on the first 24 h of cyclogenesis.

2.4.1. Role of deep moisture

The amount of initial moisture present through nearly the entire troposphere is very important for cyclogenesis in CTRL. Figure 2.10a, which shows the correlation between *SLPf* and initial variables in CTRL as a function of height, indicates significant correlation between *SLPf* and water vapor mixing ratio (q) from the surface to about 300 hPa. Furthermore, (q:*SLPf*) around 700 hPa is stronger than correlation between *SLPf* and any other variable in the initial conditions.

Figures 2.11 and 2.12 show how the moisture correlation analysis relates to individual members of CTRL. The bottom row of Fig. 2.11 shows q solid-contoured every 1 g kg^{-1} at 700 hPa for the four ensemble members shown in Fig. 2.4. Figure 2.12h shows the evolution of an 11×11 grid-point average of mean 500-850-hPa q (hereafter *qmid*), and Fig. 2.12f shows the time evolution of area-average wind speeds near the centers of the same four members. Of the four members shown in Fig. 2.11e, member 6 is the only one whose initial 700-hPa q exceeds 10 g kg^{-1} , and it quite clearly has the highest *qmid*. It is also always the strongest member of the four shown in terms of surface wind speeds. Members 9 and 19 have intermediate values of initial *qmid*, and they also have intermediate wind speeds through the forecast. Finally, member 20 is the

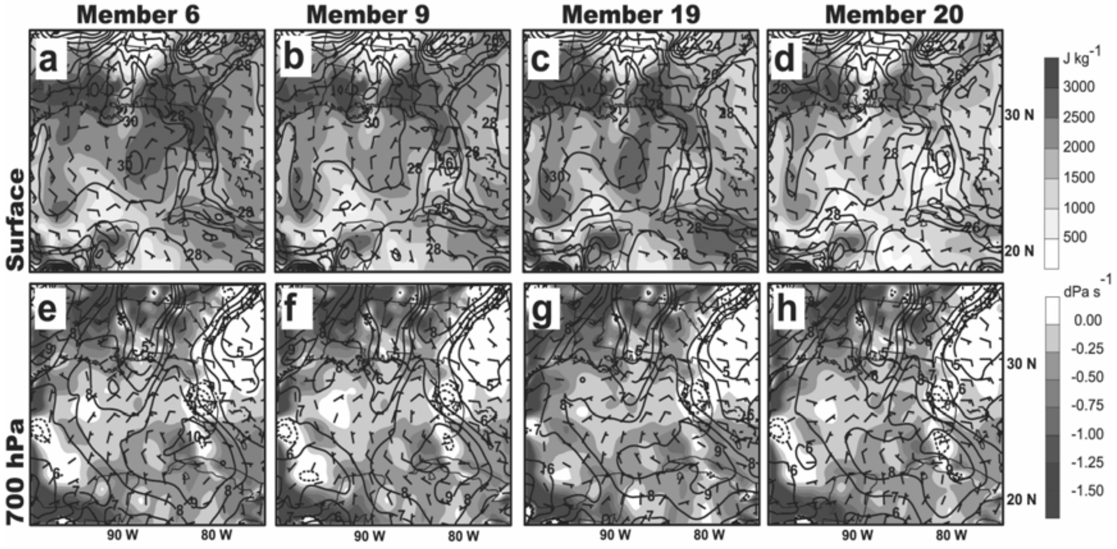

Figure 2.11. The initial fields of ensemble members shown in Fig. 2.4. The top row shows temperature (contoured every 2 C) and MUCAPE (shaded every 500 J kg^{-1}) along with surface wind barbs (full barb represents 5 m s^{-1}). The bottom row shows 700-hPa mixing ratio (solid contoured every 1 g kg^{-1}), QG vertical motion (shaded every 0.25 dPa s^{-1} for QG lift and dash contoured every 0.25 dPa s^{-1} for QG subsidence), and 700-hPa winds.

only member in which the 8 g kg^{-1} isopleth encroaches upon the western edge of the genesis region (Fig 2.12h), and it clearly has the lowest *qmid* of the four members shown. It is also the only member of the four shown that does not strengthen.

Although ensemble members with higher initial mid-level moisture more quickly strengthen the cyclone, it does not appear that higher initial deep moisture directly reduces the strength and/or number of downdrafts. For example, ensemble mean 500-850-hPa q and surface equivalent potential temperature (θ_e) in Fig. 2.13a-b both fall substantially during the first 12 h in CTRL, and Fig. 2.12 shows that ensemble members with *more* initial convection drive this change. First, although surface θ_e is initially

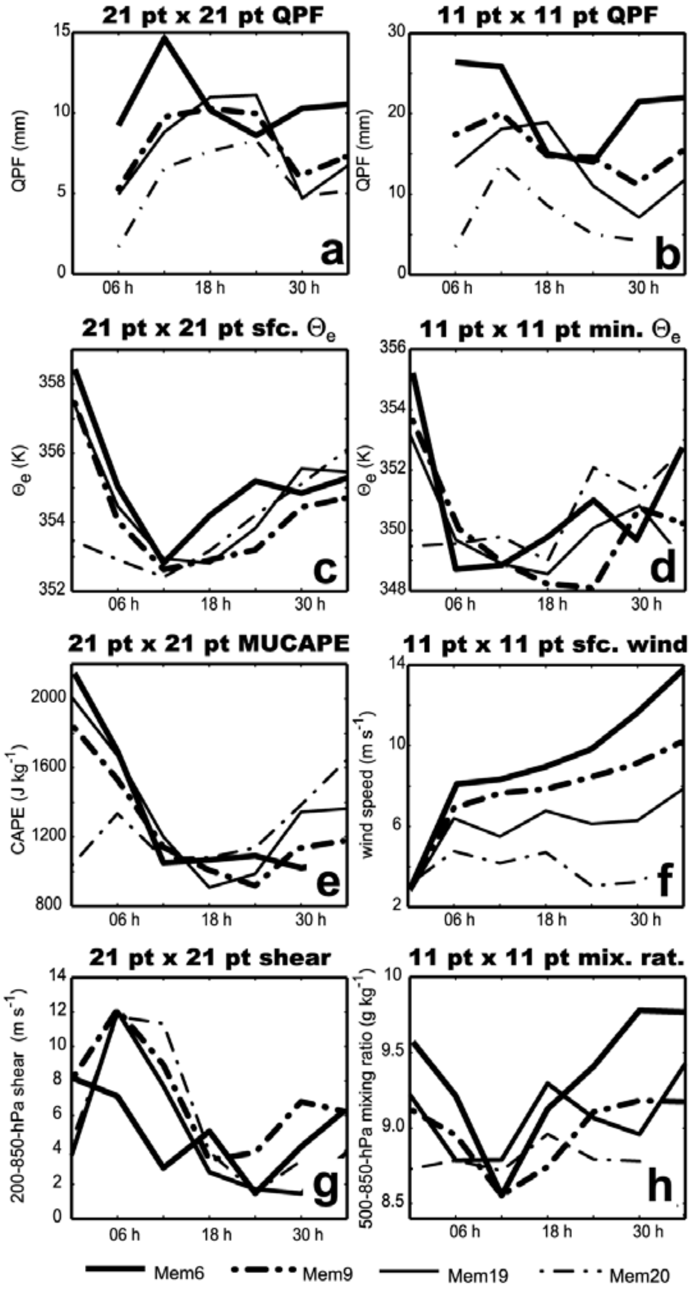

Figure 2.12. The time evolution of certain quantities from the four ensemble members shown in Figs. 2.4 and 2.11. All panels except (d) show the evolution of Lagrangian area-average quantities as indicated in the panel titles. Panel (d) shows the evolution of the minimum surface θ_e in an 11×11 grid-point Lagrangian area.

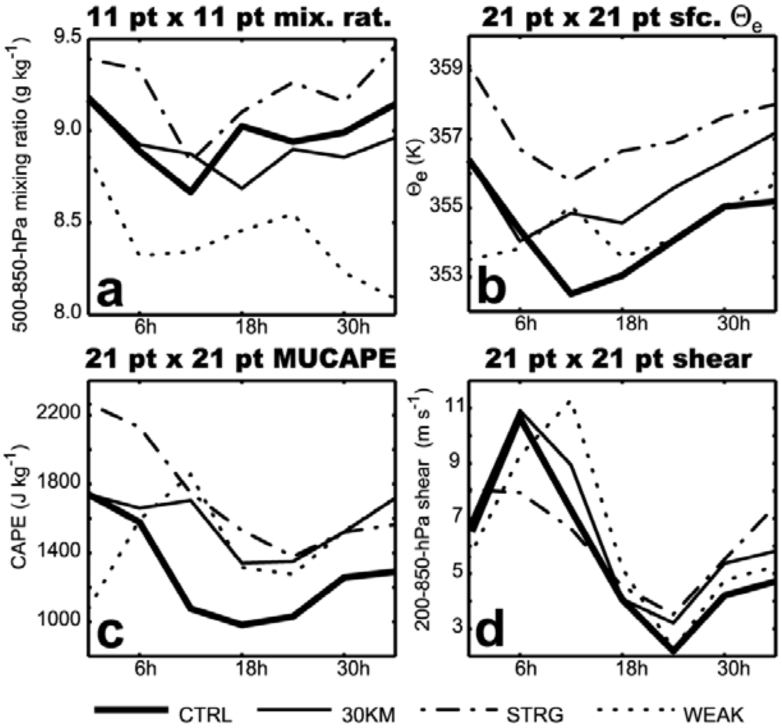

Figure 2.13. The time evolution of certain quantities from Fig. 2.12 for the ensemble means of CTRL, 30KM, STRG, and WEAK.

much higher in the convectively active ensemble members shown in Fig. 2.12, it falls sharply in members with more convection (e.g., Fig. 2.12a-c). By 12 h, θ_e is similar in all members shown. Furthermore, member 6 has the highest initial *qmid*, but it has the lowest minimum surface θ_e near the center by 12 h (Fig. 2.12d). Mid-level moisture also sharply lowers in members 6, 9 and 19 (Fig. 2.12h), and (*qmid*:*SLPf*) becomes insignificant by 12 h (Fig. 9a). Finally, the weak correlation between initial *qmid* and surface θ_e (not shown) during the first 24 h is not statistically different from that at the analysis time. Thus, any relationship between the two variables can be explained by their initial relationship, and higher initial *qmid* does not dynamically alter subsequent θ_e.

It is possible that higher deep moisture directly contributes higher rates of precipitation and latent heating without reducing the number of downdrafts. In fact, some members (e.g., member 6) have so much convection that they actually appear to have *stronger or more numerous* mean downdrafts than ensemble members with less initial moisture and convection. This appears to be consistent with the result from Nolan (2007) that the frequency and strength of updrafts increases as mid-level moisture increases, but the frequency and strength of downdrafts does *not* decrease.

2.4.2. Role of convective instability

Convective instability is also an important factor for cyclone intensity, likely because of its relationship with subsequent precipitation. Area-average most unstable CAPE (MUCAPE[2]) is about 1750 J kg^{-1} in CTRL at the analysis time (Fig. 2.13c), and it is moderately correlated with *SLPf*, 0-12-h precipitation, and 0-24-h precipitation (not shown). Furthermore, (*MUCAPE*:*SLPf*) does not appear to be a simple result of positive correlation between MUCAPE and another variable that favors intensification. In Fig. 2.14, which shows the (*MUCAPE*:*SLPf*) when controlling for initial variables, only initial temperature and mixing ratio below 900 hPa significantly affect the correlation. This is not surprising since PBL temperature and mixing ratio determine over 90% of the variance in MUCAPE. Also, although controlling for PBL mixing ratio and/or temperature reduces (*MUCAPE*:*SLPf*), MUCAPE is still a better predictor of final storm

---

[2] MUCAPE is computed as the CAPE for the parcel in each column with maximum equivalent potential temperature within the lowest 3000 m. Following the recommendation of Doswell and Rasmussen (1994), virtual potential temperature is used in this calculation.

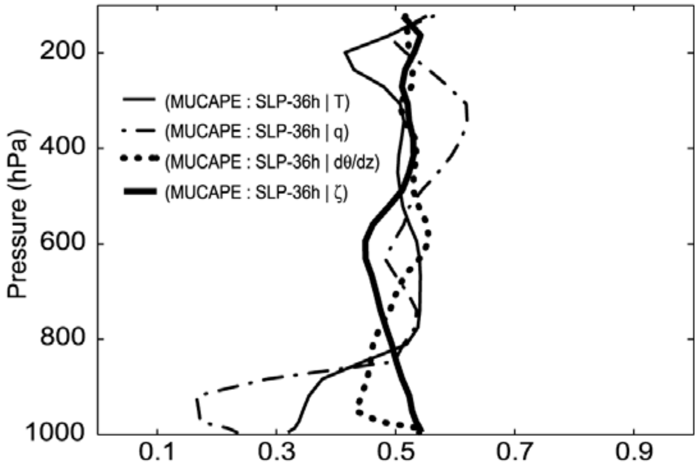

Figure 2.14. Correlation between MUCAPE and final intensity (SLP-36h) when controlling for temperature (T), mixing ratio (q), static stability ($\partial\theta/\partial z$), and vorticity (ζ) at different heights at the analysis time. All variables except SLP-36h are averaged over a 21×21 grid-point Lagrangian area. SLP-36h is averaged over an 11×11 grid-point Lagrangian area.

intensity than either of these variables individually.

Though it is not readily apparent in Fig. 2.11, MUCAPE in this case relates to the large-scale environment through its association with QG lift. The MM5 develops the cyclone in an environment of weak QG lift (shaded in the bottom row of Fig. 2.11), which is known to reduce static stability and moisten the atmosphere. MUCAPE over the genesis region is well correlated low-level QG lift in the genesis region of CTRL. However, low-level QG lift and *SLPf* are not significantly correlated, so QG lift is not directly a significant contributor to storm intensity.

MUCAPE in CTRL quickly becomes uncorrelated with *SLPf* as convection in the ensemble significantly reduces its magnitude (e.g., Fig. 2.13c) and variance. (*MUCAPE*:*SLPf*) significantly decreases after 6 h in Fig. 2.9a, and MUCAPE becomes similar for all ensemble members shown in Fig. 2.12e by about 12 h. By 30 h the members of CTRL that have high MUCAPE are those that have little convection, and the correlation between 30-h MUCAPE and precipitation over the preceding 6 h in CTRL is strongly negative (not shown). Thus, (*MUCAPE*:*SLPf*) becomes significantly anticorrelated in Fig. 2.9a.

Figures 2.11 and 2.12 show how the above correlation analysis relates to individual ensemble members in CTRL. The top row in Fig. 2.11 displays MUCAPE, again shaded every 500 J kg^{-1}, and surface temperature contoured every 2 C. In member 6 (Fig. 2.11a) the maximum MUCAPE slightly to the west of the genesis region is higher than in the other members. This member also has the least pronounced minimum in MUCAPE in the immediate genesis region. Meanwhile, member 20 (Fig. 2.11d) starts off with significantly lower initial MUCAPE and surface temperatures than the other members shown in Fig. 2.11. Figure 2.12 shows that the convective response during the first 12 h of integration is in general proportion to the initial area-average convective instability. Likewise, there is a dramatic increase in area-averaged surface wind speeds near the centers of the stronger ensemble members during the first 6 h. Thereafter, stronger ensemble members stay stronger, and weaker members stay weaker.

2.4.3. Role of vorticity and vertical wind shear

Ensemble-mean deep-layer (200-850-hPa) wind shear peaks around 6 h in CTRL (Fig. 2.13d), and shear from 6-12 h is moderately anticorrelated with *SLPf* (Fig. 2.9a). Note that the shear in Figs. 2.12 and 2.13 is again an area average, and ensemble-mean

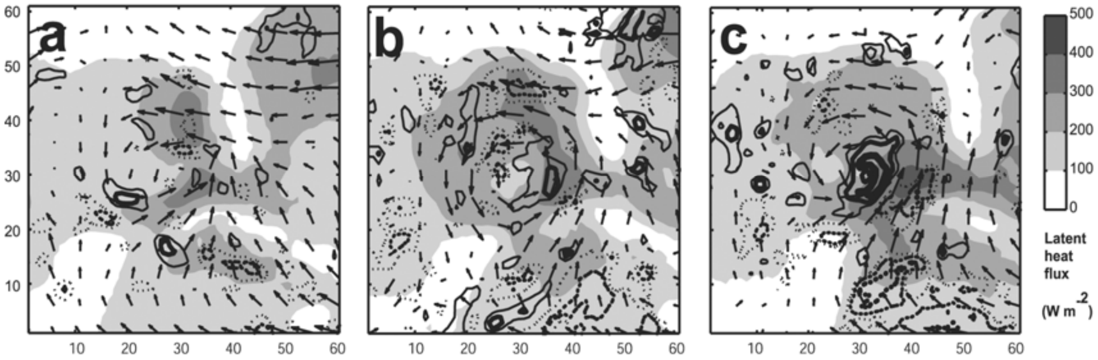

Figure 2.15. Ensemble-mean latent heat flux (shaded every 100 W m^{-2}), surface wind vectors (scaled differently in each panel), and instantaneous correlation between total heat fluxes and intensity for CTRL at 12 (a), 24 (b), and 36 h (c). Correlation is contoured at -0.7, -0.5, -0.3, 0.3, 0.5, and 0.7 with solid lines indicating positive correlation, dashed lines indicating negative correlation, and increasing thickness indicating increasing correlation magnitude. All panels are in a Lagrangian framework.

shear during the first 12 h is generally in agreement with Fig. 2.1k. The substantially weaker shear at later times in Figs. 2.12 and 2.13 seems to have little effect on final intensity (Fig. 2.9a).

The dramatic decrease in shear at later times in Figs. 2.12g and 2.13d appears to be caused by convection that occurs during the first 12 h. For example, 12-h precipitation totals are strongly anticorrelated with deep-layer shear at 12 h in CTRL. Even the convection in member 20, which is weaker than that of any other ensemble member (Fig. 2.12a-b), is sufficient to rearrange the upper level PV field (not shown) and reduce deep layer shear in the genesis region by 18 h (Fig. 2.12g). The resultant upper level PV and shear fields are incongruent with the analyses in Fig. 2.1k-m and show how quickly well-placed convection can lead to error.

Low-level vorticity is initially uncorrelated to *SLPf* in CTRL, but it quickly becomes an excellent predictor of itself. Considering that most ensemble members demonstrated development, the initially insignificant correlation in Fig. 2.10a may indicate that the initial disturbance provides sufficient vorticity for cyclogenesis to proceed in all members. Meanwhile, 6-h surface vorticity is very strongly correlated with final vorticity in CTRL. Thus, ensemble members that are able to rapidly build a surface vortex during the first 6 h are the same members that have stronger vorticity at 36 h.

2.4.4. Initial latent heat fluxes and the onset of WISHE

It is clear from Fig. 2.9 that surface latent heat flux[3] (hereafter LHF) is important before WISHE becomes a dominant intensification factor in CTRL. (*LHF*:*SLPf*) rises to moderate strength by 12 h (Fig. 2.9a), and LHF over the first 12 h is weakly to moderately correlated to subsequent precipitation. Yet, (*LHF*:*SLPi*) is quite weak during the first 24 h (Fig. 2.9b). The statistical significance of LHF before 24 h is therefore notstrongly tied to WISHE (see Emanuel 1986, 1989, 1995; Rotunno and Emanuel 1987), which should cause high instantaneous correlation between LHF and SLP.

WISHE appears to become a more important intensification mechanism by 30 h in CTRL. In Fig. 2.15, ensemble-mean LHF is shaded, and (LHF:*SLPi*) is contoured. The expanding area of dark shading and increasingly bold contours near the center from 12-36 h shows that LHF and *SLPf* become intimately related as LHF increases. Likewise,

---

[3] While WISHE theory relates to *total* heat flux (i.e., the sum of latent and sensible heat flux), latent heat fluxes in these simulations are more than an order of magnitude greater than sensible fluxes. Therefore, the correlation between storm intensity and total fluxes is determined almost exclusively by latent heat fluxes.

Fig. 2.9a shows that (*LHF*:*SLPi*) increases to a strong level by 30 h, which is consistent with WISHE becoming an intensification factor.

Another indication of the growing importance of WISHE in CTRL is the evolution to dynamics of a more mature tropical cyclone. Specifically, the correlation profiles in Fig. 2.10b become generally consistent with the expectation that a tropical cyclone will have a warm, moist, high-vorticity core in the troposphere and an anticyclone near the tropopause (e.g., Gray 1975; Hawkins and Imbembo 1976; Frank 1977). A notable exception is the large drop in correlation in (*q*:*SLPf*) at mid levels. This particular correlation drops because the averaging area for *q* in Fig. 2.10b encompasses the tropical cyclone core and areas of subsidence outside the core. Stronger cyclones should have higher moisture in their cores, but they also will be surrounded by more intense subsidence. Thus, by 24 h the smaller averaging area used in the *qmid* correlation is a more appropriate predictor of *SLPf*. Indeed, *qmid* and *SLPf* in Fig. 2.9a are moderately correlated. This represents a significant change in dynamics from 12 h, when the two variables are uncorrelated due to downdrafts.

2.5. Sensitivity experiments

This section first analyzes some possible impacts of cumulus parameterization. Ensemble 30KM is created using the same initial conditions as in CTRL, but only the 30-km domain is used. More importantly, this requires the use of cumulus parameterization. While using cumulus parameterization is not preferable since the merits of individual cumulus schemes are presently limited (e.g., Arakawa 2004), it is often necessary in the operational environment where models are used with grid spacing larger than that in CTRL.

Also investigated here are the effects of changing the ensemble initial conditions in 30KM to those that produce generally weaker (WEAK) and stronger (STRG) storms. The purpose of these experiments is to investigate the extent to which genesis dynamics change when both more and fewer ensemble members encompass the truth.

2.5.1. Experiment 30KM: Possible effects of cumulus parameterization

As in CTRL, cyclone intensity in 30KM strongly depends upon the strength of cyclogenesis and amount of precipitation during the first 24 h. In Fig. 2.9d (*SLPi*:*SLPf*) becomes very strong by 24 h, and surface wind speed and vorticity also have strong time-lag relationships by 18 h. Precipitation totals over the first 24 h are also strongly correlated with *SLPf*, which shows that latent heating during the first 24 h is crucial to cyclogenesis in 30KM.

The vertical correlation profiles in Fig. 2.10 show that the amount of deep moisture present is also crucial in 30KM. As in CTRL, *SLPf* is weakly to moderately correlated with the initial *q* through nearly the entire troposphere. While the level of maximum correlation is about 100 hPa lower than in CTRL, and the magnitude of (*q*:*SLPf*) is somewhat lower in 30KM through the middle troposphere, these differences are not statistically significant with even 80% confidence.

Convective instability is also important in 30KM, again largely because of its relationship with subsequent precipitation totals. As with CTRL, MUCAPE at the analysis time is moderately correlated with both *SLPf* and subsequent 24-h precipitation totals. This again provides a direct link between initial MUCAPE and *SLPf*. Also, weak correlation (0.38) between QG lift and MUCAPE suggests that the QG circulation indirectly contributes to cyclogenesis in 30KM as well.

One important difference between CTRL and 30KM is that (*MUCAPE*:*SLPf*) in 30KM is positive for a much longer time. Comparing Fig. 2.9a with Fig. 2.9c, (*MUCAPE*:*SLPf*) in 30KM at 12 h (18 h) is different from that in CTRL with 90% (80%) confidence. The difference is even stronger by 30 h, when the two variables are moderately anticorrelated in CTRL and uncorrelated in 30KM. This difference in correlation is significant with more than 99% confidence.

A possible interpretation of this result is that the Grell cumulus parameterization scheme is overly sensitive to CAPE because it relies too heavily on low-level instability to determine where convection should occur. This is supported by the difference in how *SLPf* relates to thermodynamic variables in 30KM and CTRL. In 30KM, *SLPf* is strongly correlated to the initial temperature within the PBL and moderately to strongly anticorrelated with static stability from within the PBL to between 700 and 800 hPa (Fig. 10c). The correlation in both these relationships is different from its corresponding value in CTRL with 95% confidence. It appears that the strong anticorrelation between static stability and *SLPf* in 30KM is due to the fact that the Grell scheme is generally quite sensitive to the vertical gradient of moist static energy near the top of the PBL (e.g., Cohen 2002).

The difference in how convection is treated in 30KM and CTRL is another possible reason for the discrepancy in (*MUCAPE*:*SLPf*). Because 30KM tends to produce less widespread stratiform precipitation than CTRL (e.g., Figs. 2.4 and 2.6), it is less effective at reducing MUCAPE over a large area. For example, ensemble-mean MUCAPE and surface θ_e (Fig. 2.13b-c) fall much less in 30KM than CTRL over the first 12 h. Furthermore, Fig. 2.7 shows a specific example of how MUCAPE relates to precipitation in CTRL and 30KM at 36 h. The 36-h ensemble-mean precipitation maximum is generally south and east of the mean center in both CTRL and 30KM, but MUCAPE in this area in 30KM is much higher than that in CTRL. Thus, the nature of convection in 30KM appears to less effectively destroy CAPE. Also, as previously mentioned, the correlation between MUCAPE and preceding precipitation in CTRL becomes strongly negative by 30 h, whereas the two variables have no statistically significant relationship at 30 h in 30KM. This difference is significant with more than 99% confidence.

The use of cumulus parameterization might also affect the correlation between initial vorticity and *SLPf* in 30KM in an unphysical way. Figure 2.10c shows that initial surface vorticity and *SLPf* are weakly anticorrelated in 30KM, which is a counterintuitive result. Recall that low-level vorticity is uncorrelated to *SLPf* in CTRL; the difference in correlation here is significant with about 90% confidence.

Also, the time-lag correlation between instantaneous and final vorticity in 30KM is generally less than it is in CTRL. The difference is most extreme at 6 h (compare Fig. 2.9b and 2.10d), when the correlation is only around 0.1 in 30KM, but it is over 0.8 in

CTRL. This is a significant difference with over 99% confidence and indicates that it takes longer for a coherent vorticity maximum to organize in 30KM than in CTRL.

Deep-layer wind shear remains an important inhibitor to strengthening in 30KM. The evolution of shear is very similar to that in CTRL (Fig. 2.13d), and as before *SLPf* is most strongly anticorrelated to shear when shear is highest. Also as in CTRL, the magnitude of shear decreases tremendously between 6 and 18 h. Since 12-h shear in 30KM is strongly anticorrelated with 12-h precipitation totals, the decrease in shear again seems to be the result of deep convection.

Finally, LHF is important in 30KM, but there is some difference from CTRL in its relationship with *SLPf*. First, (*LHF*:*SLPf*) indicates that LHF again contributes to strengthening before the onset of WISHE (Fig. 2.9c). As in CTRL, (*LHF*:*SLPi*) increases with time, and it appears that WISHE is a dominant factor by about 24-30 h. The major difference between CTRL and 30KM is that (*LHF*:*SLPf*) is significantly less in CTRL around 6 h; the reason for this large difference is unclear. Differences between CTRL and 30KM in terms of both (*LHF*:*SLPi*) and (*LHF*:*SLPf*) continue until about 30 h, but they are not statistically significant.

2.5.2. Experiments WEAK and STRG: The effect of changing initial conditions

The underlying dynamics in WEAK and STRG have both similarities to and differences with those of 30KM. First, despite the large difference in mean layer moisture from STRG to WEAK (Fig. 2.13a), initial deep moisture is significantly correlated with *SLPf* in both ensembles (Fig. 2.10). While shear is also an inhibiting factor in both ensembles at different times in Fig. 2.10, the evolution of correlation between shear and *SLPf* is different than 30KM in both ensembles. The shear to *SLPf* correlation in STRG initially resembles that of 30KM, but it becomes significantly positive after 12 h. Meanwhile, shear and *SLPf* are initially uncorrelated and become more strongly anticorrelated after 12 h in WEAK. These differences in correlation from 30KM are significant with at least 90% confidence by 30 h, and because shear in Fig. 2.13 is generally similar among the ensembles at later times, they indicate that the effect of shear likely depends on storm intensity. As with shear, the importance of MUCAPE changes with time differently in STRG and WEAK than in 30KM. In WEAK (Fig. 2.9e), (*MUCAPE*:*SLPf*) has no net trend, but (*MUCAPE*:*SLPf*) becomes lower in STRG (Fig. 2.9g) than in 30KM. The difference in correlation between WEAK (STRG) and 30KM is significant with 90% (80%) confidence by 30 h, and it appears that the time it takes to transition from the CAPE intensification regime also depends on storm intensity. Finally, Fig. 2.9 shows that the relationship between LHF and *SLPf* is generally similar in WEAK and STRG to that seen in 30KM. (*LHF*:*SLPi*) rises from insignificant levels at 6 h to moderate and high levels at 30 h. Although (*LHF*:*SLPf*) is weaker in WEAK than STRG with over 95% confidence (compare Fig. 2.9e with Fig. 2.9g), the difference quickly decreases with time. Again, the reason for the large difference at early times is unclear.

2.6. Discussion

The primary intensification mechanism during the first 6-12 h in CTRL is the explosive development of convective towers in a moist, unstable environment of weak QG lift. The presence of a stronger QG circulation with more lift over the genesis region leads to stronger destabilization. Figure 2.12 shows that those ensemble members that have the most initial MUCAPE and deep moisture averaged over a large region around their cyclone centers tend to produce more precipitation both in the immediate vicinity of the centers and over the larger area during the first 6-12 h. The immediate response to the deep convection is a rapid increase in surface wind speeds in the immediate vicinity of the centers, and after 6 h the surface wind speeds in the strongest member are roughly twice those in the weakest member (Fig. 2.12f).

The intensification rate subsides dramatically for all members by 12 h, likely because prolific downdrafts stabilize the lower troposphere (Fig. 2.12c-e). For example, area-average surface θ_e reaches a minimum around 12 h. In response to the stabilization precipitation rates plateau or fall significantly, depending on the ensemble member and averaging area.

Precipitation rates increase again when surface θ_e recovers after 24-30 h near the centers of convectively active members. This is approximately the time that the ensemble statistics support the WISHE mechanism becoming an intensification factor. Concomitant with the increase in precipitation and onset of WISHE, the rate of intensification begins to accelerate, a tendency most strongly seen in member 6.

Downdrafts still affect the minimum θ_e when precipitation intensifies from 24-36 h (compare Figs. 2.10b and 2.10d), but not to the extent of the earlier downdrafts.

Since MUCAPE and deep moisture are responsible for vortex spinup before 12 h, they ultimately help determine the intensity of the final cyclone. For example, the correlation analysis in Fig. 2.9 shows that SLP variations at 12 h account for nearly 65% of the variance in intensity at 36 h. While it is well known that convective instability does not contribute to the strength of very intense tropical cyclones (e.g., Persing and Montgomery 2005), convective instability here infuses energy into the system *before* WISHE becomes dominant. After 12 h it appears that pre-WISHE surface heat fluxes and eventually WISHE itself amplify the 12-h differences, resulting in large ensemble spread.

A simple thought experiment shows how an environment of higher CAPE could be expected to support more rapid initial genesis of a tropical cyclone. In areas where no other factors (e.g., CIN) restrain convection, a greater amount of CAPE will result in more prolific overturning of the atmosphere before a moist-neutral state is reached. One manifestation of this fact is that, regardless of complications associated with parcel theory, it is still true that updraft velocity in a given environment increases with increased CAPE (e.g., Michaud 1996; Crook 1996). This is dynamically important to tropical cyclone formation because greater updraft velocities will generally be associated with stronger stretching and production of vertical vorticity. Thermodynamically, in an environment of higher CAPE there should also be a greater difference between the mean temperature in updrafts and the environmental temperature. Therefore, sustained convection in a high-CAPE environment should produce a stronger tropospheric warm temperature anomaly in the vicinity of the convection than would occur in a low-CAPE environment. The balanced response to such an anomaly would be a decrease in surface pressure beneath it, concomitant with the increase in vorticity.

The importance of initial deep moisture here agrees with numerous other tropical cyclone modeling and observational studies, but how the importance of CAPE relates to other findings is unclear. On one hand, Montgomery et al. (2006) noted that VHTs appear to "compete" with one another for ambient CAPE. It is possible that higher CAPE in this particular case generally favors stronger and/or more numerous VHTs, which in turn incrementally contribute to system-scale heating and vortex spinup. On the other hand, the idealized results of Nolan et al. (2007) suggest *no* relationship between environmental CAPE and the rate of cyclone development. There are several major differences between Nolan (2007) and the current study, including their use of radiative-convective equilibrium and no vertical wind shear in their initial conditions. Thus, it is quite possible that these differences strongly govern how cyclones in the current study and theirs respond to initial CAPE differences.

Although using cumulus parameterization and changing the initial ensemble mean produces qualitatively similar results in the 2004 case, such changes can significantly modulate how quickly an ensemble moves out of the CAPE-based intensification regime and when shear becomes an important factor. The Grell cumulus scheme is strongly sensitive to lower tropospheric temperature and static stability, and it affects the nature of convection, resulting in less stratiform precipitation and more deep convective cells.

This convection with Grell does not remove MUCAPE over a large region as effectively as high-resolution, explicit convection, and MUCAPE therefore contributes to intensification in a low-resolution ensemble with cumulus parameterization (30KM) for a longer period of time than it does in a high-resolution ensemble with only explicit convection (CTRL). Meanwhile, in another low-resolution ensemble with the initial conditions modified to produce stronger storms (STRG), MUCAPE stays correlated with final intensity for less time than in 30KM. Exactly the opposite behavior is noted in a third low-resolution ensemble with weaker storms (WEAK). Finally, shear negatively affects storm intensity in WEAK at a much later time than in the other ensembles.

Also, it appears that cumulus parameterization can appreciably change the ensemble spread. In this situation, there is a fair amount more spread in 30KM than in CTRL in terms of RM-DTE over the entire domain. The discrepancy is accentuated in the region of the ensemble mean position of the cyclone at 36 h, where the peak in RM-DTE in 30KM is nearly double that in CTRL. This difference in spread is likely intimately related to difference in the nature of convection between CTRL and 30KM.

Finally, the use of the cold start initialization technique likely impacts results here, but the extent to which this is the case is not known. The sudden onset of deep convection early in the ensemble is well within any potential model spin up period, and the strongest reaction to the cold start technique is most likely to be felt in the ensemble members that most strongly favor initial convection. Thus, it is probable that this particular technique is an artificial source of strengthening in some ensemble members and therefore also a source of ensemble spread. To test the repeatability of the results in this chapter, the next chapter will investigate an entirely different cyclogenesis event with an entirely different initialization technique.

CHAPTER III

PROBABILISTIC DYNAMIC ANALYSIS OF HURRICANE HUMBERTO (2007)

3.1. Introduction

This chapter is intended as a follow-up study to Chapter II and will use an ensemble forecast to investigate Hurricane Humberto, which rapidly formed off the upper Texas coast on the morning of 12 September, 2007 (see Fig. 3.1). The system was operationally declared a tropical depression at 1500 UTC, though the best-track analysis issued by the NHC estimates that the depression had formed by 0900 UTC and that the system was a 35-kt tropical storm by 1200 UTC (Fig. 3.2). By the time of its landfall east of High Island, TX at 0700 UTC 13 September, the storm had strengthened to an 80-kt, Category 1 hurricane. Thus, the cyclone intensified by approximately 45 kt in the 19 hours before its landfall, which makes it the most rapidly intensifying, near-landfall storm in US records.

3.1.1. Genesis environment

The initial local environment preceding the development of Hurricane Humberto was relatively favorable for genesis, although unfavorable factors lingered on a larger scale. The focus for convection prior to cyclogenesis was an inverted trough at low- to mid-levels that manifested itself at the surface as a weak low (Fig. 3.3). This system had moved westward across the Gulf of Mexico during the preceding week, and the NHC

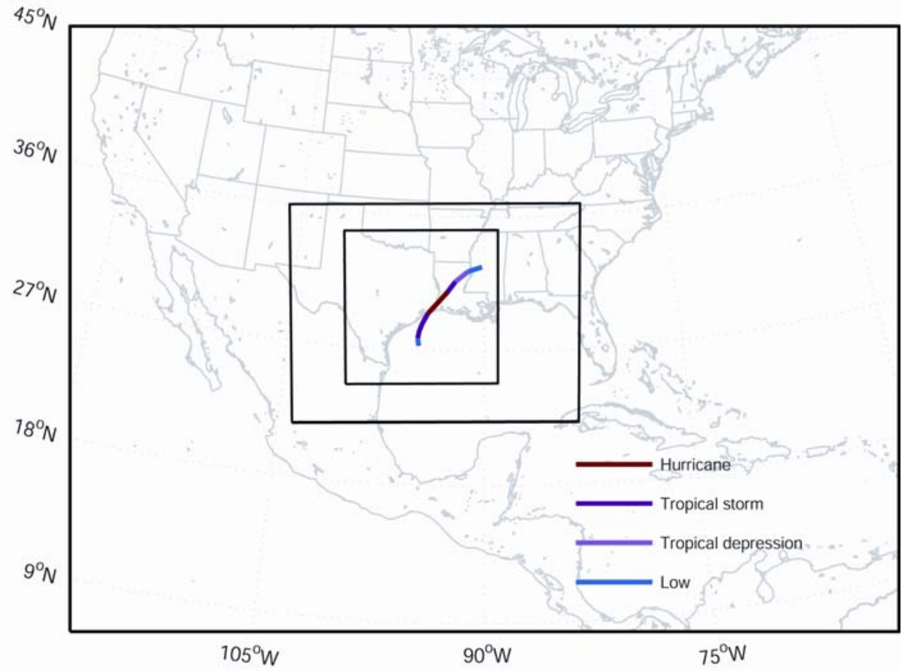

Figure 3.1. The WRF domain configuration and track of Humberto. Domain 1 serves as the background map and the nested domains 2 and 3 are outlined in black. The post-analysis best track of the storm is shown and color coded according to post-analysis intensity.

recognized it as a potential trigger for cyclogenesis as early as the afternoon of 10 September. Convection associated with the disturbance had access to convective instability and low-level moisture (e.g., Fig. 3.3b-c), and the convection gradually became more widespread and organized preceding Humberto's genesis (Fig. 3.4). In addition to increasing convection favoring genesis, the *local* genesis environment was rich with necessary deep moisture by 0900 UTC 12 June (Fig. 3.3b-c). Yet, on a larger scale, significantly drier air associated with a frontal boundary was not far north of the developing cyclone and could certainly hinder genesis if it entrained into the circulation (Fig. 3.3a-b; also note the wind shift and temperature gradients in Fig. 3.3c). Additional drier pockets at 700 hPa were also evident farther south over the Gulf of Mexico (Fig.

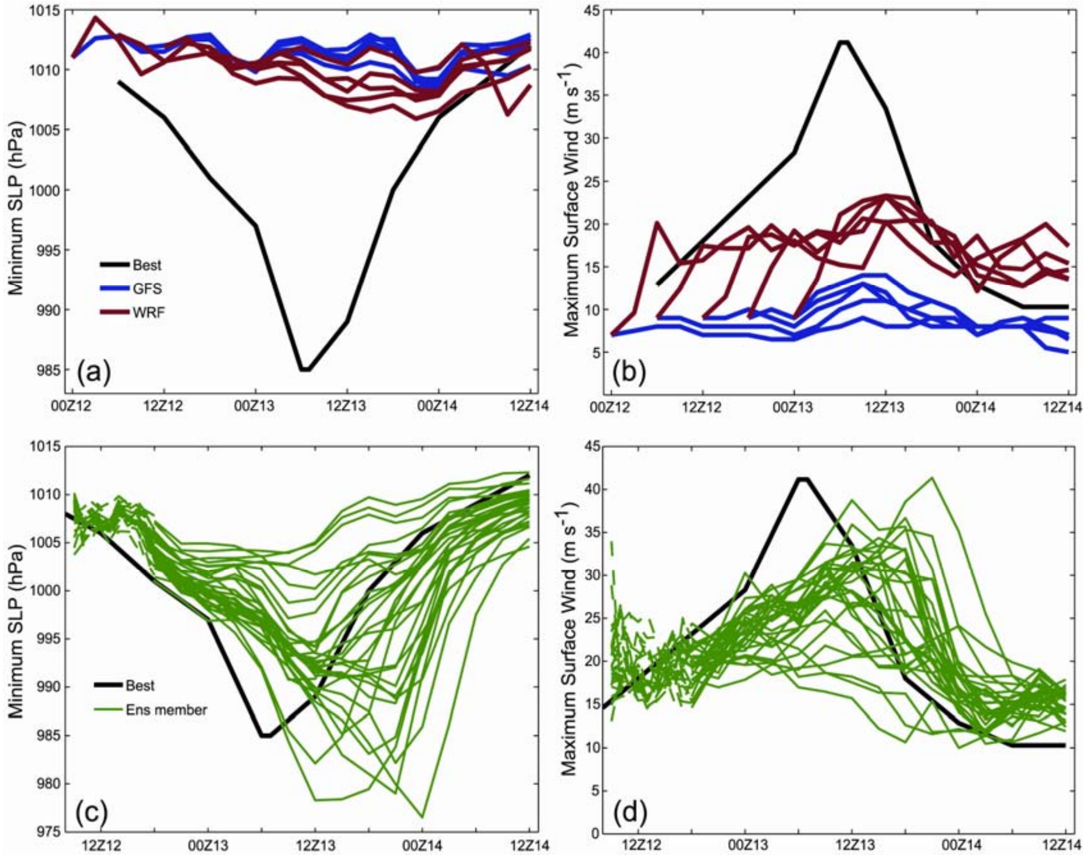

Figure 3.2. A comparison of the best-track intensity estimate (black) with the time evolution of minimum SLP (a,c) and maximum surface wind (b,d) analyses and forecasts (this same data is shown in Figs. 3 and 11 of Z08). Panels (a) and (b) show forecasts from the operational GFS (blue) and 4.5-km WRF models (red) starting every 6 hours from 0000 UTC 12 September to 0000 UTC 13 September. In panels (c) and (d), time evolution of SLP and wind from individual members of the EnKf analysis (green dashed) and subsequent ensemble forecast (green solid).

3.3a), and they too could potentially hinder genesis. Finally, the ample convection in the genesis region likely helped reduce upper level PV and build an upper level ridge above the circulation center (Fig. 3.3d). Associated with the ridge was a minimum in 200-850-hPa shear (Fig. 3.3d), and mean shear within 300 km of the circulation center was favorable for intensification (Fig. 3.5).

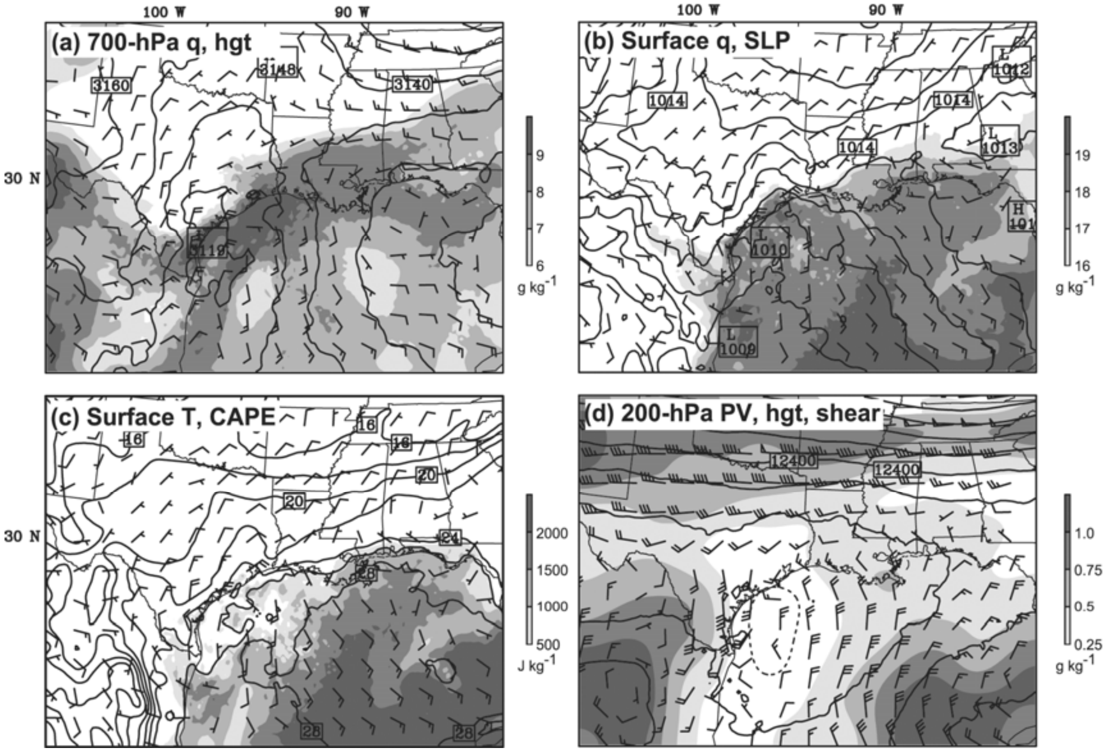

Figure 3.3. The 0900 UTC 12 June EnKF analysis of thermodynamic, height, PV, wind, and shear fields. Specifically, 700-hPa mixing ratio (filled every 1 g kg^{-1}), height (contoured every 10 m), and wind (full barb represents 5 m s^{-1}) are shown in (a), surface mixing ratio (filled every g kg^{-1}), wind and SLP (contoured every 1 hPa) are shown in (b), surface temperature (contoured every 2 C), wind, and MUCAPE (filled every 500 J kg^{-1}) are shown in (c), and 200-hPa height (contoured every 20 m), PV (smoothed, filled every 0.25 PVU for positive values and dash-contoured every 0.25 PVU for negative values), and 200-850-hPa shear (full barb represents 5 m s^{-1}) are shown in (d).

3.1.2. Forecast challenges

Humberto’s development and evolution posed serious operational forecast challenges. All operational models failed to capture the storm’s rapid genesis and deepening to a formidable Category 1 hurricane. For example, Fig. 3.2 demonstrates the severity of the failure of multiple real-time forecasts by the operational global forecast system (GFS) running at National Centers for Environmental Prediction (NCEP). The

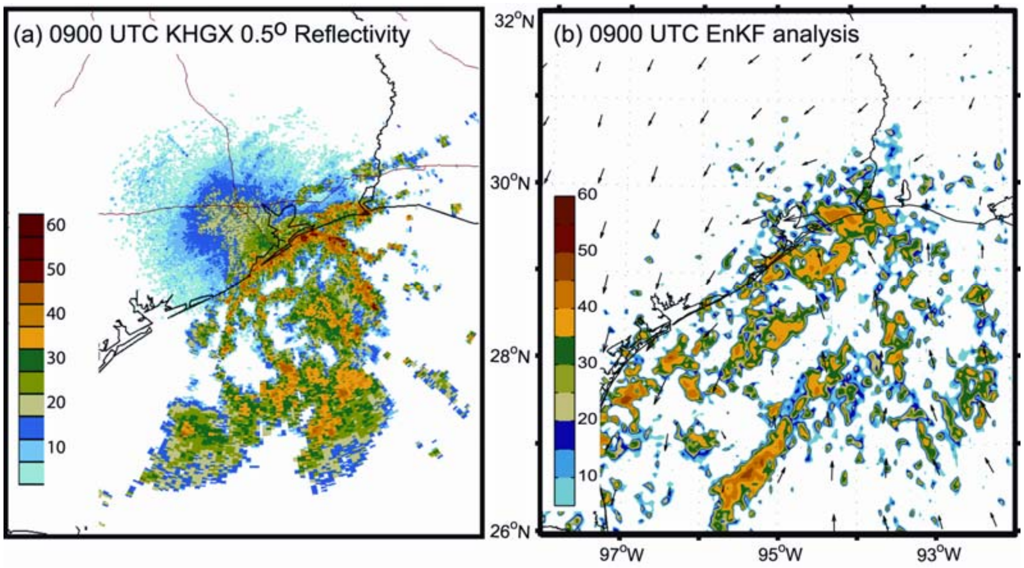

Figure 3.4. Radar reflectivity at the 0.5° elevation angle from the KHGX WSR-88D radar (a) and the EnKF-analysis reflectivity (b) at the same time. The two panels cover approximately the same domain, and reflectivity values are colored similarly in each panel. EnKF-analyzed surface wind vectors are shown in (b).

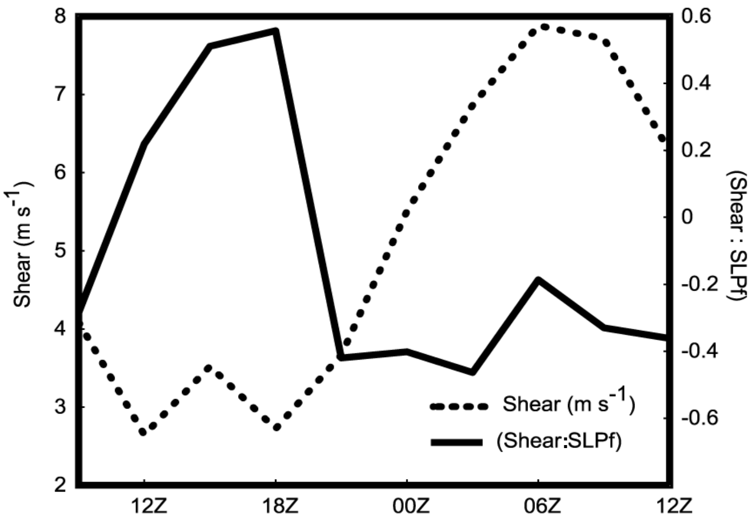

Figure 3.5. Wind shear (dotted) and the correlation between wind shear and final storm intensity (*SLPf*) (solid) from 0900 UTC 12 September until 1200 UTC 13 September. Wind shear is computed as the difference between the mean 200 and 850-hPa wind vectors averaged within 300 km of the circulation center in a Lagrangian coordinate system. Until 1800 UTC, shear is calculated from the EnKF analysis, and after that time it is calculated from the ensemble forecast.

Weather Research and Forecast (WRF) model also failed in post-event, 4.5-km, cloud-resolving simulations that were initialized with the GFS analyses with lead times every 6 h from 6 to 48 h.

The failure of all operational models to capture the rapid intensification of Humberto led to significant operational intensity forecast errors. First, while tropical weather outlooks issued by the NHC mentioned the preceding disturbance for several days prior to genesis, none mentioned the possibility that depression formation was imminent. Also, though the official track errors were less than long-tem average track error, average 12-h intensity forecast error was 300% of long-term average intensity error with the same lead time. This failure highlights the current struggle to forecast rapid intensity change of tropical cyclones in general.

Zhang et al. (2008) (hereafter Z08) studied Humberto with an ensemble Kalman filter (EnKF) data assimilation system coupled with the WRF model (see Z08 for a review of past performance of such data assimilation setups). They found that the EnKF assimilation of radial velocity observations from three WSR-88D radars along the gulf coast resulted in analyses that accurately depicted the best-track position and intensity of Humberto. In addition, EnKF-initialized deterministic (not shown) and ensemble (Figs. 3.2 and 3.6) forecasts outperformed operational forecasts by predicting the rapid formation and intensification of the hurricane. Despite the benefits of data assimilation, the large ensemble intensity spread in Fig. 3.2 exemplifies the significant uncertainty associated with the intensity forecast. The generally good ensemble performance and large uncertainty render this an ideal opportunity to test the results of Chapter II.

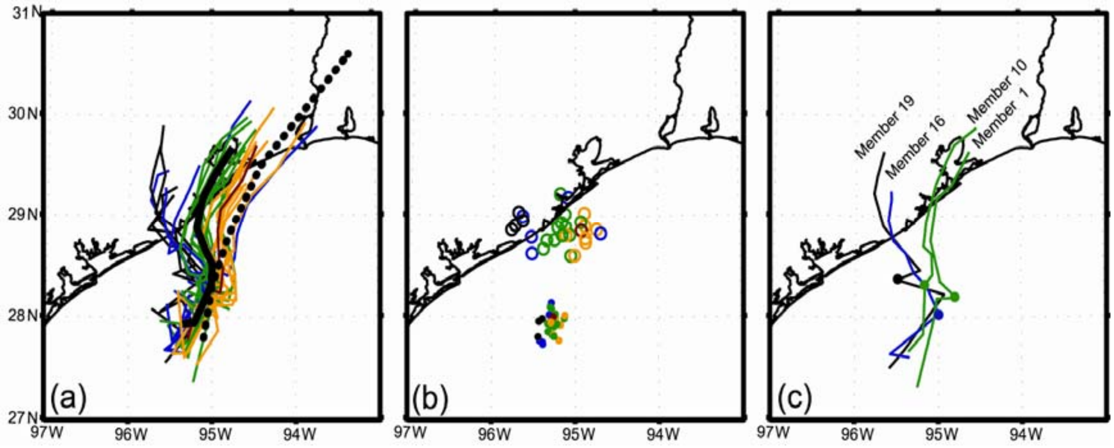

Figure 3.6. The ensemble forecast tracks and the best track analysis. Tracks of all ensemble members (thin black or colored lines), the ensemble mean position (thick black solid line), and the best-track analysis (thick black dotted line) are plotted every 3-h from 1200 UTC 12 June to 1200 UTC 13 June in (a). Panel (b) depicts the mean 1200-1800-UTC analysis position (computed from hourly data) with filled dots and the 0600 UTC forecast position with circles. Panel (c) shows tracks from select members with the 1800-UTC (final EnKF analysis) position noted by filled dots. Color represents maximum intensity of the cyclone for the given member (black, <25 m s^{-1}; blue <30 m s^{-1}; green <35 m s^{-1}; yellow <40 m s^{-1}; red >40 m s^{-1}). Before 1800 UTC, position is calculated from the EnKF analysis, and thereafter it is calculated from the ensemble forecast.

3.2. Methodology

This section outlines methodology specific to this particular chapter, including the forecast model and ensemble initialization method. In general, this chapter will employ methodology very similar to that of Chapter II in order to understand both the predictability and dynamics of the genesis and evolution of Humberto. However, as will become evident, some methods have been refined here to understand what factors on *both local and regional scales* favor cyclogenesis.

3.2.1. Forecast model and data assimilation methods

The EnkF-WRF analyses and ensemble forecasts of Z08 will be analyzed here to understand Humberto's genesis dynamics, and a brief synopsis of the setup follows. The outer, 40.5-km WRF domain covers the contiguous United States with 160×121 grid points and two nested domains cover the central United States with 160×121 (253×253) grid points and a grid spacing of 13.5 (4.5) km (Fig. 3.1). All model domains have 35 vertical layers, and the model top is set at 10 hPa. The physical parameterization schemes include the Grell-Devenyi cumulus scheme (Grell and Devenyi 2002), WRF Single Moment 6-class microphysics with graupel (Hong et al. 2004), and the Yonsei State University scheme (Noh et al. 2003) for planetary boundary layer processes. Random, balanced, large-scale perturbations are added to the National Centers for Environmental Prediction (NCEP) Global Forecast System (GFS) analyses at 00Z 12 September to create initial conditions for a 30-member ensemble forecast that is integrated forward until 0900 UTC. Data assimilation of thinned and quality controlled radial velocity observations from the Corpus Christi (KCRP) and Houston-Galveston (KHGX) radars begins at 0900 UTC, and assimilation of data from Lake Charles (LCH) begins a few hours later. Assimilation proceeds in hourly cycles until 1800 UTC 12 June, at which point an EnKF-initialized ensemble forecast is integrated forward. For a full review of the methodology used in this data assimilation system, see Z08.

The use of an EnKF for the analyses here is a significant difference from the methodology of Chapter II. In the ensemble analysis of the 2004 gulf low, the cold-start technique was used, which likely resulted in some artificial overreaction of initial convection to ambient convective instability during the model spin-up period. The EnKF analyses used in this chapter is a so-called “hot start” technique because the analysis contains active moist convection (see Fig. 3.4). As will be seen later in this chapter, the difference in techniques *does* have some effects on results.

3.2.2. Correlation

As in Chapter II, linear correlation is used here to elucidate dynamics, but verbal descriptions of correlation will be somewhat different than in that study. Since the size of the ensemble used here is larger (i.e., 30 vs. 20 members), confidence that a particular level of correlation is statistically different from 0 is higher here. This chapter continues using the Chapter II correlation benchmarks of 0.3, 0.5, and 0.7, and these values are significant with roughly 90%, 99.5%, and 99.99% confidence, respectively. Verbal descriptions of the correlation values will respectively be ‘correlated’, ‘strongly correlated’, and ‘very strongly correlated’.

3.2.3. Lagrangian and Eulerian computations

This study also largely follows the convention of Chapter II by making use of a Lagrangian, storm-centered coordinate system, but advancements are made upon the methodology. Many of the ensemble-mean and correlation computations use the Lagrangian system in which the analysis domain is centered upon the larger scale circulation center in each ensemble member. However, while Lagrangian variables in Chapter II were averaged in a square box, many variables here are averaged in a radial

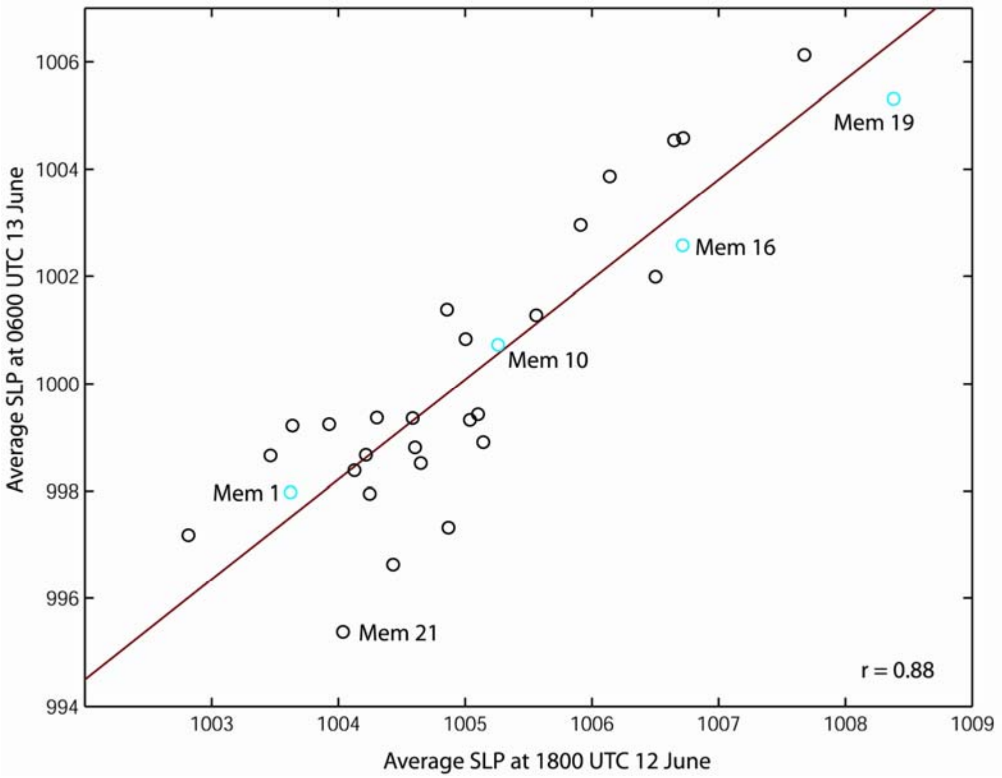

Figure 3.7. A scatterplot of *SLPi* at 1800 UTC 12 June vs. *SLPf*. The best fit line is shown in dark red, and members 1, 10, 16, and 19 are labeled and shaded in cyan (these members are further analyzed in the text). The correlation coefficient is shown in the lower right corner.

coordinate system with averaging radii increments of 20 km. For example, variables are averaged at all grid points falling within the first 20 km of the center to produce near-center means (and correlation), and they are also averaged at points falling in 20-km annuli (e.g., from 20 to 40 km, etc.) to show how the azimuthal mean (and correlation) varies with distance from the center. As in Chapter II, many variables are correlated with area-average sea-level pressure (SLP) at a time when the storm is mature. In this case, that time is 0600 UTC 13 June, which is before most ensemble members make landfall (although the results are very similar with a slightly later time when the mean strength is higher but more ensemble members have storms that have made landfall). The averaging area for SLP at 0600 UTC (hereafter in this chapter, *SLPf*) is within the first 20 km; this radius was chosen largely because it produces *SLPf* that exhibits the best time-lag correlation with SLP averaged over the same area at other earlier times (hereafter in this chapter, *SLPi*). For instance, in Fig. 3.7, (*SLPi*:*SLPf*) at 1800 UTC 12 June is nearly 0.9. Finally, as in Chapter II the negative of *SLPi* and *SLPf* will be in correlation computations so that positive correlation with *SLPf* implies that a factor favors intensification.

There are times in this study when correlation with azimuthally averaged variables does not give necessary insight, so that methodology is not ubiquitously used here. For example, it is interesting to know how *SLPf* is affected by large-scale Eulerian fields before genesis. In addition, it is sometimes necessary to investigate specific features in one quadrant or another of the circulation; in these cases correlation and means will be computed for area averages that only encompass certain features of interest. These instances will be described in more detail as their use becomes necessary.

3.3. Ensemble performance and predictability

Ensemble spread grows much more rapidly in the case of Humberto than in the 2004 gulf low. For instance, the minimum SLP envelope here spans nearly 30 hPa after 18 h of forecast time (i.e., by 1200 UTC 13 June in Fig. 3.3c), but the envelope in the gulf low was only 14 hPa after 36 h (when sampled on the 3.3-km grid). As a result of the larger intensity spread in the Humberto case, RM-DTE error grows much faster. In Fig.

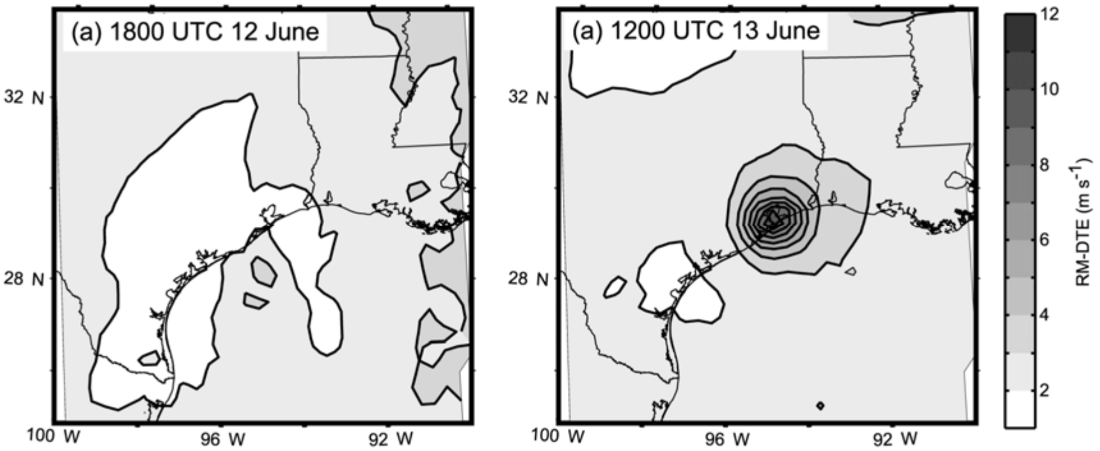

Figure 3.8. RM-DTE (every 1 $\mathrm{m\,s^{-1}}$) for the approximate area of domain 3 at 1800 UTC 12 June (a) and 1200 UTC 13 June (b). Sampling is limited to every 7 grid points (31.5 km) in order to facilitate comparison with Fig. 2.5, which shows RM-DTE sampled to a 30-km grid.

3.8, RM-DTE increases from about 3 $\mathrm{m\,s^{-1}}$ at 1800 UTC 12 June to over 10 $\mathrm{m\,s^{-1}}$ by 1200 UTC 13 June (to facilitate comparison to Chapter II, RM-DTE has been sampled every 7 grid points, or 31.5 km, in Fig. 3.8). This >300% RM-DTE increase occurs in only half the time of a similar percentage increase in Chapter II (see Fig. 2.5). Thus, forecast uncertainty was considerably higher with Humberto than with the 2004 low.

As mentioned in the introduction, the current ensemble captures the genesis and rapid intensification of Humberto, a feat not accomplished by operational models. To further demonstrate ensemble performance, Figs. 3.9 and 3.10 respectively show observed reflectivity from the time around Humberto’s landfall and derived reflectivity at the landfall time of ensemble members 1, 10, 16 and 19 (these members generally span the ensemble in terms of *SLPf* in Fig. 3.7). Members 1 and 10 (Fig. 3.9a-b) both have fairly strong cyclones with well-organized central cores. Member 1, which has a

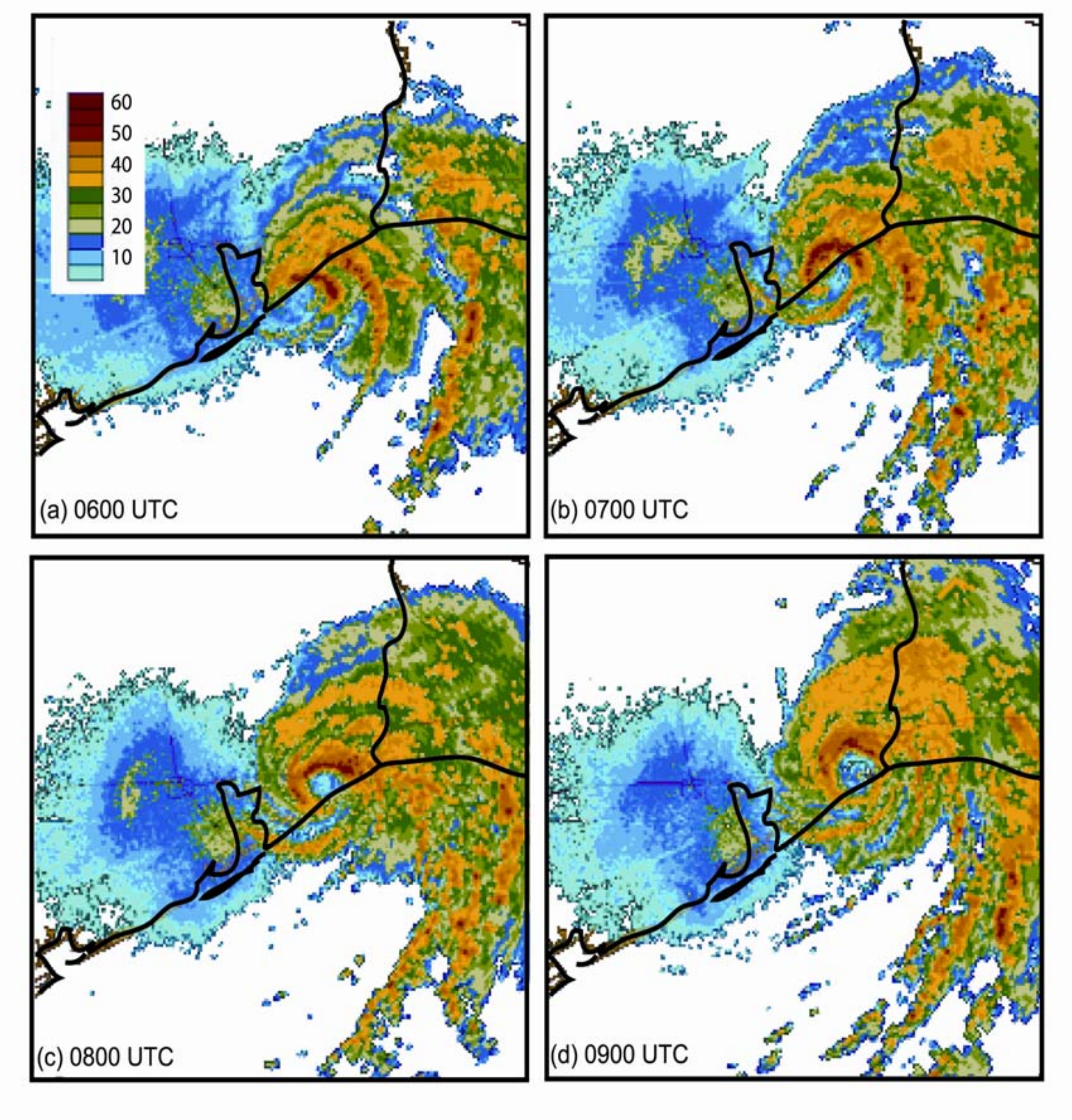

Figure 3.9. Radar reflectivity at the 0.5° elevation angle from the KHGX WSR-88D radar at 0600 (a), 0700 (b), 0800 (c), and 0900 (d) UTC 13 June.

50% closed eyewall, best represents the central reflectivity structure of Humberto at its landfall, but member 10 performs better with the stratiform precipitation to the northeast of the core. In terms of minimum SLP, the cyclones in both members are somewhat weaker than Humberto at its landfall, but other storms in the ensemble do obtain lower

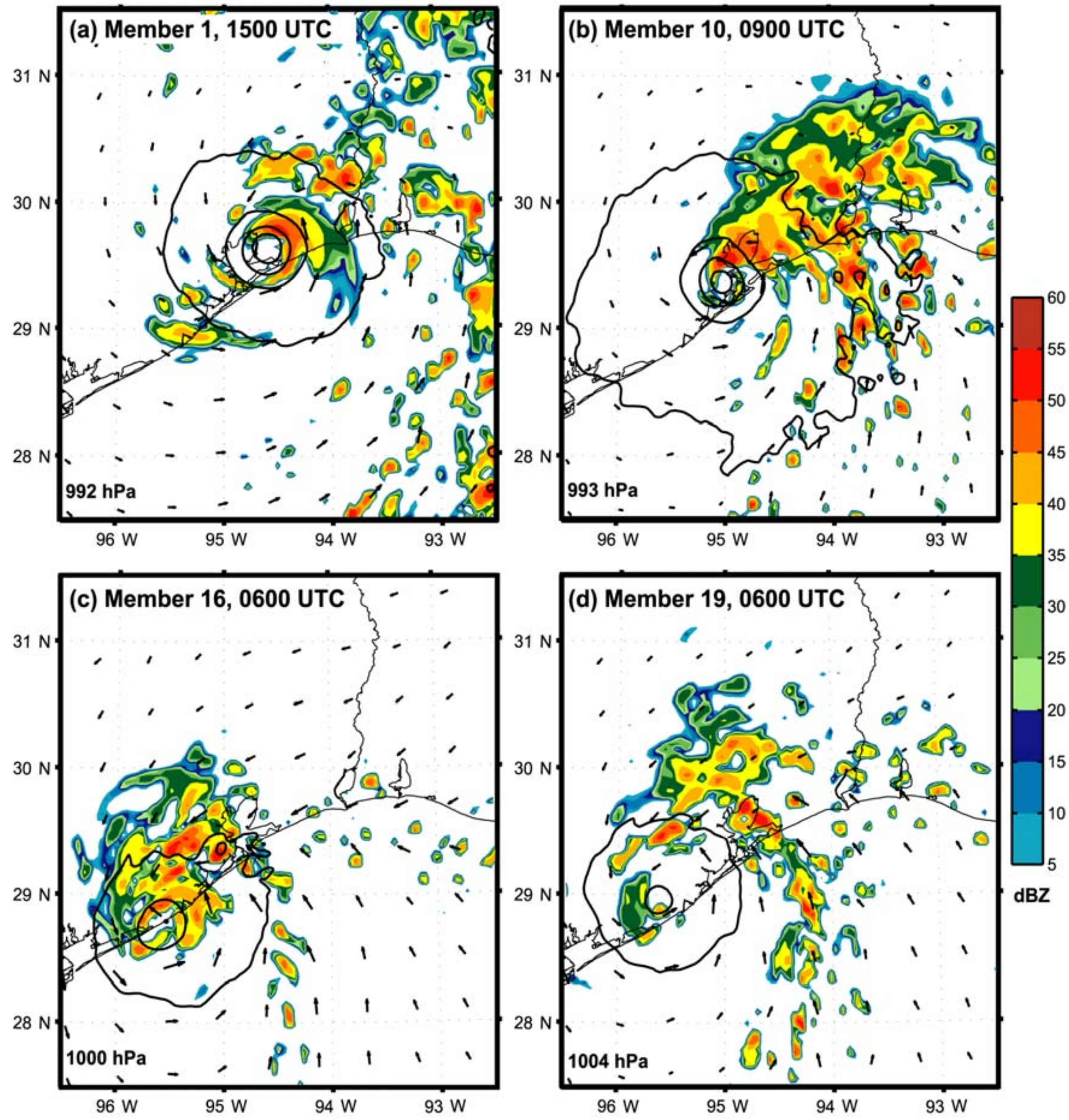

Figure 3.10. Derived reflectivity from ensemble members 1 (a), 10 (b), 16 (c), and 19 (d) at the approximate time their storms make landfall on 13 June. Surface wind vectors and SLP (contoured every 5 hPa) are also shown, and the minimum central SLP is shown in the bottom left corner of each panel.

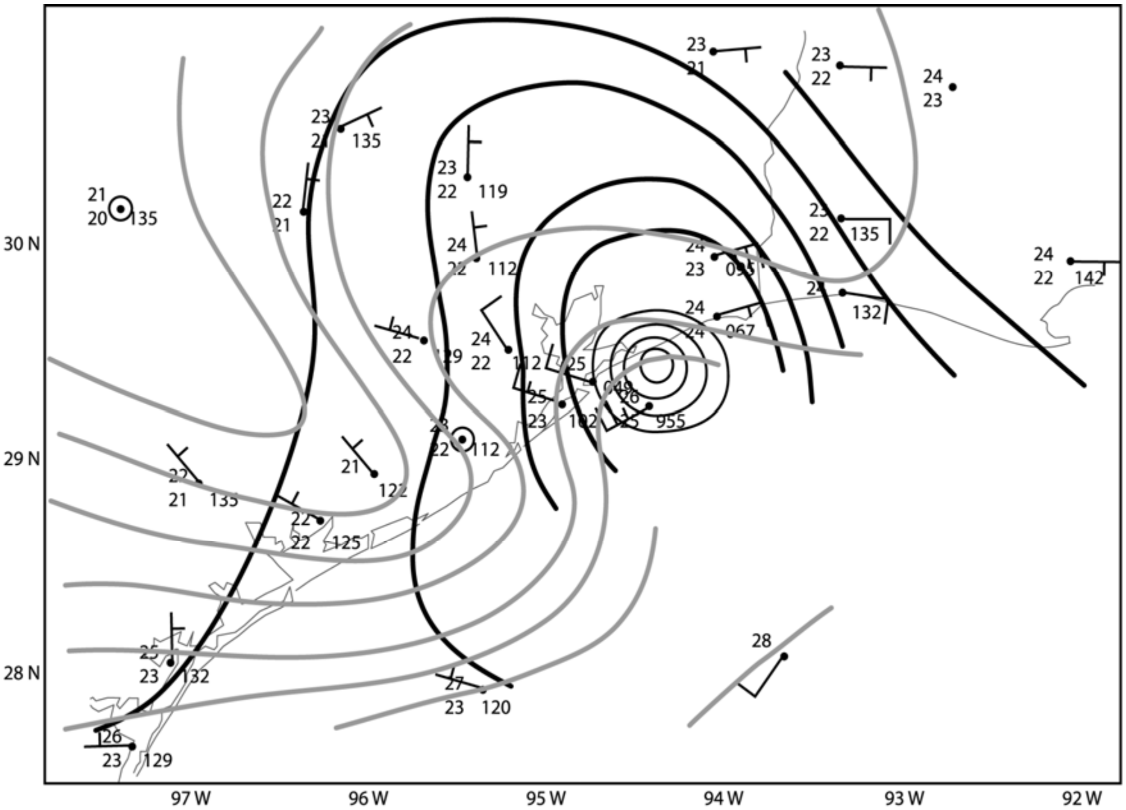

Figure 3.11. A mesoscale surface analysis from 0600 UTC 13 June, just prior to Humberto's landfall. Full wind barbs are 5 m s^{-1} and analyzed fields are as follows: pressure is contoured every 5 hPa from 990 to 1005 hPa (thin black lines) and every 1 hPa at and above 1010 hPa (thick black lines), and temperature is contoured every 1 C. Observations outside the depicted domain and at both earlier and later times were used to construct the analysis.

central pressure (see Fig. 3.2c). The one noticeable problem with the strongly developing ensemble members in Fig. 3.2c-d is that they strengthen the storm too slowly. Humberto's actual central pressure falls below the lower limit of the ensemble envelope until its landfall, after which many ensemble members obtain a similar central pressure. Meanwhile, member 16 (Fig. 3.9c) does a mediocre job at representing Humberto's intensity and structure, and member 19 (Fig. 3.9d) does a poor job. Yet, both members perform better than did the operational models (e.g., Fig. 3.2a).

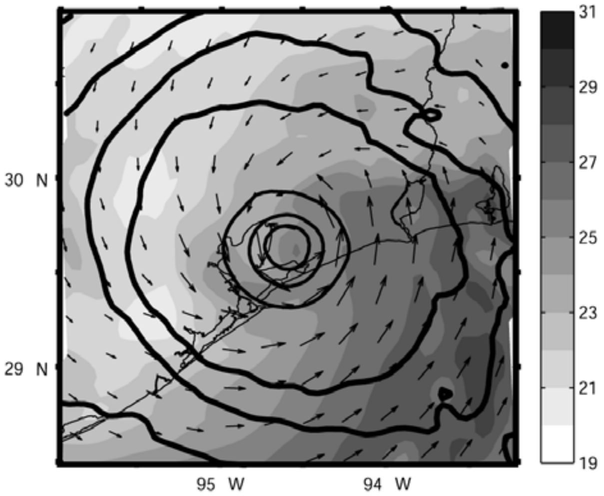

Figure 3.12. Surface temperature (shaded every 1 C), pressure (contoured as in Fig. 3.11), and wind vectors at 1500 UTC 13 June for member 1.

In addition to accurately portraying Humberto's intensity, certain members of the ensemble also accurately capture the storm's interaction with the nearby surface front. For instance, Fig. 3.11 shows a mesoscale analysis of Humberto shortly before the hurricane made landfall, and Fig. 3.12 shows the corresponding member 1 forecast for 1500 UTC 13 June shortly after the cyclone in that member makes landfall. The observations in Fig. 3.11 reveal that Humberto's circulation had begun entraining cool post-frontal air before landfall, which might explain the observed lack of convection on the southwest side of the storm (e.g., Fig. 3.9a). The forecast temperature field in Fig. 3.12 exhibits a very similar wavelike pattern to that observed in Fig. 3.11, and the temperature difference across the front is about the same in both figures. In addition, the simulated storm similarly lacks convection on its southwest side. Finally, a wavelike field seen in both dew-point observations and the simulation (not shown) indicates that the air entraining into the circulation from the northwest was also drier than that of its immediate genesis environment.

The ensemble captures Humberto’s general track, but it moves the storm northeastward too slowly. For example, in Fig. 3.6 the actual position of the cyclone at 1200 UTC 13 June is well northeast of all the ensemble members. This error is partly a result of the left track deviation that takes place after 1800 UTC 12 June (i.e., after the final EnKF analysis) in many of the ensemble members. Of the four members shown in Fig. 3.6c, the storm in member 10 is the only one to not exhibit a leftward turn, and it is the farthest northeast at 1200 UTC 13 June. One result of this error is that many members make landfall 6-12 h later than did Humberto, which is evident by the end of their intensification cycles in Fig. 3.3c-d.

3.4. Ensemble mean and probabilistic dynamics

The correlation statistics here reveal that the processes that control Humberto’s simulated final intensity begin very early in the analysis period and that the *SLPf* variance is largely determined by 1800 UTC 12 June. For example, Fig. 3.13 shows azimuthally averaged PV in a Lagrangian system and (*PV*:*SLPf*). Temporally and spatially consistent (*PV*:*SLPf*) is established by 1300 UTC, and the most quickly developing storms have a well-defined PV tower through 9 km by 1500 UTC. Furthermore, (*SLPi*:*SLPf*) at 1800 UTC is almost 0.9 (Fig. 3.7). Because 1800-UTC strength differences explain a large majority of *SLPf* variance, the processes that act to strengthen the cyclone before 1800 UTC (discussed below) must be crucial in

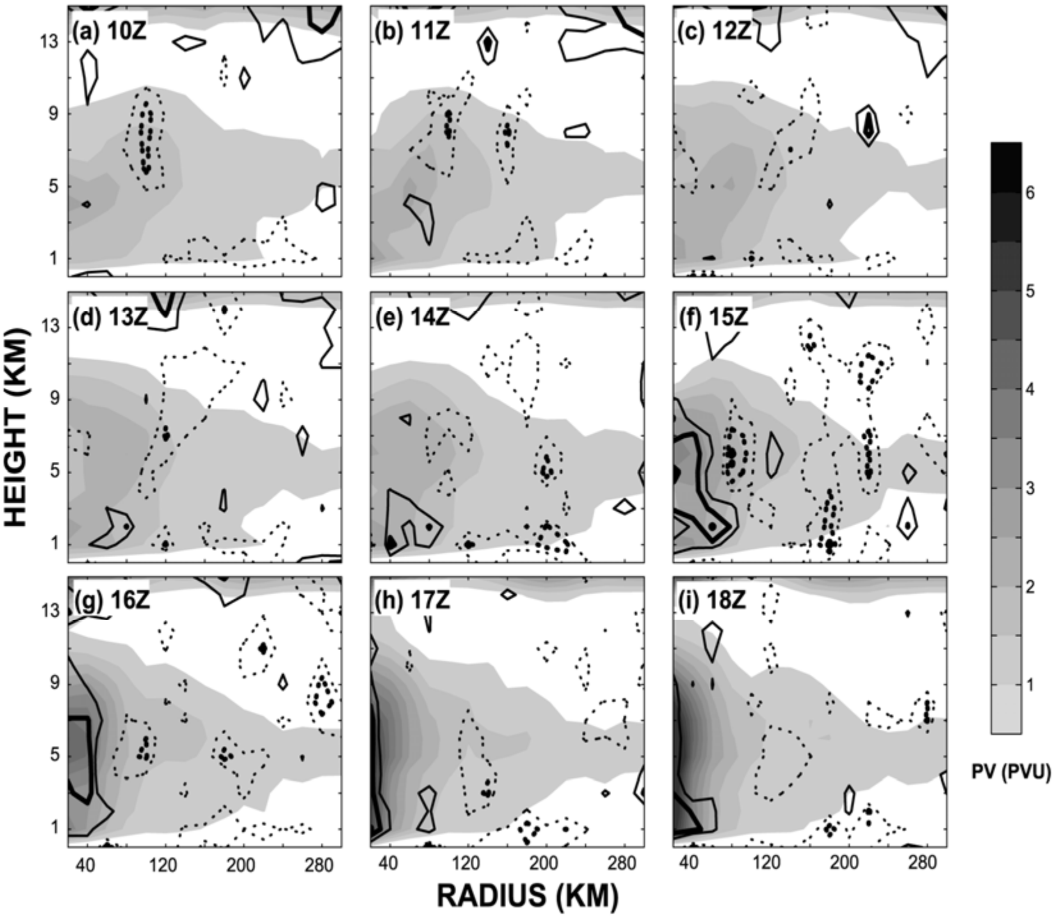

Figure 3.13. The evolution of ensemble-mean PV and (*PV*:*SLPf*) as a function of radius and height in a Lagrangian, storm centered coordinate system. PV is averaged in 20-km annuli and shaded every 0.5 PVU. The average is computed before the correlation, which is contoured in black at magnitudes of 0.3, 0.5, and 0.7 with increasing line thickness indicating increasing magnitude (dotted black lines indicate negative correlation). Each panel represents a different time, every hour from 1000 UTC until 1800 UTC 12 June.

determining the final strength. Meanwhile, processes after 1800 UTC generally only act to increase existing differences. The dynamical examination is therefore divided to show how distinct mechanisms act to determine intensity differences by 1800 UTC and the means by which post-1800 UTC spread increases.

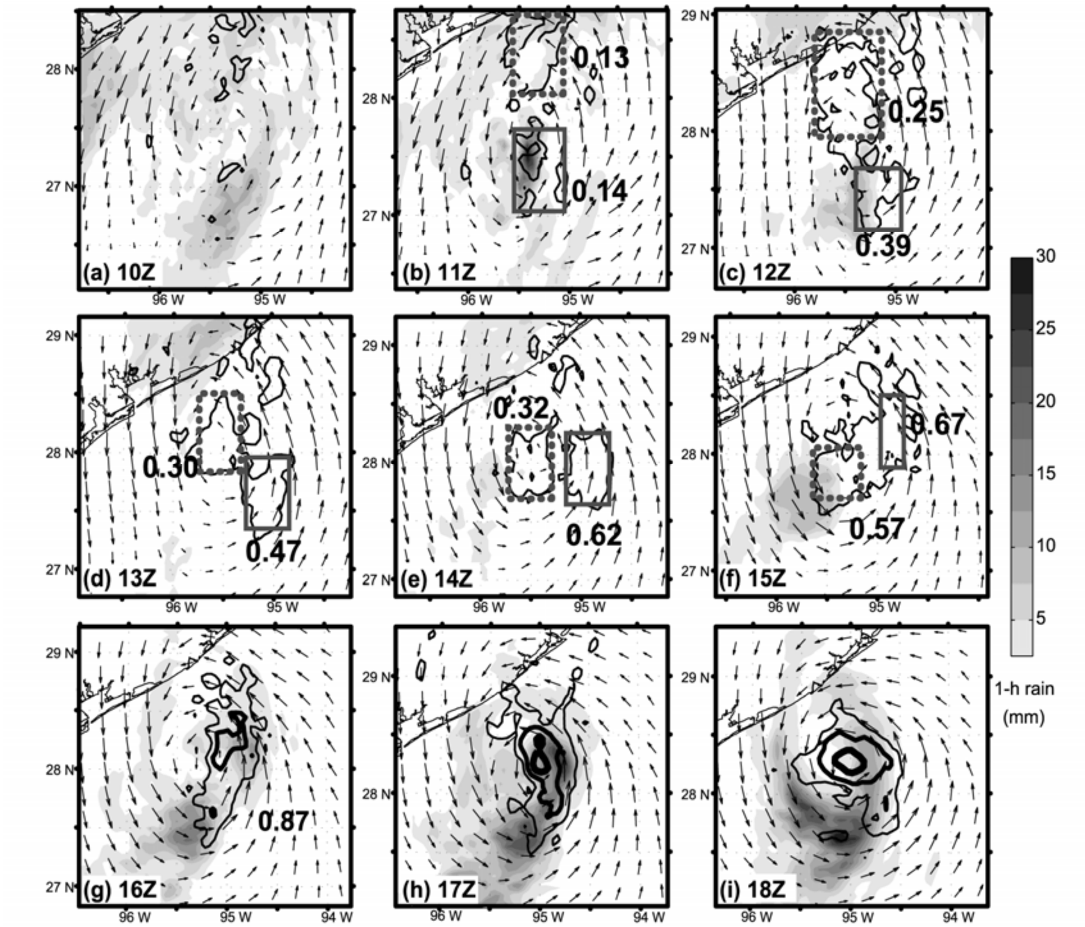

Figure 3.14. Ensemble-mean 1-h precipitation (shaded every 5 mm), surface wind vectors, and 2-km PV (contoured at 2, 4, and 8 PVU). The boxes outline averaging regions of PV anomalies A (solid) and B (dashed) mentioned in text. The associated correlation between area-average PV and *SLPf* is also indicated next to each box, and (*PV16*:*SLPf*) is indicated in panel f. Analysis is completed in a Lagrangian coordinate system with the center of each panel at the ensemble mean center location.

3.4.1 Early convection and details of PV tower building

Between 1000 and 1100 UTC, two ensemble-mean, 2-km PV anomalies appear in areas of active convection and grow in both strength and areal extent thereafter. When the anomalies first appear, they have little relationship to the ultimate storm strength, but

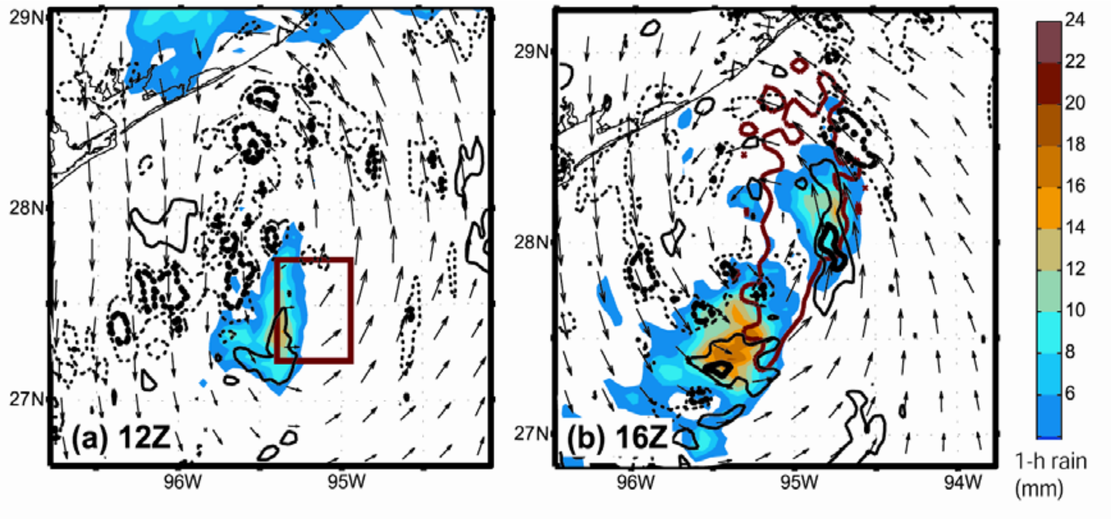

Figure 3.15. Ensemble-mean 1-h precipitation (color filled every 2 mm), surface wind vectors, and the correlation (contoured as in Fig. 3.13) between precipitation and *PVA* (a) and *PV16Z* (b). In panel (a), precipitation is from 1100 to 1200 UTC, and in panel (b) the precipitation is from 1500 to 1600 UTC. The regions of *PVA* and *PV16Z* are outlined with red contours in panels (a) and (b) respectively.

correlation between their strength (determined by the area-average PV within the solid and dashed boxes in Fig. 3.14, respectively *PVA* and *PVB*) and *SLPf* quickly increases. Strong (*PVA*:*SLPf*) and (*PVB*:*SLPf*) by 1500 UTC indicates that variance in the strengths of these anomalies ultimately explains much of the variance in *SLPf*.

How do these low-level anomalies become well correlated to *SLPf*? In anomaly A, the change in (*PVA*:*SLPf*) between 1100 and 1200 UTC seems to be largely a dynamic response to the amount of precipitation (i.e., latent heating) in its vicinity. Figure 3.14 shows that high precipitation totals encompass anomaly A as it develops, and precipitation totals on the southwest side of anomaly A from 1100 to 1200 UTC are significantly correlated to *PVA* at 1200 UTC (Fig. 3.15a). Standard deviation of *PVA*

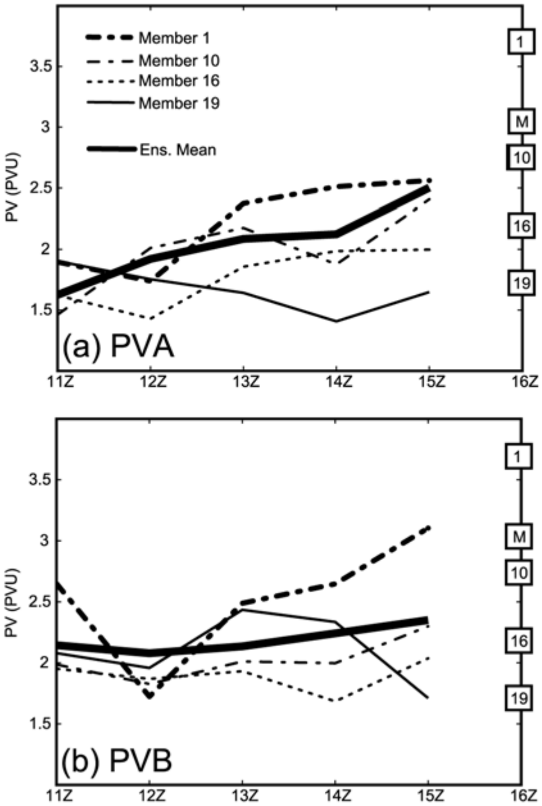

Figure 3.16. The evolution of PVA (a) and PVB (b) is shown for the ensemble mean (thick solid) and members 1 (bold dash-dot), 10 (thin dash-dot), 16 (dotted), and 19 (thin solid) from 1100 to 1500 UTC 12 June. PV16Z is also shown for the mean (boxed 'M' at 1600 UTC) and same members (boxed with their respective numbers at 1600 UTC).

also doubles during this time period (evidence for this is in the increased spread for select members in Fig. 3.16a), and ensemble-mean *PVA* concomitantly increases (Fig. 3.16a). It thus appears that convection strengthens *PVA* and that varying convective intensity leads to varying *PVA*. Such is also the case for *PVB* between 1400 and 1500 UTC, when the mean and standard deviation of *PVB* and (*PVB*:*SLPf*) all increase in the presence of deep convection. Meanwhile, it seems that EnKF updates might lead to increases in (*PVA*:*SLPf*) and (*PVB*:*SLPf*) at other times. For example, there is no

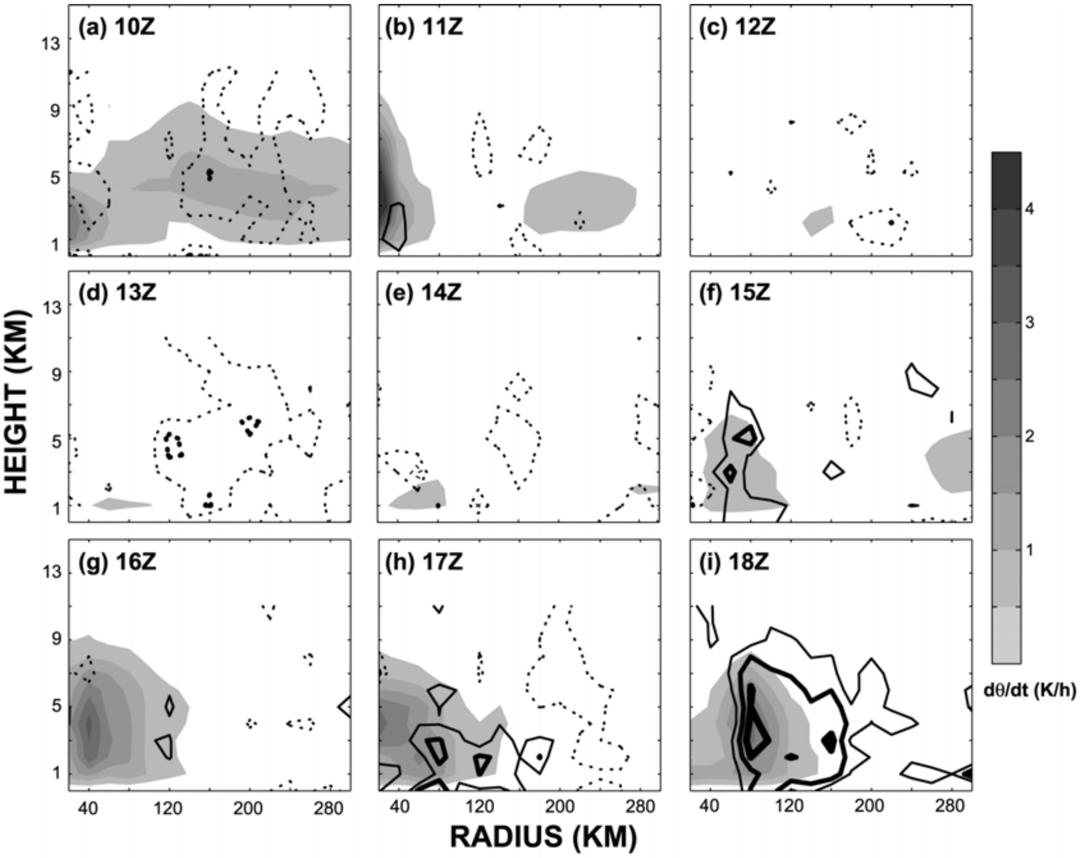

Figure 3.17. The evolution of ensemble-mean condensational heating (*CON*) and (*CON*:*SLPf*) as a function of radius and height in a Lagrangian, storm centered coordinate system. *CON* is averaged in 20-km annuli and shaded every 0.5 $\mathrm{K\,h^{-1}}$. The average is computed before the correlation, and the correlation is contoured as in Fig. 3.13. Each panel represents a different time, every hour from 1000 UTC until 1800 UTC 12 June.

precipitation associated with the increase in (*PVB*:*SLPf*) between 1100 and 1200 UTC or (*PVA*:*SLPf*) between 1300 and 1400 UTC. With no apparent dynamic mechanism to increase correlation in Fig. 3.14, EnKF updates are a possible culprit.

The strength of the single PV anomaly that results from the 1500 UTC merger of anomalies A and B in the ensemble mean is very strongly correlated to *SLPf*. At 1600 UTC, correlation between mean PV inside the mean 2-PVU isopleth (hereafter in this chapter, *PV16Z*) and *SLPf* is 0.87 (see Fig. 3.14); this means that 75% of *SLPf* variance can be explained by variance of *PV16Z*. Furthermore, Fig. 3.13 shows that significant (*PV*:*SLPf*) encompasses much of the troposphere starting at 1500 UTC, the time of the merger.

Simultaneous with the change in (*PV*:*SLPf*) is a remarkable change in PV strength due to widespread convection. From 1500 to 1700 UTC in Fig. 3.14, ensemble-mean positive PV strongly grows in both strength and areal coverage. Also, ensemble-mean *PV16Z* is significantly higher than either mean *PVA* or *PVB* at 1500 UTC (Fig. 3.16), and an increase in PV is evident throughout much of the troposphere from 1500 UTC onward in Fig. 3.13. Concomitant with the PV increase, two regions of high precipitation totals emerge near the center between 1400 and 1800 UTC in Fig. 3.14, and azimuthally averaged condensational heating increases dramatically (Fig. 3.17). *PV16Z* is strongly correlated to precipitation totals in these regions where they are high (Fig. 3.15b), and the correlation between *PV16Z* and mean antecedent 1-h precipitation within the 4-mm isopleth (i.e., the regions encompassed by the yellow line in Fig. 3.18, hereafter in this chapter, *PTOT16Z*[4]) is also strong. Thus most *PV16Z* variance can be explained by variance of *PVA*, *PVB*, and *PTOT16Z*.

---

[4] If the two large precipitation regions of *PTOT16Z* are considered individually, the northeastern region is more strongly correlated with *PV16Z*, but the southwestern region is more strongly correlated with *SLPf*. The differences are likely due to the location and duration of the convective events. The northeastern convection occurs more immediately in the *PV16Z* region and tends to produce stronger PV, but this convection is relatively short in duration. The southwestern convection region lasts through the afternoon hours, and while its initial PV anomaly is weaker, it continues to produce high-PV air that feeds into the center.

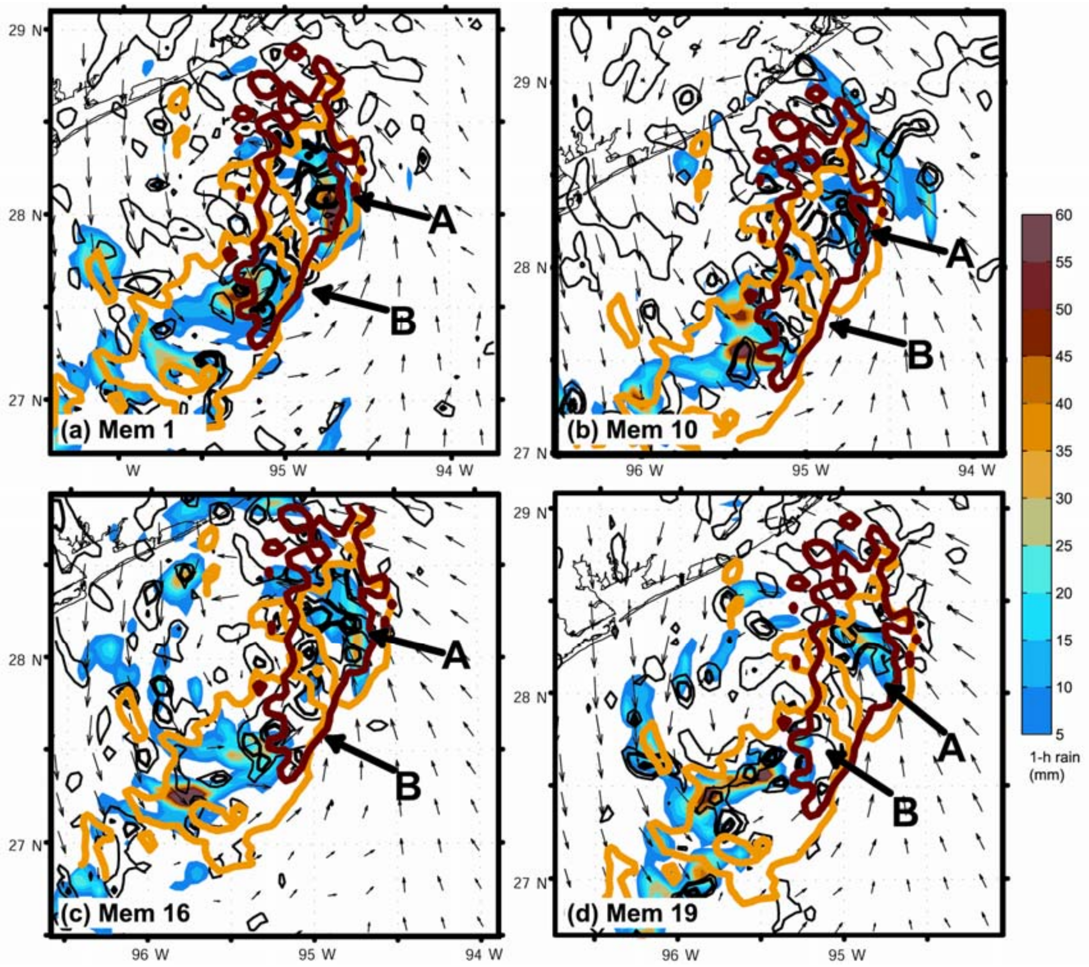

Figure 3.18. The relationship between 1-h precipitation (color filled every 2 mm) and PV (contoured at 2, 4 and 8 PVU) in members 1 (a), 10 (b), 16 (c), and 19 (d) at 1600 UTC 12 June. The region of *PV16Z* is outlined in red, and the region of *PTOT16Z* is outlined in yellow. ‘A’ and ‘B’ point roughly to the regions of PV anomalies A and B from the text. Surface wind vectors are also shown.

Figures 3.16 and 3.18 demonstrate how the above results relate to the individual ensemble members selected from Fig. 3.7. Member 1, which is strongest in terms of *SLPf* chosen from Fig. 3.7 for further analysis, has the highest *PVA* from 1300 UTC onward. Its *PV16Z* is also much higher than that of the other members (Fig. 3.18a).

PVA and *PVB* in member 19, on the other hand, weaken with time, and it is the weakest member further analyzed in terms of both *PV16Z* and *SLPf*. Simulations with higher *PV16Z* also tend to have heavier or more widespread precipitation within the *PTOT16Z* regions between 1500 and 1600 UTC; this is also best demonstrated by comparing members 1 and 19 (i.e., Fig. 3.18a,d). For example, member 1 has very strong precipitation maxima in both primary *PTOT16Z* regions that appear to be a source of the stronger and more widespread PV that advects into the *PV16*Z region. Meanwhile, member 19 has considerably less convection in the *PTOT16Z* region, especially around anomaly A (this is likely why PV in the anomaly A region of member 19 is so low).

Figure 3.19 shows how the PV and precipitation distribution present at 1600 UTC evolves in the ensemble members from Fig. 3.18. In members 1 and 10 (Fig. 3.19a-f), anomalies A and B are both well-defined at 1600 UTC. By 1700 UTC, A becomes clearly associated with the circulation center in both of these simulations, and B becomes increasingly deformed by A. Because anomaly A is strongest in member 1 at 1600 UTC, member 1 also has a larger area of strong PV at its center at 1800 UTC. In members 16 and 19 (Fig. 3.19g-m), anomaly B is also much more ill-defined and elongated at 1600 UTC. While the strength of the PV near the center is visually similar in members 10 and 16 at 1800 UTC (Fig. 3.19i,m), PV in member 19 is clearly less. Finally, the most notable differences in convection between these simulations occur south and southwest of their circulation centers (i.e., that initially associated with the southwestern *PTOT16Z* region). From member 16 to member 1, there is incrementally more precipitation in this area through 1800 UTC; this convection also generates PV that

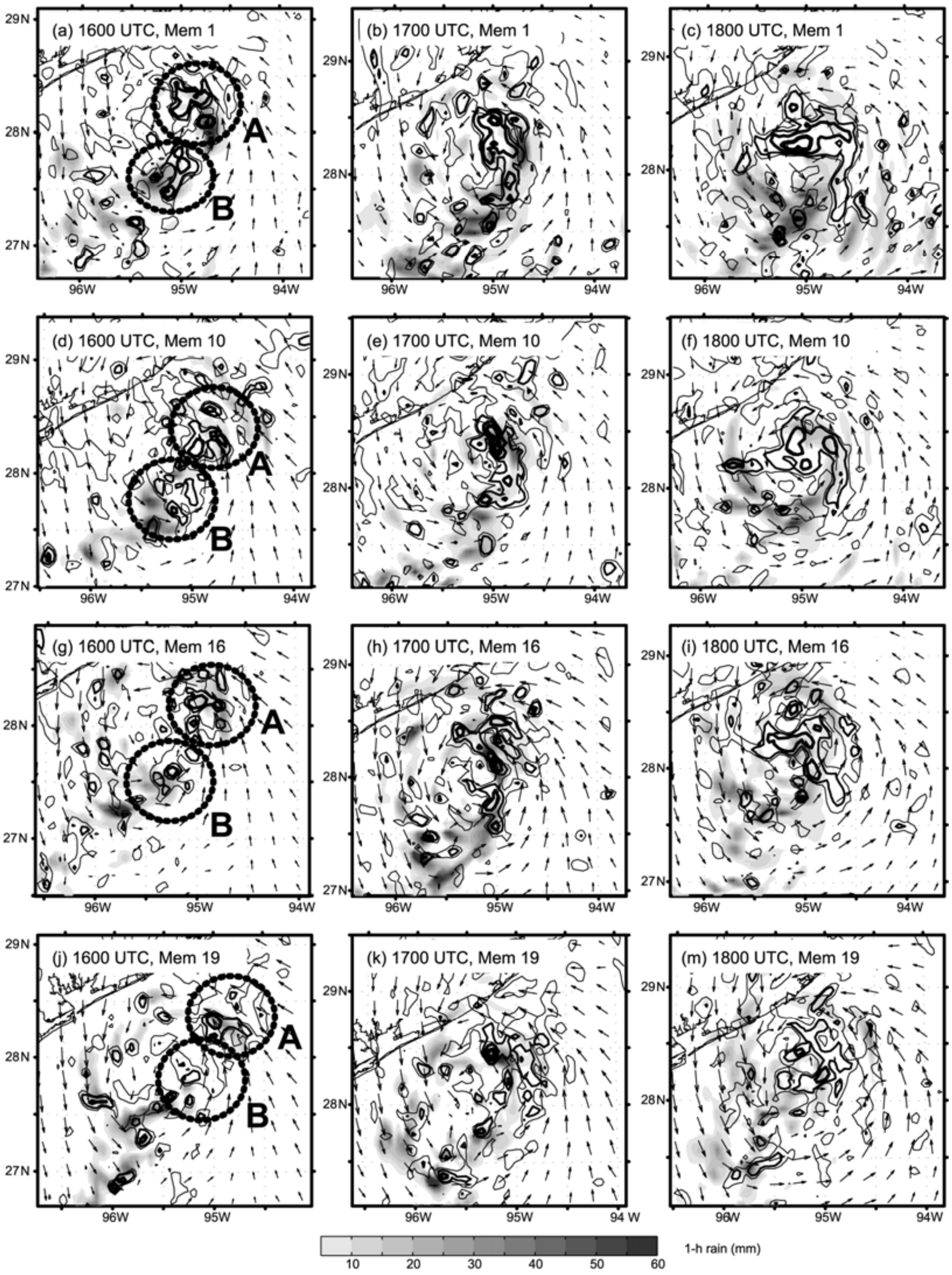

Figure 3.19. The evolution of surface winds vectors, 1-h precipitation (color filled every 10 mm) and PV (contoured at 2, 4, 8, and 16 PVU) for members 1 (a-c), 10 (d-f), 16 (g-i), and 19 (j-m) from 1600 to 1800 UTC 12 June. PV in encircled regions A and B roughly corresponds with PV anomalies A and B from the text.

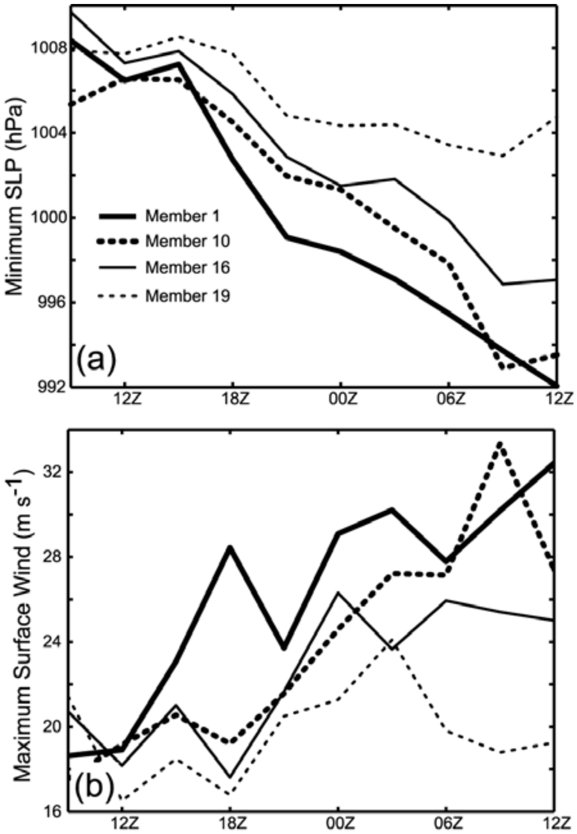

Figure 3.20. Minimum SLP (a) and maximum wind speed (b) for members 1, 10, 16, and 19.

apparently helps to further strengthen the stronger members. Contributing factors to the sustenance of the southwestern convective region will be discussed in the next subsection.

The differences in low-level PV organization at 1800 UTC are associated with varying intensities in terms of SLP and surface winds. For example, in Fig. 3.20 member 1 clearly has the strongest maximum winds and lowest SLP, which is consistent with its strong PV core. Members 10 and 16 have generally similar core PV strength and organization, which is less than in member 1 at 1800 UTC. Likewise, their minimum SLP is more similar to one another than to member 1, and their maximum winds are significantly weaker than those in member 1. Though the member-19 cyclone center has considerably less areal coverage of high PV than members 10 and 16, its maximum local intensity is similar to that of members 16 and 19. Thus, apparently only for the strongest members do organizational differences translate to differences in local (maximum) intensity at 1800 UTC. Yet the more organized cores of members 10 and 16 are beneficial to storm intensification later in the day, when their cyclones strengthen more rapidly than does that of member 19 (discussed in section 3.4.4).

To summarize, it was shown in this subsection that strength of a low-level PV anomaly at 1600 UTC 12 June strongly controls the ultimate strength of the cyclone. This anomaly results from the merger of two smaller anomalies, and its strength is modulated by the initial strength of the smaller anomalies and the amount of precipitation that falls during an eruption of convection around 1500 UTC. The next several subsections will analyze what specific initial factors both favor and inhibit convection in the *PTOT16Z* region.

3.4.2. Contributors to PTOT16Z: MUCAPE and deep moisture

Deep moisture in Chapter II was found to favor tropical cyclone intensification, and here it directly contributes to convection in the *PTOT16Z* region. To demonstrate this, Fig. 3.21g-i shows ensemble-mean mid-level (3-6 km average) moisture (hereafter in this chapter, *qmid*) and (*qmid*:*PTOT16Z*).The large meridional band of strong correlation

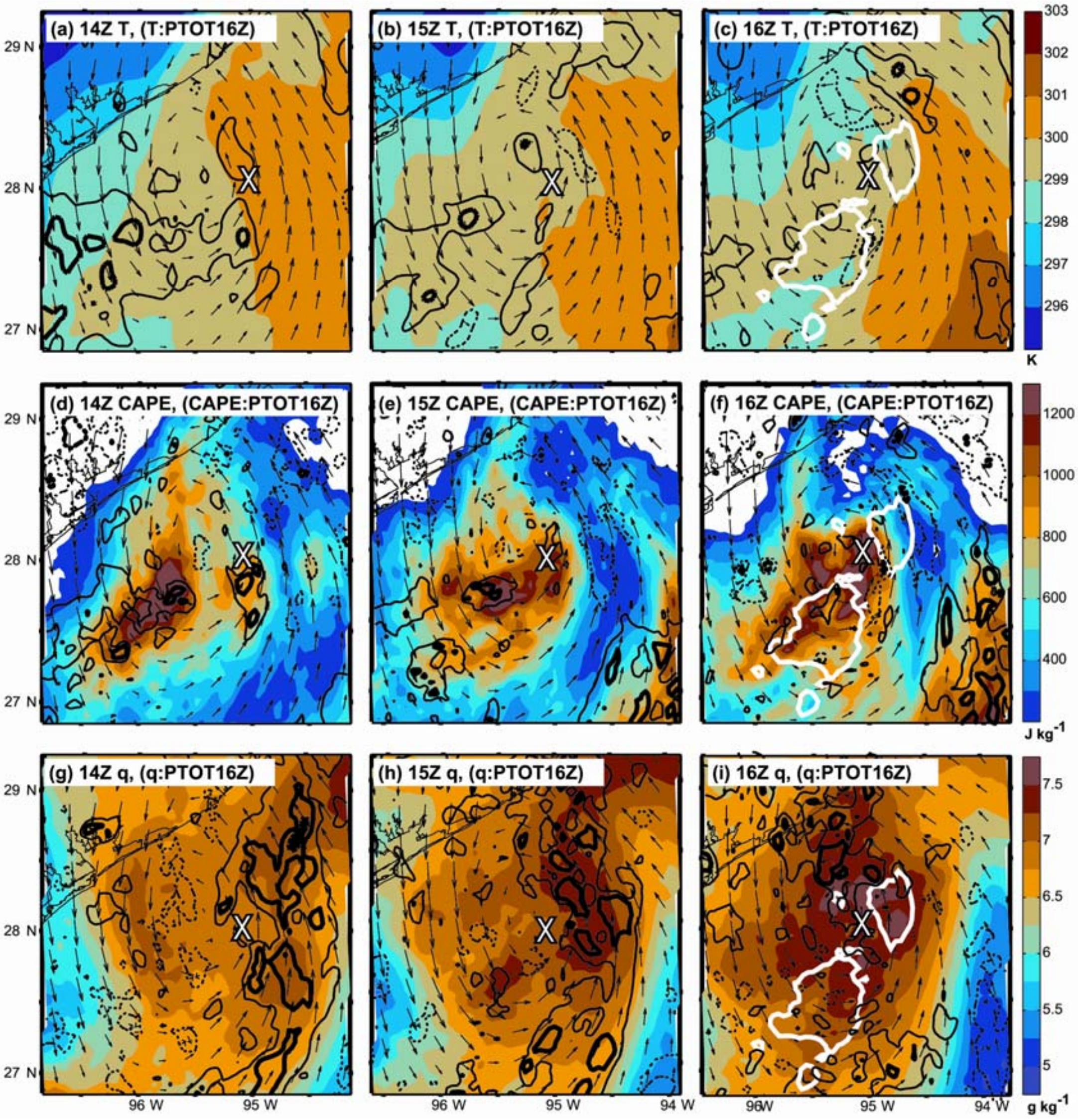

Figure 3.21. The relationship between *PTOT16Z* and antecedent/concurrent *Tsfc* (a-c), MUCAPE (d-f) and mid-level moisture (g-i) in a Lagrangian, storm centered coordinate system. Ensemble-mean *Tsfc*, MUCAPE, and mid-level mixing ratio (average from 3-6 km) are respectively color filled at intervals of 1 K, 200 J kg^{-1}, 0.5 g kg^{-1} at 1400 (first column), 1500 (second column), and 1600 UTC (third column) 12 June. Correlation between the variable in each panel and *PTOT16Z* is contoured as in Fig. 3.13. The *PTOT 16Z* region is contoured in white in panels (c), (f), and (i). Surface wind vectors are also shown, and the bold 'X' represents the position of the mean circulation center at 1600 UTC for reference.

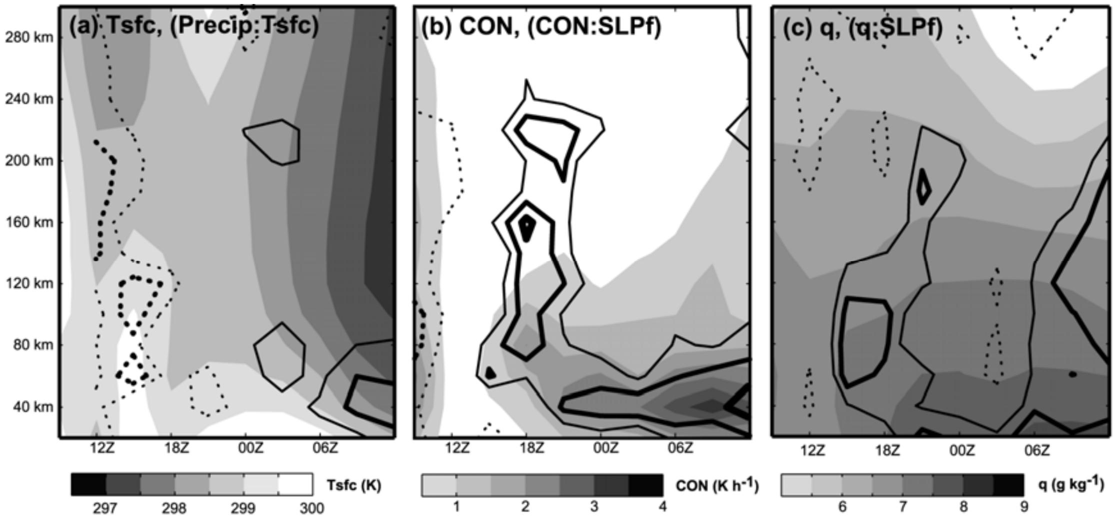

Figure 3.22. The Lagrangian evolution of ensemble-mean *Tsfc* (shaded every 0.5 K) and its correlation with preceding 3-h precipitation (a), ensemble-mean condensational heating (*CON*, shaded every 0.5 $\mathrm{K\,h^{-1}}$) averaged over 1-9 km and its correlation with *SLPf* (b) , and ensemble-mean mid-level (3-6-km average) moisture (shaded every 0.5 $\mathrm{g\,kg^{-1}}$) and its correlation with *SLPf* (c). All variables are displayed as a function of radius and time, and *CON*, *Tsf*c, and moisture are averaged in 20-km annuli before the correlation is computed. Correlation is contoured as in Fig. 3.13.

in Fig. 3.21g-h illustrates the direct causal role that mid-level moisture has in enhancing precipitation and thus genesis. This point is reinforced by Fig. 3.22, which shows the evolution of azimuthally averaged *qmid* and its correlation with *SLPf*. Both ensemble-mean *qmid* and (*qmid*:*SLPf*) generally increase with time in the immediate vicinity of the circulation center, which is a reflection of stronger storms having initially more moisture and subsequently more abundant convection near the center (Fig. 3.22b).

In addition to more deep moisture, *PTOT16Z* convection also benefits from higher surface temperature (hereafter in this chapter, *Tsfc*) and convective instability in its low-

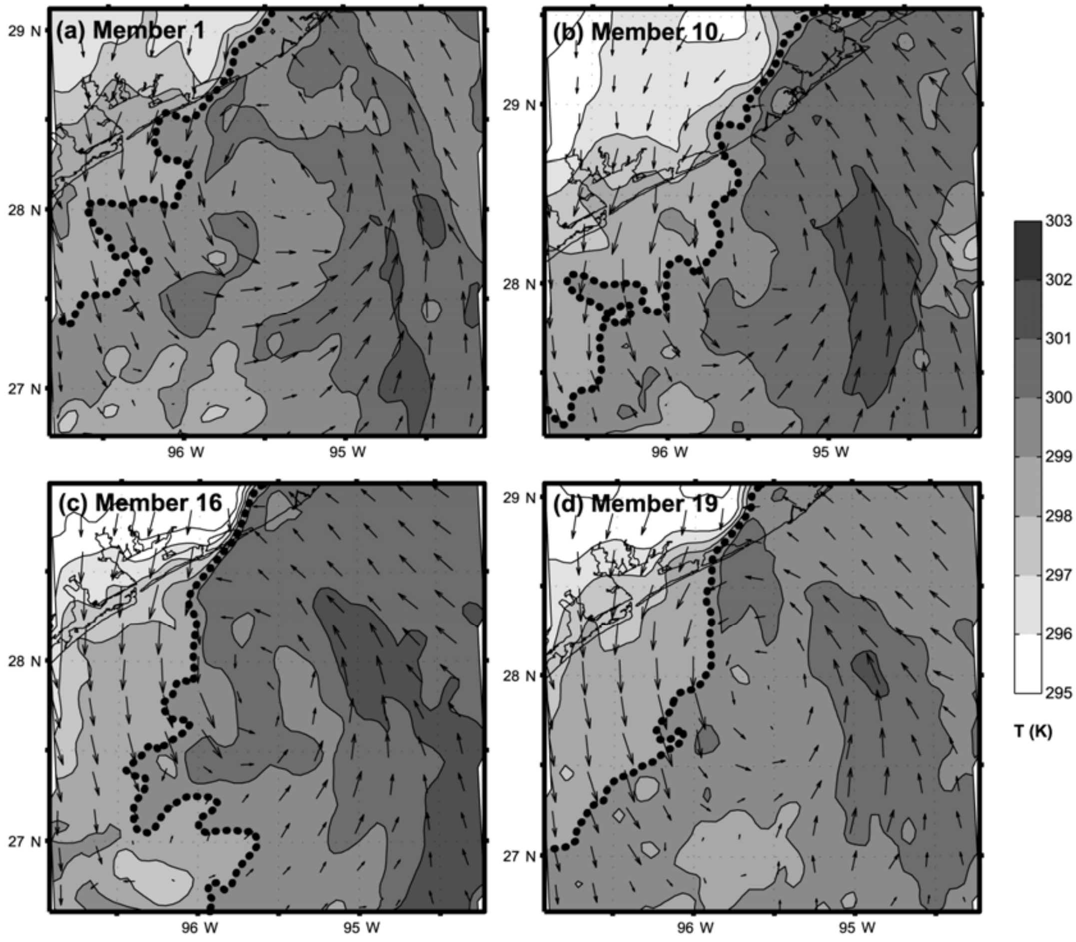

Figure 3.23. Surface temperature (shaded every 1 K) and wind vectors for members 1 (a), 10 (b), 16 (c), and 19 (d) at 1400 UTC 12 June. The approximate leading edge of cool, post-frontal air (i.e., the 299-K isotherm) is marked with a bold dashed line.

level inflow regions. To show this, ensemble-mean *Tsfc* (MUCAPE) is overlain with the correlation between *PTOT16Z* and *Tsfc* (MUCAPE) in Fig. 3.21a-f. Strongly positive (*Tsfc*:*PTOT16Z*) shows that higher surface temperatures upstream of the *PTOT16Z* regions are quite clearly beneficial to convection within the *PTOT16Z* boundary. In a specific example, member 19 has the coolest surface air immediately southwest of the circulation center (i.e., upstream of *PTOT16Z* convection) and generally less precipitation in the *PTOT16Z* region than the other simulations shown in Fig. 3.23. Meanwhile, member 1 generally has generally higher *Tsfc* in the same location than the other members shown, and it has very strong convection in the *PTOT16Z* region. Increased *Tsfc* is favorable because it results in higher MUCAPE, and (all else equal) an increase in MUCAPE leads to stronger convection. Indeed, precipitation that contributes to *PTOT16Z* falls generally downstream of distinct ensemble-mean MUCAPE maxima, and MUCAPE in these regions is significantly correlated with *PTOT16Z* (Fig. 3.21d-f). Both (*Tsfc*:*SLPf*) and (*MUCAPE:SLPf*) are respectively quite similar to (*Tsfc*:*PTOT16Z*) and (*MUCAPE*:*PTOT16Z*), which shows that the variance in *Tsfc* and MUCAPE that leads to precipitation differences also leads to similar differences in *SLPf*. In addition, there is evidence that the intensity of convection in the vicinity of anomaly A at 1100 UTC is also sensitive to surrounding surface temperature (not shown). This further demonstrates the importance of initial convective instability in generating Humberto and is a similar result to that seen in Chapter II.

Interestingly, Fig. 3.21 indicates that some precipitation areas might be more sensitive to variance in MUCAPE, while others are more sensitive to changes in mid-level moisture. For example, (*MUCAPE*:*PTOT16Z*) is strong in the inflow of the southwestern *PTOT16Z* region at 1400-1500 UTC, and it is weaker (yet still significant) in the inflow of the northeastern region. Meanwhile, *PTOT16Z* is strongly correlated to mid-level moisture upstream of the northeastern *PTOT16Z* region, but the variables are not at all correlated near the southwestern region (Fig. 3.21 g-h). This suggests that variance in inflow MUCAPE is the primary control for precipitation in the southwestern primary *PTOT16Z* region, and mid-level moisture more strongly controls precipitation variance in the northeastern region.

3.4.3. Frontal interaction: An inhibiting factor

Interaction with the front directly limits intensification in some ensemble members. Figure 3.24, which shows ensemble-mean surface mixing ratio (hereafter *qsfc*) and *Tsfc* along with (*qsfc*:*SLPf*) and (*Tsfc*:*SLPf*) at 0900 UTC and 1200 UTC 12 June, clearly demonstrates that the front negatively impacts *SLPf*. As in Fig. 3.3, enhanced *Tsfc* and *qsfc* gradients along the gulf coast clearly delineate the ensemble-mean position of the front. Strong (*qsfc*:*SLPf*) and (*Tsfc*:*SLPf*) to the north of the boundary indicate that a weaker front is more favorable for cyclogenesis, and similar correlation patterns at later times (not shown) indicate that the front continues to negatively impact cyclogenesis through the afternoon hours of 12 June. Figure 3.23 reveals the negative influence of the front very early in some ensemble members. Members 16 and 19, which have weaker cyclones than those in members 1 and 10, have cooler air behind the front and also tend to ingest post-frontal air sooner. This is demonstrated by differences in location of the 299 K isotherm in Fig. 3.23 and is partially a cause of the strong correlation between *PTOT16Z* and *Tsfc* in Fig. 3.21a-b.

Though the close proximity of the front could conceivably cause system location to be an important factor during the early stages of genesis, such does not appear to be the case before 1800 UTC. Pre-1800-UTC position is well stratified by strength in Fig. 3.6b, but very low position spread in the EnKF analyses indicates that position alone probably

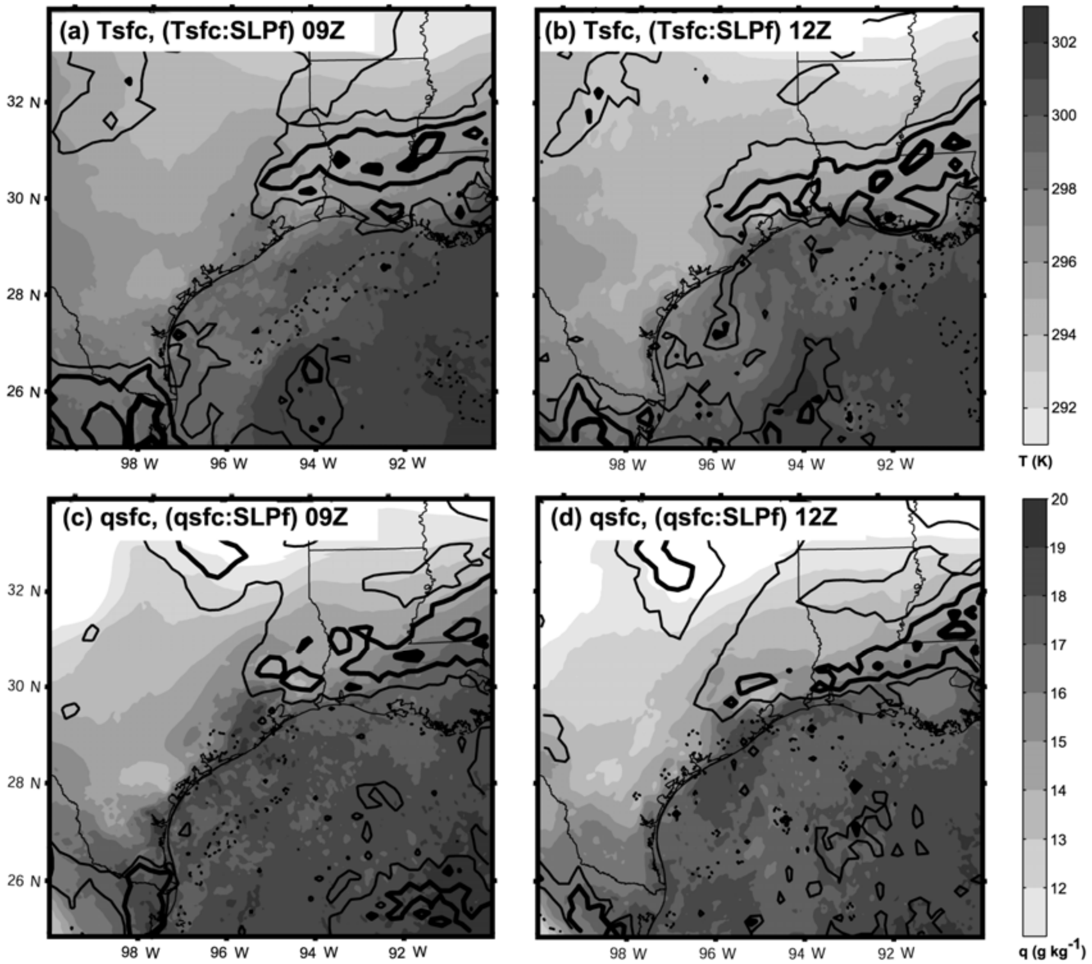

Figure 3.24. Ensemble-mean Eulerian surface temperature (a-b) and moisture (c-d) fields as well as the correlation between *SLPf* and the respective fields at 0900 (left column) and 1200 UTC (right column) 12 June. Temperature (moisture) is shaded every 1 K (1 g kg^{-1}), and correlation is contoured as in Fig. 3.13.

is not a controlling intensification factor at that time. There is only about 30-40 km of longitudinal separation between the western-most and eastern-most cyclones in Fig. 3.6b, which alone is insufficient distance to strongly govern the extent of front-cyclone interaction. For example, an inspection of the ensemble members in Fig. 3.23 reveals no clear indication that storms further west interact with the front more strongly by 1400

UTC. Member 10 is the western-most storm in Fig. 3.23, but it has surface temperatures warmer than those in members 16 and 19.

It appears that the main reason for strong stratification of position by strength in Fig. 3.6b (and correlation between pre-1800-UTC longitude and *SLPf*) lies in the relationship between frontal strength and the mean regional winds. For an undetermined reason (beyond the scope of this study), the strength of the front is very strongly anticorrelated with the mean zonal wind (u) below 6 km in the genesis area (i.e., members with stronger fronts also have a stronger easterly wind component, not shown). Since mean background winds are known to determine tropical cyclone track (zonal wind and storm longitude are strongly correlated here as well), the very early stratification of track by strength appears to be a byproduct of the relationship between the front and wind fields.

In summary, this subsection has shown that the presence of the front significantly inhibits development in ensemble members whose cyclones interact with it more strongly. Members with the weakest cyclones have the strongest fronts, and cooler, post-frontal air entrains into their circulations. Previous subsections show that convection leading to genesis is weaker when surface temperatures and instability are lower, so the effect of the front is to diminish this convection and ultimately PV production and genesis.

3.4.4. Post-1800 UTC evolution

To review, it was previously shown that variance in storm intensity by 1800 UTC explains a vast majority of *SLPf* variance. Stronger storms at 1800 UTC evolve from stronger low-level PV anomalies that initially appear around 1100 UTC in the ensemble mean. These anomalies are built by intense convection, which itself is fed by higher MUCAPE and mid-level moisture. Since a stronger surface front reduces surface temperature and convective instability, it also inhibits genesis. Finally, since *SLPf* is so strongly correlated with 1800-UTC cyclone strength, any processes acting after 1800 UTC generally only increase existing differences. This subsection investigates how spread increases after 1800 UTC.

Interaction with the surface front continues to be the most important mechanism governing cyclone intensity during the afternoon of 12 June. Unlike the period before 1800 UTC, however, storm track becomes an increasingly important factor. The reason for the change in relevance of storm position is related to the change from using EnKF analyses to using an ensemble forecast. At and before 1800 UTC, track spread is fairly low because EnKF analyses adjust the cyclone position in all members toward the observed track (Fig. 3.6). Therefore, differences in interaction with the front are not strongly a result of differences in storm position. However, spread increases substantially after 1800 UTC, when the background wind is free to advect cyclones without track adjustment by the filter. The 2100-UTC result of larger track spread is a much stronger track-dependent difference in cyclone-front interaction (Fig. 3.25). For example, not only do members 16 (Fig. 3.25c) and 19 (Fig. 3.25d) have drier air behind the front, but their cyclones are visibly further west and closer to the front than those in members 1 (Fig. 3.25a) and 10 (Fig. 3.25b). Recall that that the westerly wind component is strongly anticorrelated to front strength, so storms embedded in weaker

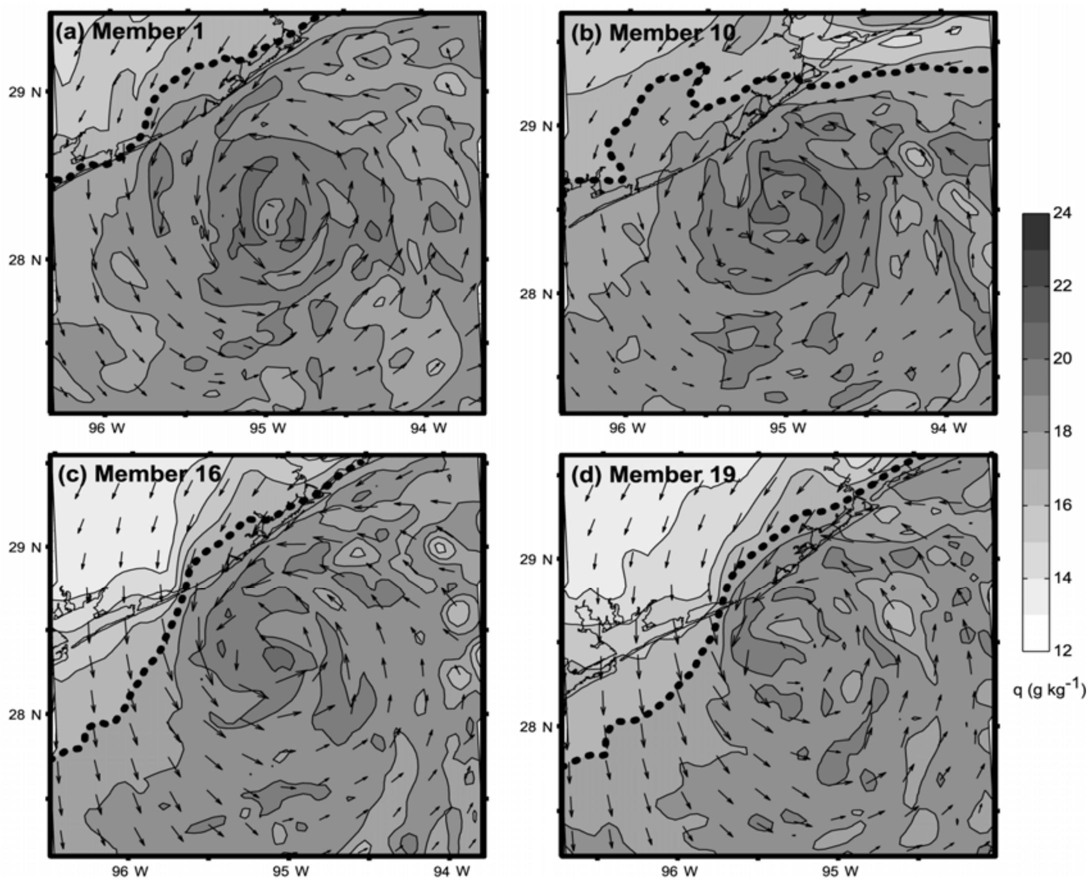

Figure 3.25. Surface mixing ratio (shaded every 1 g kg^{-1}) and wind vectors are shown for members 1 (a), 10 (b), 16 (c), and 19 (d) at 2100 UTC 12 June. The approximate leading edge of dry, post-frontal air is marked with a bold dashed line.

westerlies must fight a stronger front *in addition to* encountering the front sooner (e.g., in Fig. 3.6, storms with stronger westerlies move to the northeast, somewhat parallel to the front). Thus, the cyclones in members 16 and 19 face a serious uphill battle.

Other processes present before 1800 UTC persist through the afternoon as well. For example, the convection that begins at 1500 UTC in the southwestern *PTOT16Z* region lasts through the afternoon and into 13 June (see the boxed area in Fig. 3.26a for reference). This post-1800-UTC convection remains similar to the initial *PTOT16Z*

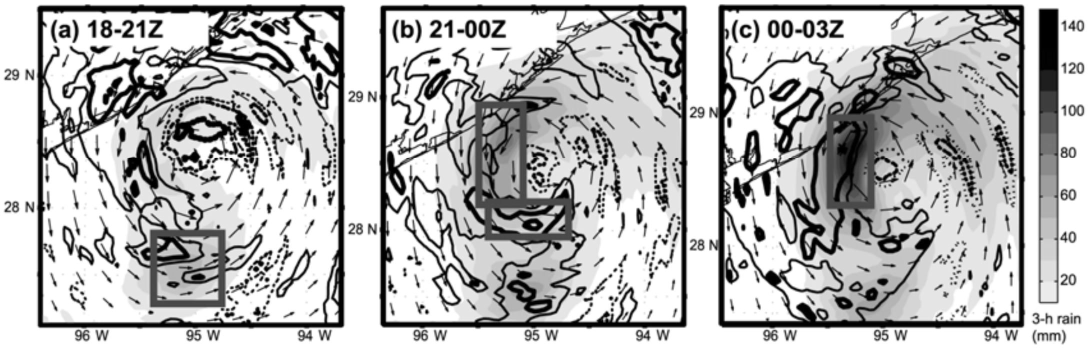

Figure 3.26. The relationship between *SLPf* and 3-h rainfall ending at 2100 (a), 0000 (b), and 0300 UTC (c). Ensemble-mean rainfall is shaded every 20 mm, and correlation is contoured as in Fig. 3.13. Analysis is completed in a Lagrangian coordinate system with the center of each panel at the ensemble mean center location.

convection in terms of its relationship with *SLPf* and surrounding thermodynamic fields. First, average precipitation inside the box in Fig. 3.26a is strongly correlated to *SLPf*, a likely result of continued low-level PV production in this region (e.g., Fig. 3.27a). Second, precipitation continues to be strongly correlated to its low-level inflow temperature (Fig. 3.28a), which indicates persistent importance of convective instability for genesis and intensification.

Another interesting result from Fig. 3.28 is that stronger convection produces stronger cold pools through the afternoon of 12 June. For example, surface temperatures downstream of the boxed area in Figs. 3.26a and 3.28a are strongly anticorrelated to mean precipitation within the boxed region. Yet, precipitation in the same region is strongly correlated with *SLPf*, which indicates that the negative effects of downdrafts do not outweigh the benefits of PV production. In fact, convection in this area continues producing low-level PV through at least 2100 UTC (see Figs. 3.19 and 3.27), and this

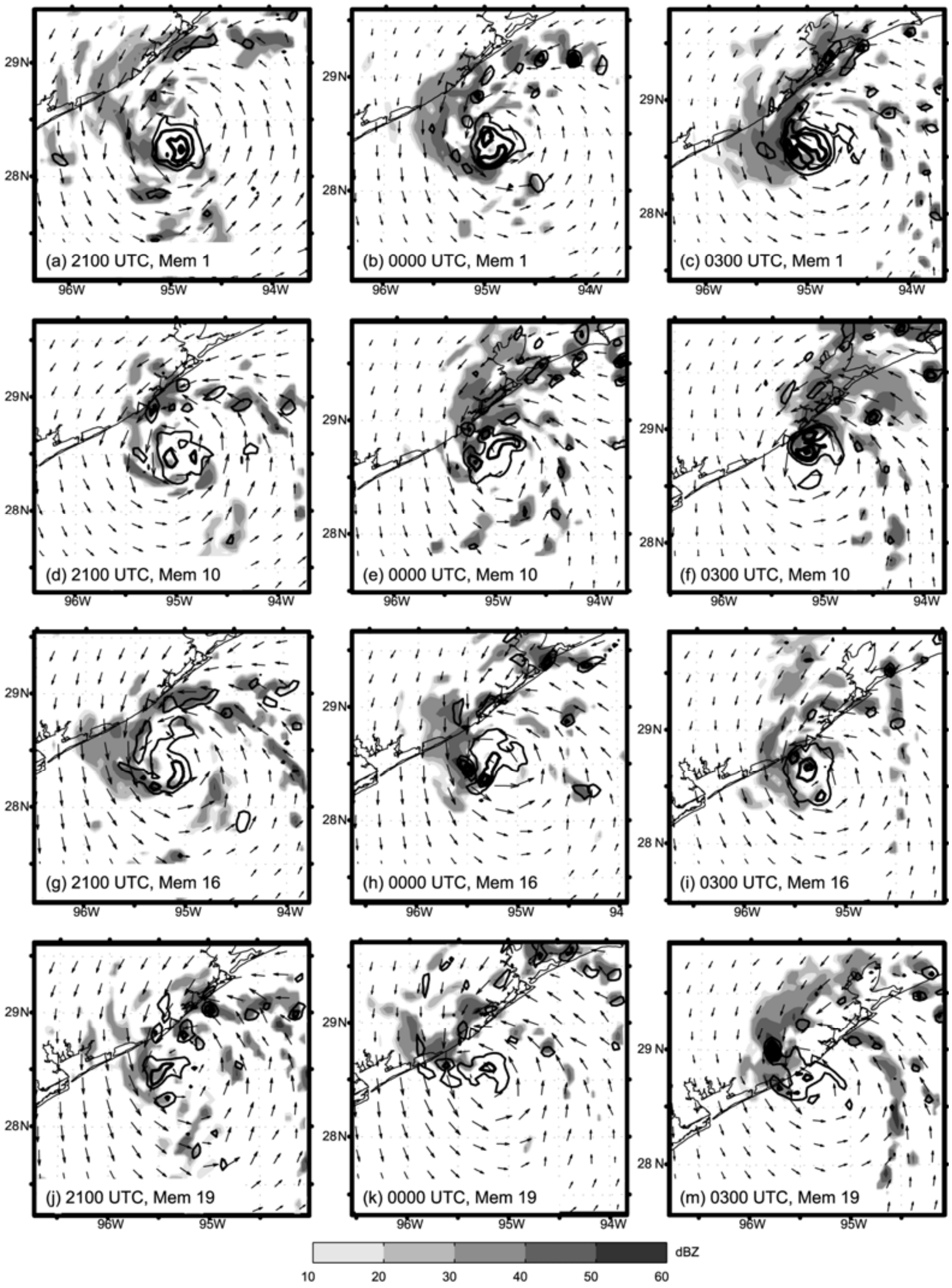

Figure 3.27. The evolution of PV (contoured at every 5 PVU with increasing thickness indicating increasing values) and simulated radar reflectivity (shaded every 10 dBZ) for members 1 (a-c), 10 (d-f), 16 (g-i), and 19 (j-m).

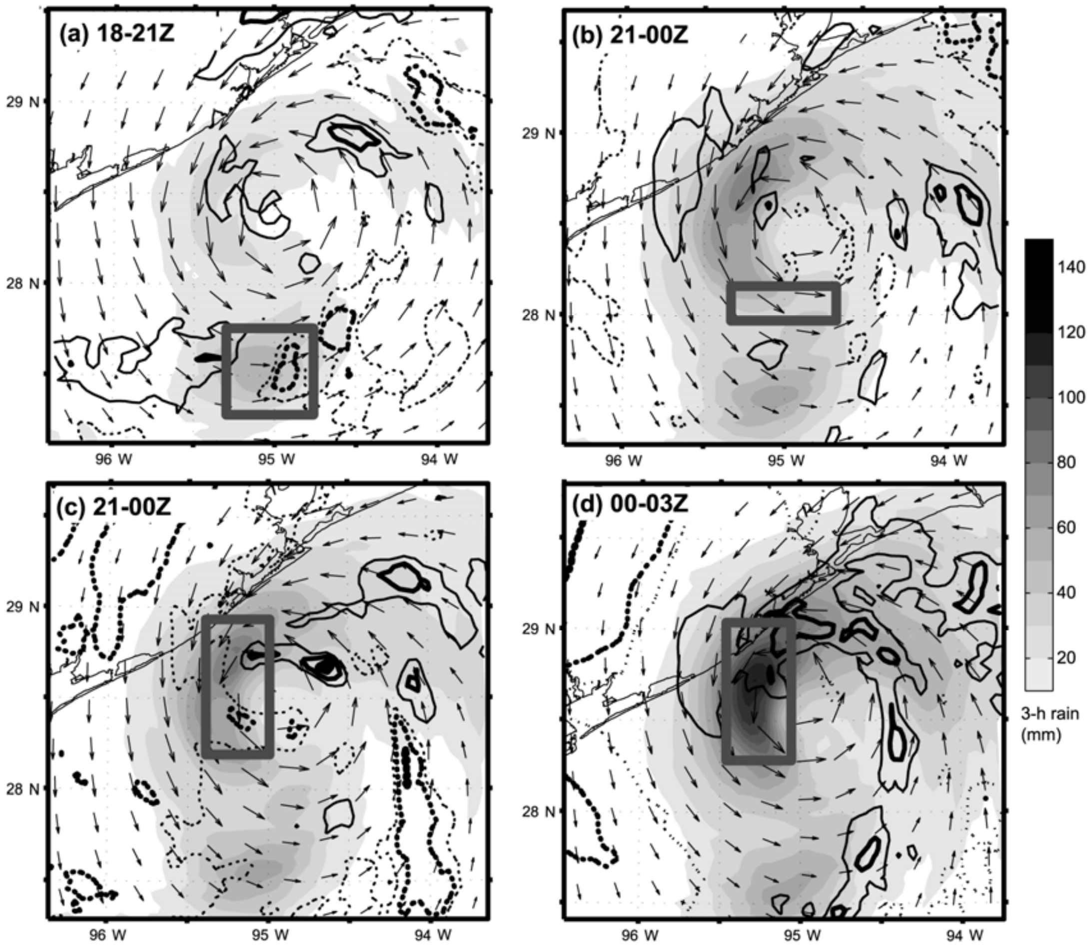

Figure 3.28. Ensemble-mean precipitation (shaded every 10 mm) from 1800 to 2100 UTC (a-b), 2100 to 0000 UTC (c), and 0000 to 0300 UTC (d) and correlation between *Tsfc* and area-average precipitation within the gray box. Correlation is contoured as in Fig. 3.13, and surface wind vectors are also shown. Analysis is completed in a Lagrangian coordinate system with the center of each panel at the ensemble mean center location.

PV eventually becomes ingested into the circulation center. In addition, other core precipitation that is strongly correlated with *SLPf* produces downstream cold pools through 0000 UTC 13 June (Figs. 3.26b-c, Fig. 3.28b-c). In a cyclone-mean sense, anticorrelation between azimuthally averaged precipitation totals and *Tsfc* is present through 2100 UTC (Fig. 3.22). Importantly, the *strength* of the cold pools decreases through the day (not shown).The above results are especially interesting in light of the fact that the entire ensemble intensifies at the same time that convection produces cold downdrafts (e.g., see Fig. 3.2). Only after 0000 UTC does anticorrelation between *Tsfc* and core convection cease to be statistically significant immediately surrounding the cyclone center (Fig. 3.26c). By this time, pressure has dropped by greater than 5 hPa, and wind has increased beyond tropical storm strength in most ensemble members. Thus, cessation of cool downdrafts is not necessary for intensification. Rather, as intensification proceeds, downdrafts either weaken, or some other process mitigates their effects.

In fact, it appears that enhanced oceanic heat flux (hereafter in this chapter, FLUX) both directly and indirectly increases *Tsfc* and maintains storm intensity in face of downdraft activity. First, strongly negative (*FLUX*:*Tsfc*) near the mean center in Fig. 3.29c shows that *Tsfc* variance directly modulates FLUX variance until about 0300 UTC 13 June. Thus, any decrease in *Tsfc* due to downdrafts is likely associated with an increase in FLUX, which probably contributes to the diminishing statistical relationship between precipitation and cold pools in Fig. 3.28d. Indeed, ensemble mean *Tsfc* inside 40 km rises from 1800 UTC 12 June until 0000 UTC 13 June (Fig. 3.22a) despite the fact that mean, downdraft-producing convection near the center increases markedly during the same time period (Fig. 3.22b). (*FLUX*:*SLPf*) in Fig. 3.29a indicates that stronger storms at 0600 UTC 13 June have had generally higher FLUX on 12 June.

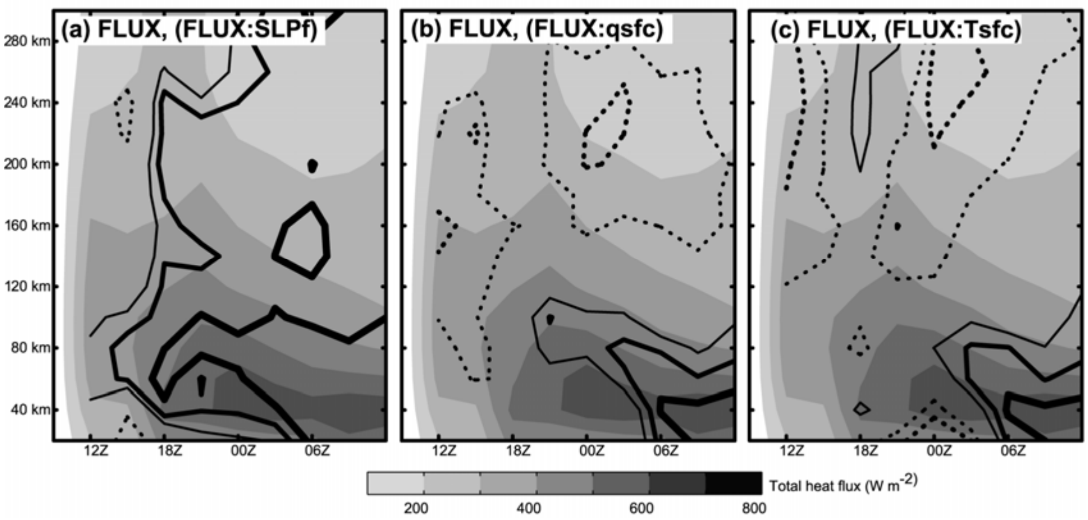

Figure 3.29. Ensemble-mean total heat fluxes (FLUX, shaded every 100 W m^{-2}) overlain with (*FLUX*:*SLPf*) (a), (*FLUX*:*qsfc*) (b) and (*FLUX*:*Tsfc*) (c) as a function of radius and time. All variables are averaged in 20-km annuli before computing the correlation, and correlation is contoured as in Fig. 3.13.

Thus, the high FLUX in stronger storms more efficiently combats their more widespread cold pools. Second, increased FLUX through the afternoon of 12 June should also indirectly contribute to warming *Tsfc* by leading to more convection, which itself moistens the mid-troposphere (note that mid-level moisture indeed rises through the day in Fig. 3.22c). With a more humid mid troposphere, the temperature of downdrafts should increase and downdrafts themselves should weaken. .

The rapid increase in ensemble-mean FLUX in Fig. 3.29 and diminished relationship between stronger convection and cold pools essentially signals the onset of WISHE and evolution to a mature tropical cyclone. Tropical cyclone dynamics are also strongly implied by 0600 UTC (*FLUX*:*Tsfc*) and (*FLUX*:*qsfc*). The rapid strengthening of these correlation fields indicates that storms with stronger surface fluxes begin to have warm, moist surface air over a large area surrounding their centers. With enhanced FLUX easily overcoming the effects of downdrafts and the weakening of downdrafts, *Tsfc* and *qsfc* increase and provide a more favorable environment for strong convection. Thus, stronger storms are able to strengthen more quickly because they have stronger heat fluxes; this is the essence of the WISHE mechanism.

Both the continuation of processes ongoing before 1800 UTC and strength-dependent oceanic heat fluxes lead to further organization and strength differences in the ensemble. From 2100 UTC 12 June to 0300 UTC 13 June, the 2-km PV core is significantly stronger in member 1 (Fig. 3.27a-c) than in members 10, 16, and 19 (Fig. 3.27 d,g,j). Though members 10 and 19 are initially similar in terms of 2-km PV and surface intensity, they also begin to diverge by 0300 UTC. Member 19 lags farthest behind with less high PV at 2 km, fairly high SLP, and low winds.

Finally, differences in landfall time after 0600 UTC have an effect on the ensemble that is dynamically similar to but increasingly more pronounced than the front. Because the front lies parallel to the coast, variance in frontal interaction must necessarily be associated with differences in the time that a storm is over water. While entrainment of post-frontal air certainly lowers instability and hinders convection, landfall is a much more severe instantaneous effect that completely shuts off the *source* of instability. The above correlation analysis was constructed in a way that minimizes the effects of landfall on the diagnosed dynamics (by using *SLPf* at 0600 UTC, before most members have made landfall in Fig. 3.6b) so that the above *other* factors could be investigated, but the landfall of storms thereafter leads to increasing spread until storms in most members have made landfall (Fig. 3.3c-d).

3.4.5. Other processes relevant to intensification

Deep-layer shear is also known to inhibit genesis, so its relation to intensification in the ensembles is also briefly shown here. The positive early correlation between *SLPf* and deep-layer shear in Fig. 3.5 indicates that either the initial shear is beneficial for genesis or the pre-1800-UTC analysis increments do not correctly capture the relationship between upper level winds, convection, and storm intensity. Since ensemble-mean shear is quite low before 1800 UTC, it is possible that shear helps to organize convection during this time frame (e.g., as in Molinari et al. 2004). After 1800 UTC, however, shear intensifies and clearly becomes an inhibitor to intensification. The magnitude-dependent effects of shear are similar to the results of Chapter II.

The tendency for (*qmid*:*SLPf*) to be highly variable beyond a radius of about 60 km is also similar to the results of Chapter II. Initial mid-level moisture there was well-correlated with final intensity over a large area. However, at later times, only mid-level moisture very near the center was correlated with intensity. It was found that the varying correlation between large-scale, mid-level moisture and final intensity was due to the establishment of a secondary circulation; subsidence outside of the immediate vicinity of the cyclone is stronger with increasing cyclone strength. In the case of Humberto, it was shown that strong positive (*qmid*:*SLPf*) around 1500 UTC is the result of mid-level moisture favoring more precipitation. Meanwhile, the substantial drop in correlation later in the day may very well be due to subsidence outside of the peak condensational heating annulus, as in Chapter II. Interestingly, (*qmid*:*SLPf*) changes sign again around 0600 UTC 13 June. This change might be due to convection forced by the eventual interaction of stronger circulations with the front (not shown).

3.5. Discussion

It has been shown that an ensemble initialized with EnKF perturbations can accurately capture the genesis and intensification of Hurricane Humberto, a storm deemed highly unpredictable in the operational environment. Not only does the EnKF-initialized ensemble produce storms that span the observed strength of the cyclone, but some ensemble members produce cyclones with reasonable structure and mesoscale interaction with a nearby front. Even the poorest performing ensemble members perform better than operational models, which completely failed in this event. Yet, the EnKF-initialized ensemble produces huge spread, which further highlights the lack of predictability of this event. The large ensemble spread and good ensemble performance make this an ideal case to test the results of Chapter II and further investigate the source of error in the forecast of an actual tropical cyclone.

Perhaps the most significant result of this chapter is that the results of Chapter II have generally been confirmed. Though the ensemble initialization method, the genesis environment, and the storm itself are very different here than in Chapter II, MUCAPE and mid-level moisture have once again been found very important at determining how quickly cyclones strengthen in various ensemble members. Thus, it appears that the main sources of uncertainty (spread) in the ensemble forecast here are the instability and mid-level moisture fields. Spread in the instability analysis and forecast appears to be a result of differing positions of the front and the extent to which the front and cyclone interact. Meanwhile, mid-level moisture differences among ensemble members might stem from the lack of in-situ moisture observations over the Gulf of Mexico.

With respect to the above result, one significant difference between the current case and Chapter II is in regard to the areal extent of positive correlation. In Chapter II the correlation between *SLPf* and both MUCAPE and mid-level moisture extended to the synoptic scale (not shown, but implied to some extent by the averaging area of the variables), but in the current chapter the correlation is limited to inflow regions of convective areas. This difference is very likely due to the difference in ensemble initialization. For instance, with only large-scale initial perturbations and no convection in the analysis, the cold-start technique in the Chapter II ensembles produces initial spread only at large scales. Thus the correlation length scale is very large, and convective intensity is well related to CAPE and moisture in the entire surrounding region. Meanwhile, the presence of cold pools and mesoscale variations associated with the hot-start technique in the current case leads to a shorter correlation length scale in the analyses. Specifically, CAPE and mid-level moisture are correlated to precipitation only in the convective inflow regions.

Improvements in analyses and model physics could likely reduce some of the above uncertainty. For example, more numerous in situ observations can also further refine the exact position of features such as fronts and better estimate the state of the atmosphere in regions that are currently only remotely sensed. A practical result of these improvements would be less ensemble spread later in the forecast period and more accurate specification of the true intensification.

Yet, the behavior of the various ensemble members here indicates that a certain (fairly large) degree of uncertainty might always be expected in some situations. For instance, the RMS spread of lower tropospheric variables in the 1800-UTC EnKF analysis is comparable to typical analysis error (not shown). Even if significant improvements were made to the analysis, it is likely that large (albeit less) strength spread would remain simply because of small differences in the trajectory of the cyclone and the time it would take for the cyclone to interact with both the front and land. In order to understand how minute differences in initial conditions can impact the forecast of a tropical cyclone, the next chapter in this dissertation will return to the 2004 gulf low and examine the sensitivity to error far smaller than can be detected by any analysis or observation system.

CHAPTER IV

AN ASSESSMENT OF THE LIMIT OF INTRINSIC PREDICTABILITY OF THE GULF LOW[*]

4.1. Introduction

With probabilistic dynamic analyses completed and similar results obtained for a case independent of the gulf low (i.e., Chapter III), it is more certain that the results from the gulf low case (i.e., Chapter II) represent realistic processes and are relevant to more than just an isolated event. This chapter therefore now turns back to select ensemble members from Chapter II to investigate the effects of very small changes in initial conditions on tropical cyclone formation. The purpose of this chapter is to better understand the inherent limit of tropical cyclone predictability arising from initial errors with amplitudes far smaller than any observation and analysis system.

In particular, this chapter analyzes the effects of initial condition differences on both larger scale structure and smaller scale variations during tropical cyclone formation. Although the results of Chapter II imply that large-scale thermodynamics play an important role in tropical cyclone formation, the mesoscale area averages utilized in Chapter II preclude insight into the importance of smaller scale features such as VHTs. This paper investigates how *both* larger mesoscale variations and VHT generation/evolution are impacted by initial condition error.

---

[*] Reprinted with permission from “Effects of Moist Convection on Hurricane Predictability” by F. Zhang and J. A. Sippel. *J. Atmos. Sci.*, in press.

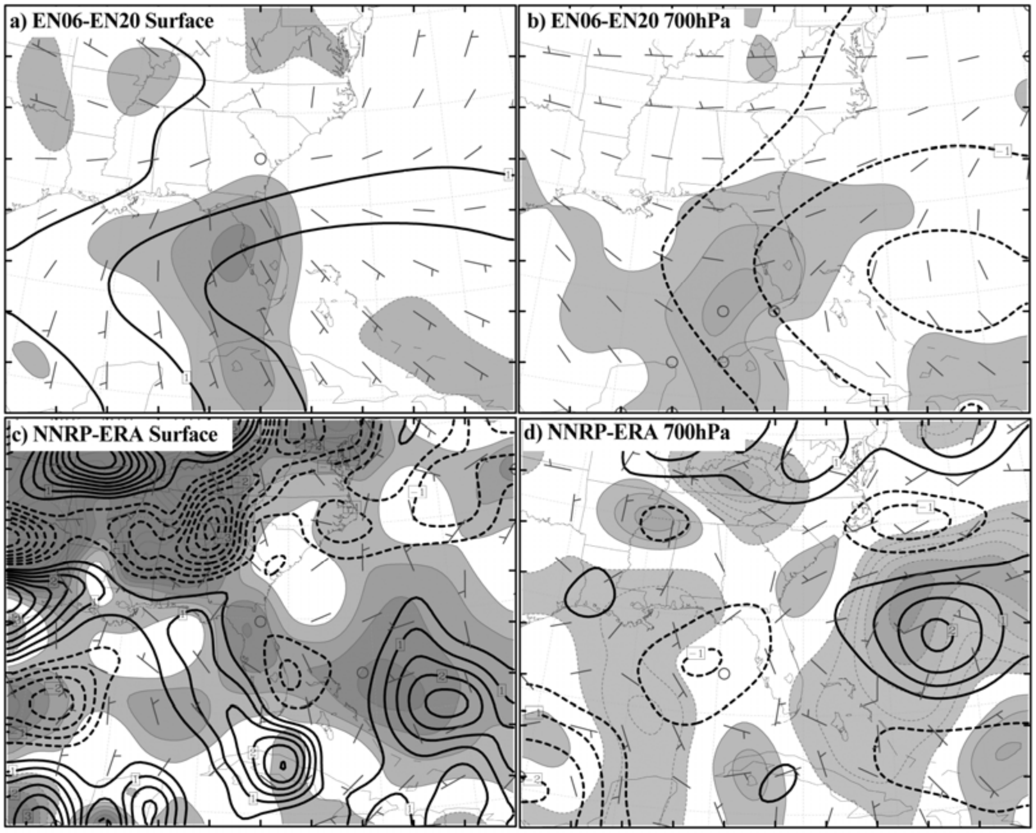

Figure 4.1. Difference between surface and 850-hPa temperature (thick; every 0.5K), mixing ratio (thick lined and shaded; every 0.5 $g\,kg^{-1}$) and horizontal wind vectors (full barb 5 represents $m\,s^{-1}$) for (a-b) ensemble members 6 and 20 and (c-d) the NCEP/NCAR and ECMWF global reanalyses interpolated to the MM5 grids at 00 UTC 30 July.

4.2. Methodology

In this chapter initial-condition sensitivity experiments are used to explore the dynamics that leads to drastic difference in storm development between members 6 and 20 in the CTRL ensemble of Chapter II. Recall from Chapter II that member 6 develops a strong tropical storm and member 20 remains very weak after 36 hours. These strong final differences come in spite of initial RM-DTE between the two members being less than typical analysis error (e.g., Fig. 2.2). Furthermore, Fig. 4.1 shows that the initial surface and 700-hPa wind, temperature and mixing-ratio differences the two members are generally equal to or smaller in magnitude than differences between the NNRP and ERA reanalyses. Thus, the discrepancies between these two extreme members are comparable to realistic analysis uncertainties in the large-scale environment. Additional analysis uncertainties related to the mesoscale and microscale structure of the tropical disturbances, along with errors in the forecast model, may lead to even stronger forecast divergence and thus further limit hurricane predictability. However, the current study focuses only on the effect of large-scale environment initial uncertainty on the predictability of tropical cyclones.

Nomenclature for the experiments in this chapter is as follows. For simplicity, the non-developed member 20 is defined to have an initial perturbation of zero (hereafter member 20 will be “QRT0”). The difference between members 6 and 20 for all prognostic variables is defined as one unit state vector (hereafter referred to as the “difference vector”). Thus the perturbation magnitude for member 6 is 1 unit, or 4 quarters (hereafter member 6 will be “QRT4”). Also performed is a series of sensitivity experiments, each with an initial perturbation added to QRT0 that varies in amplitude from -0.5 to 1.5 in units of the difference vector. For example, an initial perturbation value of 1.5 (which is experiment QRT6) corresponds to adding 1.5 times the initial difference between QRT0 and QRT4 to the reference experiment QRT0, and a perturbation value of -0.5 corresponds to subtracting the half the difference from QRT0 (which is experiment QRTM2). Values of 0.5 and 0.75 correspond to experiments QRT2

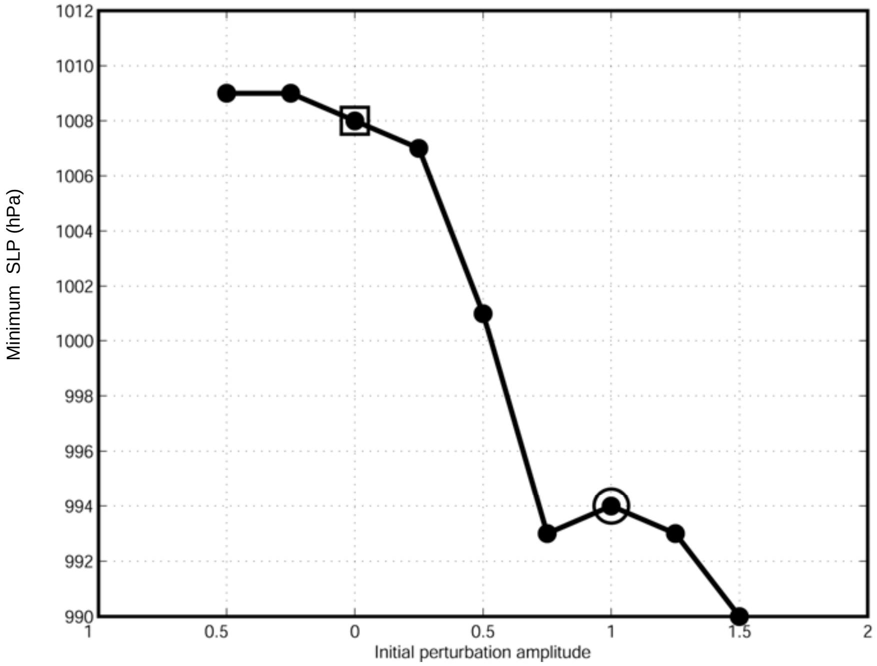

Figure 4.2. Sensitivity of the 36-h minimum SLP to initial-perturbation amplitude. The x-axis depicts the initial perturbation magnitude scaled by the difference vector, which is the initial difference for all prognostic variables between QRT4 (i.e., member 6) with a circle and QRT0 (i.e., member 20) with a square.

and QRT3, which respectively add perturbations to QRT0 with amplitudes of 2 and 3 quarters that of the difference vector. Experiments QRTM1 and QRT5 respectively correspond to perturbations of -0.25 and 1.25.

As in Chapter II, the results here carry the caveat of using a cold-start technique to initialize the ensemble. The probable result of having no convection in the initial analysis is that the model produces very strong convection during the spin-up period. Despite this limitation, the results of Chapter III suggest that the basic principles governing the Chapter II results are indeed physically relevant to the atmosphere.

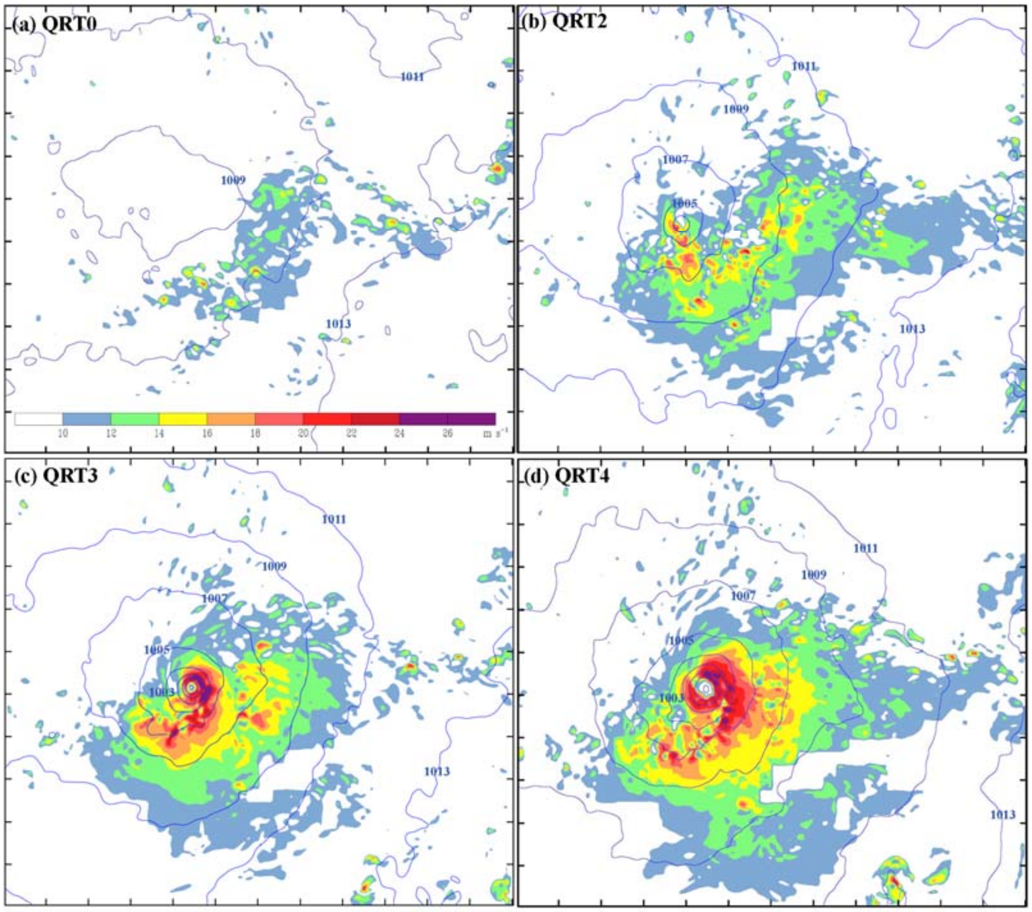

Figure 4.3. Comparison of the 36-h surface wind speed (only >10 m s^{-1}, color filled every 2 m s^{-1}) and sea-level pressure forecasts of the Gulf low (a) QRT0, (b) QRT2, (c) QRT3 and (d) QRT4. The sea-level pressure (contoured every 2 hPa) is smoothed 9 times with a 5-point smoother. Tick marks denote a horizontal distance of 100 km.

4.3. General characteristics of experiments

Figures 4.2 and 4.3 demonstrate that the above simulations can be clearly grouped as “developing” and “non-developing”. Figure 4.2 shows sensitivity of the 36-h minimum SLP change to adding different perturbations. The 36-h minimum SLP has a strongly nonlinear distribution with a fairly strong first-order discontinuity around 0.75. The transition zone in Fig. 4.2 is very narrow, and a change as small as one quarter of the difference vector (i.e., from QRT2 to QRT3) distinguishes whether or not a well-organized tropical cyclone will form. Figure 4.3, which shows the 36-h surface wind and SLP from QRT0, QRT2, QRT3, and QRT4, further demonstrates the narrow transition zone. QRT3 and QRT4 are both near category 1 hurricane strength, and each has an impressive primary rain band and a nearly closed eyewall (not shown). In the meantime, there is virtually no tropical development in QRT0, while QRT2 forms a generally unorganized tropical cyclone.

The simulations with developing systems can also be distinguished in terms of organization as early as 6 h, a result that will be discussed in much more detail in sections 4 and 5. For now, it is sufficient to say that simulations QRT2 through QRT6 develop both a larger scale circulation and strong, 20-50-km vortices, which will be referred to as VHTs[5]. Examples of VHTs in QRT5 and QRT6 at 9 h are shown in Fig. 4.4, where 985-hPa θ_e, wind vectors, and vertical vorticity are shown along with 500-hPa vertical velocity. The towers of strong vorticity are always initially associated with updrafts (as in anomalies A1, B1, C1, B2, and C2 in Fig. 4.4), though sometimes the vorticity remains long after the updraft dies (as in A2; such features which will be referred to as a remnant vortices since a VHT must be associated with an updraft). Both QRT0 and QRT1 also initially develop weaker larger scale circulations and a few small-

---

[5] The vortices here do not seem to precisely match the characteristics of any features heretofore discussed in literature. Their association with deep convective updrafts suggest a formation mechanism similar to that of VHTs (Hendricks et al. 2004; Montgomery et al. 2006), though they appear to be somewhat larger than the 10-30-km scale suggested in Montgomery et al. (2006). Since the vorticity features here are analyzed only on the 10-km grid due to data processing and storage constraints, aliasing error might make such features appear to be larger than they actually are. Considering this possibility, and since this is a numerical study and the vortices here generally resemble VHTs, the ‘VHT’ term is used.

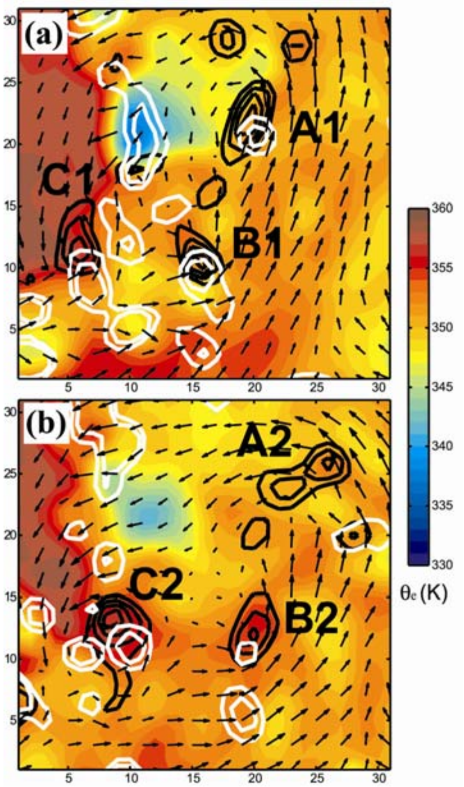

Figure 4.4. Surface (985-hPa) wind vectors (scaled differently in each panel), absolute vorticity (black contours every 2.5×10^{-4} s^{-1} beginning at 5×10^{-4} s^{-1}), θ_e (color filled every 1 K), and 500-hPa vertical velocity (solid white contours at 0.5 and 1.0 m s^{-1}) at 9 h in simulations (a) QRT5 and (b) QRT6. The axes are labeled every 5 grid points (50 km) on the 10-km grid, and several VHTs or remnant vortices are labeled in bold.

scale vorticity anomalies near their limited convective cells. However, their small-scale features are weak, isolated, ephemeral, and they hardly resemble VHTs. Meanwhile, QRTM1 and QRTM2 take 12-18 h to even develop a very weak larger scale circulation.

Finally, in light of the small initial condition differences between QRT0 and QRT4, the stark differences between QRT0 and QRT4 cyclone development is somewhat alarming. In particular, the initial root-mean square difference between QRT0 and QRT4 is smaller than NCEP-assumed observational errors and differences between global analyses of lead operational centers for all variables at nearly every vertical level (Figs. 2.3 and 4.1). The large difference in outcome due small initial uncertainty in the large-scale environment further highlights the potential for extreme difficulty in deterministic prediction of hurricane formation and intensity.

4.4. Effects of moist convection: Storm scale

In the previous section, it was demonstrated that a sharp transition occurs around an initial perturbation of 0.5. The following section examines the detailed the role of moist convection in the extreme sensitivity of model solutions to very small initial-condition differences between the simulations shown in Fig. 4.2 (though the main focus will be on those from Fig. 4.3). Due to time and storage issues related to post-processing large quantities of data from the 3.3-km grid, all analysis will take place on the 10-km grid.

The choice of initial variables/parameters to examine is motivated by the findings of Chapter II. In particular, Fig. 4.5 shows the time evolution of responses to the different initial conditions in all simulations in Fig. 4.2 averaged over a $300\text{ km} \times 300\text{ km}$ box area (hereafter referred to as a “storm-scale” average)[6] except for maximum surface vorticity (panel f) and wind speed (panel d). Chapter II found that initial MUCAPE was well correlated to cyclone intensification, but this chapter instead examines surface θ_e.

---

[6] Before convection begins, the box center is near the 700-hPa circulation center in all simulations between from QRT0 to QRT6, which is where convective initiation occurs. Thereafter, the box center follows the surface to 850-hPa vorticity center in those same simulations. Because convection is almost completely inactive in simulations weaker than QRT0, a surface low is very slow to form. Therefore, the box center in those simulations follows that of QRT0 for the entire simulation. Only small changes in storm-scale averages occur if the box center is defined by other metrics.

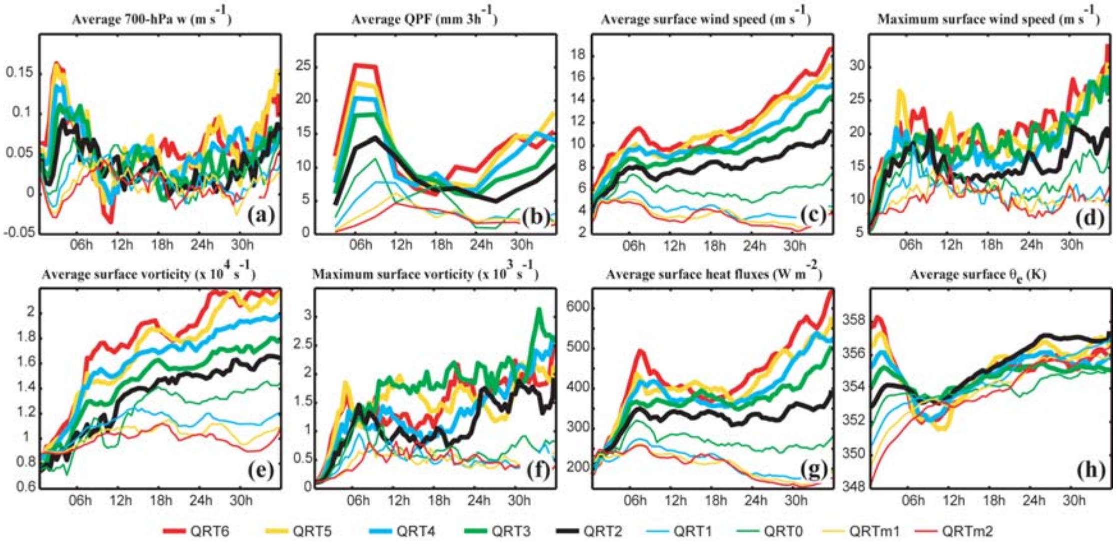

Figure 4.5. Time evolution of storm-scale averaged (a) 700-hPa vertical velocity ($\mathrm{m\,s^{-1}}$), (b) 3-h accumulated precipitation (mm), (c) surface wind speed ($\mathrm{m\,s^{-1}}$), (e) surface vorticity ($\times 10^{-4}\ \mathrm{s^{-1}}$), (g) surface heat fluxes ($\mathrm{W\,m^{-2}}$), and (h) surface θ_e (K) as well as (d) maximum surface wind ($\mathrm{m\,s^{-1}}$) and (f) vorticity ($\times 10^{-3}\ \mathrm{s^{-1}}$) in all simulations shown in Fig. 4.2.

Initial MUCAPE and θ_e were strongly correlated at early times in Chapter II, so differences in θ_e represent similar differences in MUCAPE. In addition, surface θ_e has the added benefit of demonstrating cold pool strength and the extent of planetary boundary layer (PBL) recovery after cold pool formation. Meanwhile, storm-scale 700-hPa vertical velocity (*w*) and 3-h precipitation totals demonstrate differences in convection, and average wind speed and vorticity show differences in intensity on the system scale. Maximum surface wind speed and vorticity are metrics of system strength on local scales.

In a manner consistent with Chapter II, storm intensity appears to vary with initial θ_e differences and the amount of initial precipitation that falls. Simulations with higher initial instability in Fig. 4.5h have stronger mean upward velocity at 700 hPa through 6 h (Fig. 4.5a), and they generate more precipitation during the first 9 h (Fig. 4.5b). Likewise, these same simulations have generally stronger storm-scale surface wind speeds and vorticity by 6-12 h (Fig. 4.5c-f). The apparent inability to develop a cyclone without an initial round of convection is quite evident by the similarly low storm-scale winds and vorticity in QRT0, QRTM1, and QRTM2.

4.4.1. Convective instability and convection

While the initial differences in most variables in Fig. 4.5 are quite small compared to their later differences, differences in surface θ_e (due to both temperature and moisture differences) are considerably larger at the initial time than they are at later times. For example, initial surface θ_e in QRT4 (i.e., member 6) is a little more than 4.5 K higher than in QRT0 (i.e., member 20), but it decreases to less than 2 K at later times. The initial difference in surface θ_e between QRT0 and QRT4 (Fig. 4.6a), though seemingly big, is comparable to the difference between NCEP and ECMWF global reanalyses over this region (Fig. 4.6b). This difference therefore grossly represents the realistic large-scale initial-condition uncertainties in tropical cyclone prediction. The following discussion will show that the underlying cause for diminishing θ_e variation is that convection tends to equilibrate convective instability among the simulations. Meanwhile, the same differences in convection tend to increase variation with other variables and metrics of strength.

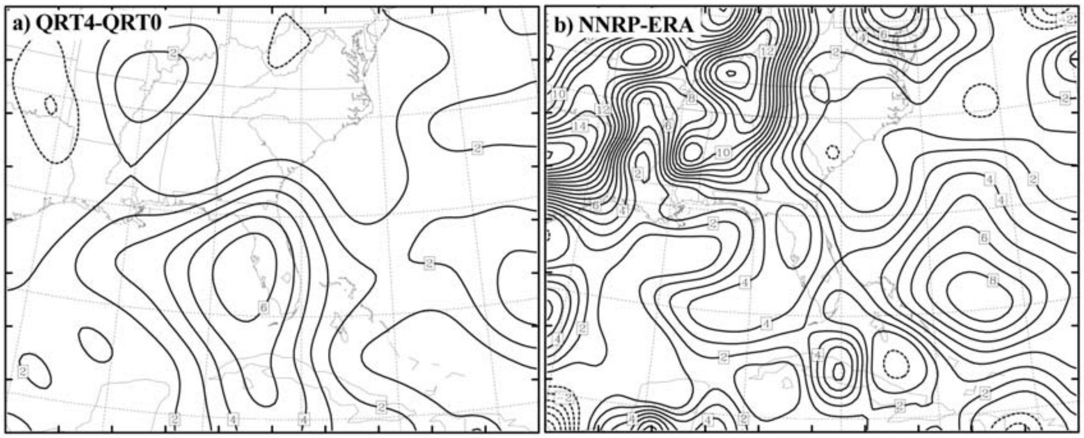

Figure 4.6. The initial difference in surface θ_e (every 0.5K; negative dotted) between (a) QRT0 and QRT4, and (b) between the NCEP/NCAR (NNRP) and ECMWF (ERA) reanalyses interpolated to the MM5 grids.

If, as found in Chapter II, higher initial surface instability results in more precipitation, then it must do so as a result of more intense and/or widespread updrafts. Although mean 700-hPa *w* is indeed stronger in simulations with higher initial instability, general updraft (and downdraft) characteristics are not clear from such a mean. In order to better understand early updrafts, the analysis in Fig. 4.7a-b is undertaken by first calculating vertical mass flux per unit area at every point and every σ-level in the storm-scale region every 30 m from 0-6 h, 6-9 h, and from 0-9 h. The first time period encompasses the strongest convection in all simulations and ends generally before strong cold pools form, the second period begins about when significant cold pools begin to form, and the sum of the two periods spans the duration of the heaviest precipitation for all simulations in Fig. 4.5. Mass flux per unit area is calculated by multiplying vertical velocity by density at each grid point. Grid point values are sorted into 0.5 m s^{-1} vertical

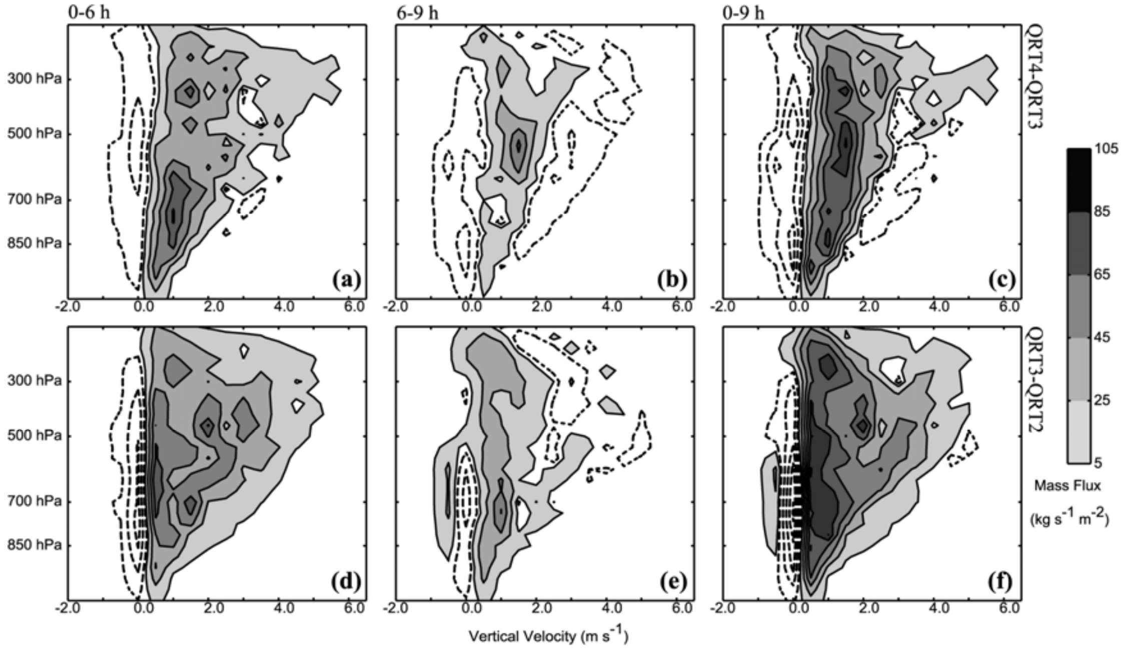

Figure 4.7. Difference in total vertical mass flux per unit area between (a-c) QRT4 and QRT3 and (d-f) QRT3 and QRT2 as a function of vertical velocity (m s^{-1} ; x-axis) and height. Differences are shown from (a,d) 0-6 h, (b,e) 6-9 h and (c,f) 0-9 h with positive (negative) differences shaded (dash-contoured) every 20 kg s^{-1} m^{-2} beginning at 5 (-5) kg s^{-1} m^{-2} .

velocity bins (from -2 m s^{-1} to 6.5 m s^{-1}) with each σ-level retaining its own set of bins. Vertical mass flux is then summed for all grid point *w* values in each bin, and the difference in resulting sums between QRT4 and QRT3 and between QRT3 and QRT2 is contoured as a function of updraft velocity and height. Positive values in Fig. 4.7a,c indicate greater upward flux in QRT4 than QRT3, and positive values in Fig. 4.7b,d indicate greater upward flux in QRT3 than QRT2.

Convection is clearly stronger during the first 6 h in simulations with higher instability. Figure 4.7a,d shows that net 0-6-h upward mass flux increases incrementally from QRT2 to QRT4 for nearly all updraft speeds at any given level. An exception is that the very strongest updrafts in QRT3 are stronger than those in QRT4, but this represents only one or two updrafts. The greatest upward fluxes in QRT4 indicate that updrafts of a particular intensity cover a greater area and/or last longer in that simulation. Likewise, QRT2 has weaker upward mass flux than the other two simulations.

4.4.2. Cold pools

Also associated with the stronger convection in the more unstable simulations are stronger downdrafts that lead to substantial drops in surface θ_e. While θ_e rises during the first few hours due to horizontal advection and oceanic heat fluxes, it drops proportionally with 6-h precipitation totals after convective initiation in QRT1 through QRT6. For example, although simulations QRT4 through QRT6 have higher initial θ_e, they also have more initial precipitation, and downdrafts quickly cool their surface to a value below that seen in the other simulations (Fig. 4.5h). As a testament to the strong downdrafts in QRT4, Fig. 4.7 shows that downward mass flux is unambiguously stronger for all downdraft speeds at all levels in QRT4 than in QRT3. Likewise, QRT3 has generally stronger downward mass flux than QRT2, especially during the first 6 h.

An interesting result in Fig. 4.5h is that the cold pool strength in QRT3 is more similar to QRT2 than the other convectively active cases from 6-12 h. Although the reason for this is not entirely clear, it will be discussed in more detail in section 5. For now, the important result is that QRT3 has substantially more convection than QRT2, but it does not have as strong of a cold pool as QRT4, QRT5, and QRT6.

Widespread colder surface air eventually diminishes updrafts near the centers, especially in QRT4 through QRT6. Figure 4.7b reveals that 6-9-h total updraft flux in QRT3 surpasses that in QRT4 for stronger updrafts over much of the troposphere, which is a substantial change from the 0-6-h total in Fig. 4.7a. The difference between Fig. 4.7a-b is a result of the surface cold pool in QRT4 reducing instability and therefore the number of strong updrafts near the center after 6 h. Although mean vertical motion in QRT4 remains positive through 9 h (Fig. 4.5a), it becomes negative for a period between 9 and 12 h. There is also subsidence from 9-12 h in QRT5 and QRT6, and storm-scale 700-hPa w is lower in QRT4 through QRT6 than any of the other simulations during this period (Fig. 4.5a). QRT4 through QRT6 also generally produce less precipitation than QRT2 and QRT3 from 9-15 h (Fig. 4.5b). Simulations QRT2 and QRT3 also exhibit substantial drops in θ_e and precipitation totals due to cold downdrafts by 12 h, and the period from 12 to 24 h is convectively the least active period for all developing simulations.

4.4.3. Vorticity production: A response to convection

Simulations with greater net vertical mass flux should also have stronger production of vertical vorticity via stretching deformation. Vorticity budgets (not shown) and the time evolution of storm-scale vertical vorticity (displayed as a function of height in Fig. 4.8) indicate that there indeed is a tendency for vorticity to strengthen from simulation QRT2 to QRT4. A vorticity maximum initially between 700 and 850 hPa grows stronger and deeper with time, and around 6 h there is a rapid increase in storm-scale

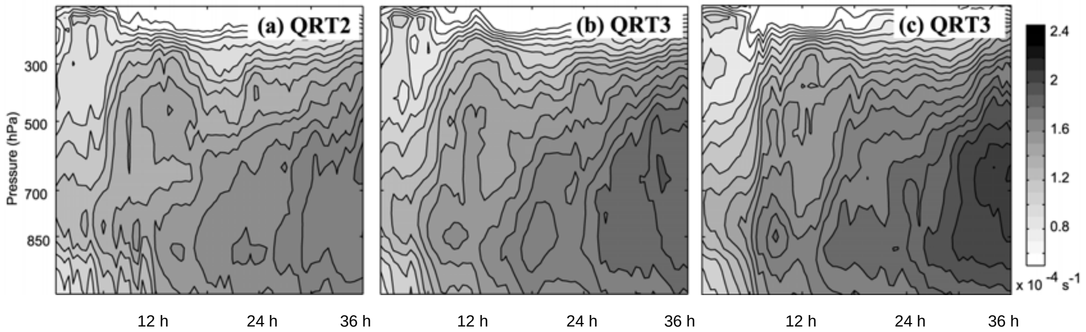

Figure 4.8. Evolution of the vertical distribution of vorticity (every 2×10^{-5} s^{-1}) averaged over the storm scale region for (a) QRT2, (b) QRT3 and (c) QRT4, respectively.

vorticity through the entire depth of the troposphere in all three simulations. Thus, incrementally higher precipitation totals in QRT3 and QRT4 lead to incrementally higher vorticity values through much of the troposphere.

The response in storm-scale vorticity to the widespread downdrafts and cold pools can also be seen in Fig. 4.8. Storm-scale vorticity decreases somewhat after 9 h in QRT3 (Fig. 4.8b), and it decreases strongly in QRT4 (Fig. 4.8c). This is consistent with stronger downdrafts and negative mean 700-hPa *w* in QRT4.

4.4.4. Recovery period and beyond

In the absence of widespread convection, the planetary boundary layer (PBL) recovers from the prolific cold pools present at 12 h. When θ_e reaches 355-357 K (at about 24 h), persistent convection begins again at the circulation centers of the active simulations. Storm-scale θ_e becomes higher in the simulations with weaker cyclogenesis because there is less convection producing downdrafts in those simulations. As rainfall begins to increase again in QRT2 through QRT4, the vortices grow stronger and deeper (Fig. 4.8) with higher surface wind speeds and heat fluxes (Fig. 4.5). Simulations QRT4, QRT5, and QRT6 all exhibit impressive increases in maximum wind speed after 24 h, and peak surface winds at 36 h are nearly twice those at 24 h.

Interestingly, stronger storms tend to have more storm-scale precipitation after the recovery period. One possible reason for this is that Ekman pumping is stronger in the simulations with stronger storm-scale circulations. Increased boundary layer forcing in these simulations could conceivably ignite more widespread convection than in the weaker simulations. Another possible reason for the relationship between precipitation and system strength is quasi-geostrophic lift caused by shear-vortex interaction. For example, when convection reignites in the developing cases, it tends to do so downshear to downshear-left of the vortex center (not shown). Since this is known to be a favorable location for lift due to shear-vortex interactions (Frank and Ritchie 1999, 2001; Rogers et al. 2003; Jones 1995, 2000a,b), it is plausible that this mechanism acts to enhance convection in these experiments. If this is the case, stronger lift is expected when either the vortex or shear is stronger (to the limiting extent that shear does not destroy the vortex). In the present simulations, it appears that a combination of *both* stronger vortices and stronger deep-layer (i.e., 200-850-hPa) shear could be enhancing precipitation after 24 h (deep-layer shear is 4-8 m s^{-1} in QRT5 and QRT6 during this period, while it is 3-4 m s^{-1} in the other simulations), but the full extent to which this is the case is beyond the scope of this study.

4.5 Effects moist convection: Local scales

Although the previous section showed that storm-scale quantities are well behaved in the sense that very small incremental changes in initial conditions produce incremental changes in storm-scale strength, local-scale strength metrics are less predictable. For example, from 6 to 24 h the absolute maximum vorticity in QRT4 is significantly less than that in QRT3 and about the same as that in QRT2 (Fig. 4.5f). Maximum wind speed, another local-scale strength metric that is used operationally to classify tropical cyclones, is also greater in QRT3 than QRT4 for an extended period of time. This section explores precisely why local-scale metrics are less predictable and can give significantly different estimates of relative strength than their storm-scale counterparts might imply.

4.5.1 Divergence between QRT3 and QRT4

What physical processes lead to the seemingly chaotic behavior that QRT3 has the highest maximum surface vorticity of all simulations and maximum winds much stronger than in QRT4 (Fig. 4.5) despite having lower instability? First, recall from section 4 that the developing cyclone in QRT4 has *both* stronger updrafts and downdrafts during the first 6 h. Accompanying the strong downdrafts in QRT4 is low-θ_e air that quickly diminishes convective intensity near its center. It will be shown here that, not only do the strong downdrafts in QRT4 diminish its convection, but they also catastrophically interfere with the primary VHT that forms during the first 6 h of QRT4. Although

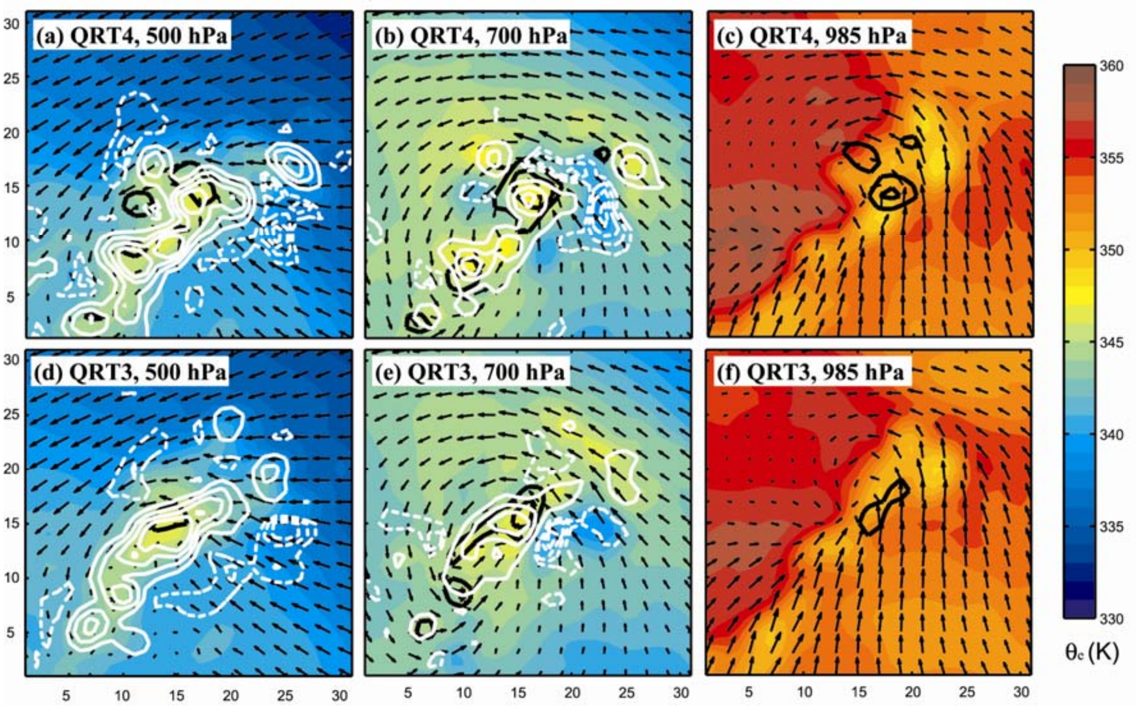

Figure 4.9. As in Fig. 4.4 except that all variables are time averaged from 4-5 h and displayed for the simulation and level indicated in each panel. In addition, vertical velocity is contoured every 0.5 m s^{-1} for positive values (solid white) and every 0.1 m s^{-1} for negative values (dashed white).

QRT4 does develop more numerous VHTs than QRT3, they are all weaker than the strongest VHT in QRT3.

In order to answer the introductory question to this subsection, a period is examined before QRT3 and QRT4 strongly diverge, and around when convection reaches its peak intensity (as determined by mean 700-hPa *w* in Fig. 4.5). Specifically, Fig. 4.9 shows the spatial distribution of updrafts and downdrafts in relation to the incipient VHT in both QRT3 and QRT4. Time averaged (i.e, an average of 4, 4.5 and 5-h) wind vectors, absolute vorticity, vertical velocity, and θ_e at different levels are displayed.

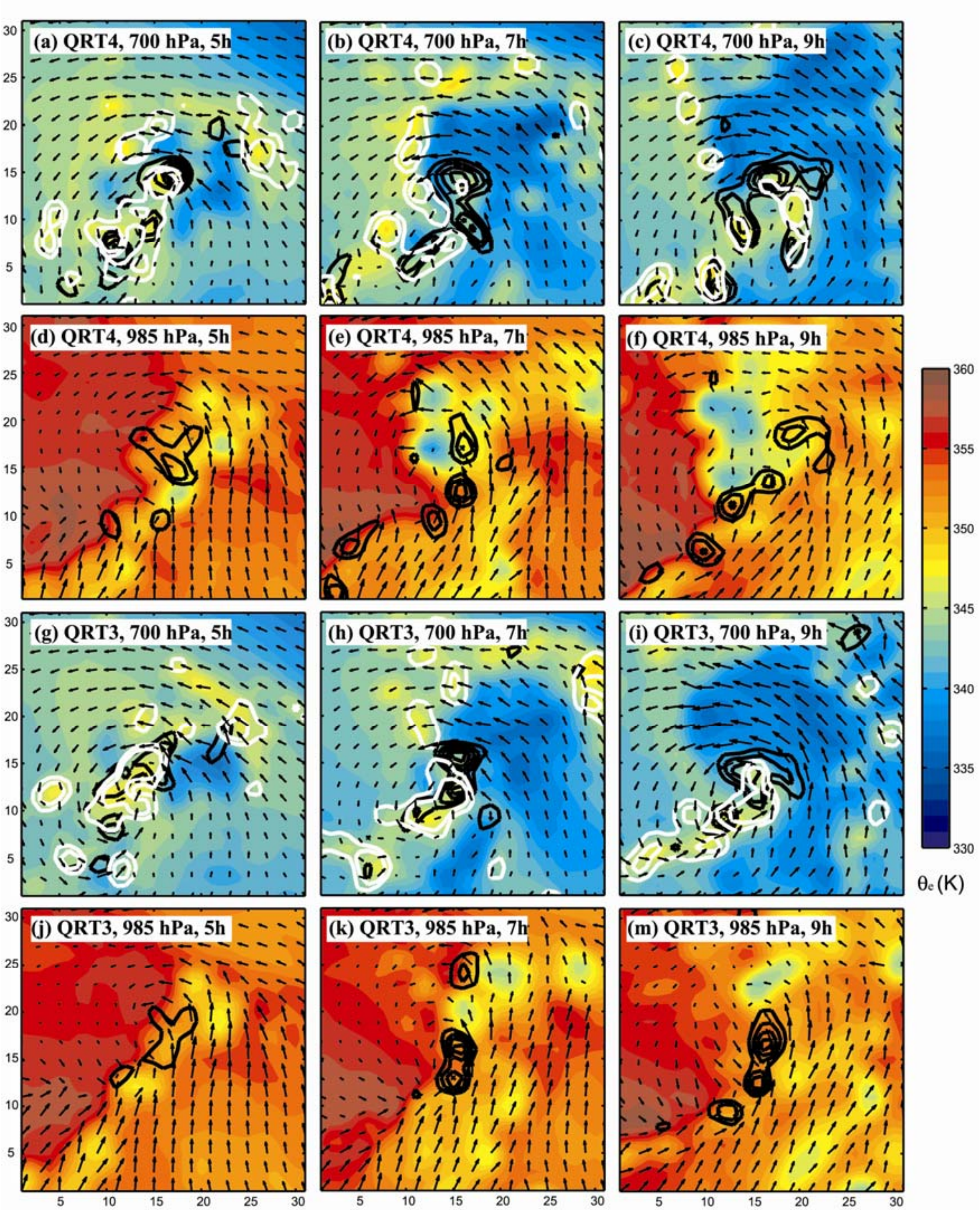

Figure 4.10. As in Fig. 4.4 except that all variables are displayed for the simulation, level, and time indicated in each panel.

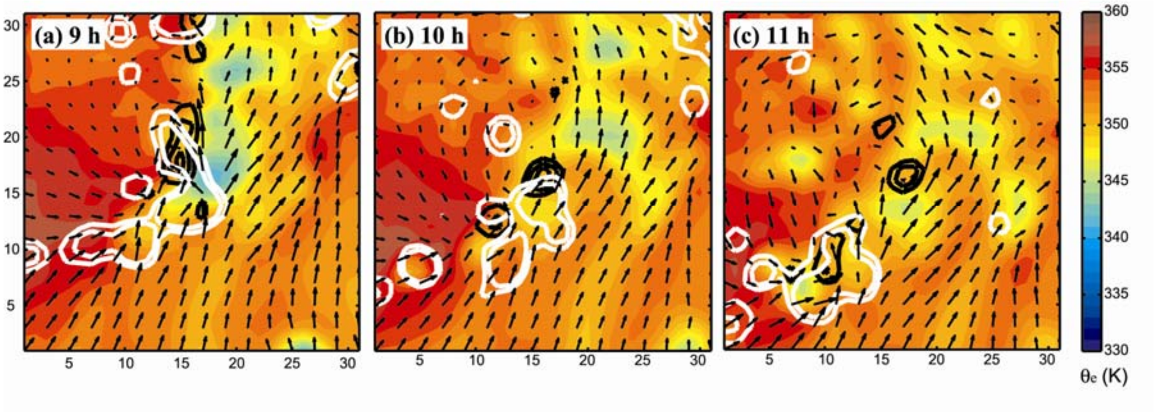

Figure 4.11. As in Fig. 4.4, except that variables are shown for QRT2 at the time indicated in each panel.

In a manner consistent with Fig. 4.7, the initially stronger convection in QRT4 is associated with more numerous and stronger downdrafts in the vicinity of the VHT than in QRT3. A band of downdraft wraps from southeast to north of the vorticity tower in QRT4 (Fig. 4.9b), but in QRT3 the downdraft area is discontinuous and weaker (Fig. 4.9d-e). Associated with the encircling band of downdraft in QRT4 is a band of low-θ_e air at mid levels. The slightly lower θ_e air northeast of the center in QRT4 at 985 hPa (compare Fig. 4.9c and Fig. 4.9f) is a sign that the effects of the downdraft have begun to reach the surface.

Though generally stronger downdrafts decrease initial θ_e around the VHT in QRT4 more than in QRT3, the formation of a convective line and an associated cold pool reduces QRT4 θ_e to even lower values. To demonstrate this, Fig. 4.10 shows instantaneous velocity vectors, vertical velocity, and θ_e at 5, 7, and 9 h for QRT3 and QRT4. After the low-θ_e air on the north side of the vorticity center in QRT4 penetrates to the surface (Figs. 4.9c and 4.10d), a north-south oriented convective line forms on the interface of high- and low-θ_e air immediately west of the center (Fig. 4.10b). The convective line, which seems to form as a result of forcing along the θ_e boundary, lasts from about 6.5 to 8.5 h. Downdraft formation behind the line strongly reinforces the cold pool (Fig. 4.10e-f) and seems to be a primary reason why storm-scale surface θ_e decreases more in QRT4 than in QRT2 and QRT3 (which do not have such a line).

As a result of the widespread cold pool, the QRT4 VHT loses its access to unstable air and begins to dissipate. Figure 4.11e shows that low θ_e air has been drawn into the VHT by 7 h, and most of the substantial updrafts are to the south and west. After 9 h (not shown) the 700-hPa vorticity maximum becomes displaced to the southwest of the surface-850-hPa remnant vortex, and the original surface vorticity maximum further weakens in the absence of convection.

The 700-hPa remnant vortex in QRT4 survives as it moves southwest and encounters further convection, but its survival is short-lived (not shown). At 9 h the 700-hPa vorticity center is about 20 km north of the leading edge of the cold pool (Fig. 4.10c,f), and by 9.5 h the anomaly is being strengthened again by convective updrafts forming on the boundary. In fact, a new VHT builds all the way down to the surface amidst the new convection, and surface vorticity beneath the mid-level anomaly strengthens dramatically by 10.5 h. However, by 12 h the new VHT moves back over the cold pool, the convection diminishes, and the 700-hPa remnant vortex begins to dissipate. Around 20 h, the vorticity remnants of the newer VHT merge with the old low-level vortex from the first VHT (not shown).

While the spreading cold pool in QRT4 clearly leads to the demise of the principal VHT that forms within the first 6 h, storm-scale vorticity remains stronger in QRT4 than in QRT3 (Fig. 4.5e, Fig. 4.8). Though the ultimate reason for the stronger storm-scale vorticity in QRT4 is more storm-scale convection, phenomenologically, the stronger QRT4 vorticity is associated with more numerous VHTs. In QRT2 through QRT6, convection first forms on an inverted-V shaped convergence line, and the main VHT forms at the apex of the ‘V’. After VHT formation, the western extension of the convergence line (i.e., that oriented southwest to northeast and terminating at the circulation center in Fig. 4.10d-f) acts as a focus for further convection, which is where the additional VHTs in QRT4 form. Although the primary VHT in QRT4 is disrupted, there are more VHTs in QRT4 along the western leg of the convergence line (e.g., compare Fig. 4.10e,k). These VHTs have access to the pristine air to the southwest of the center, which is more unstable in QRT4 than that in QRT3, and their individual circulations contribute to the storm-scale circulation. The more abundant QRT4 VHTs in Fig. 4.10 represent a trend for the simulation; through the first 20 h, a total of 12 VHTs form in QRT4, whereas only 6 form in QRT3.

The local-scale evolution in QRT3 is clearly much different than QRT4, largely because QRT3 lacks the strong cold pool that forms on the northwest side of the QRT4 VHT. With initially weaker updrafts from 4 to 5 h in QRT3 (Fig. 4.7), the compensating downdrafts and cold pool are weaker by 5 h. Perhaps not coincidentally, a convective line fails to materialize along the edge of the weaker cold pool (Fig. 4.10h,k), though *some* convection does occur at that location. Without the convective line, significantly less low-θ_e air penetrates to the surface, and the QRT3 VHT enjoys practically uninhibited access to the unstable air to its southwest. The effect on the surface vorticity field is substantial in Fig. 4.10k-m, where a strong surface vorticity core builds beneath the 700-hPa anomaly.

An additional factor that contributes to low-level vortex intensification in QRT3 is the merger of multiple smaller vorticity anomalies with the main VHT. As in QRT4, the western extension of the initial convergence line acts as a focus for further convection, and vorticity anomalies form within convective cells as they move northeastward toward the circulation center (see Fig. 4.10m). In QRT4 the spreading cold pool prevents these anomalies from reaching the center, but in QRT3 the primary VHT merges with a number of these anomalies strengthens between 6 and 12 h.

4.5.2 Divergence between QRT2 and QRT3

The previous subsection demonstrates that unobservable large-scale initial condition differences between QRT3 and QRT4 result in strong differences in the intensity and placement of updrafts and cold pools. This eventually leads to a different route to tropical cyclogenesis between QRT3 and QRT4. The initial condition difference between QRT2 and QRT3 is exactly the same as that between QRT3 and QRT4, and this subsection examines *what physical processes lead QRT2 to fail to develop a well-organized tropical cyclone* (e.g., Fig. 4.3b).

Recall from Figs. 4.5 and 4.8 that storm-scale changes in strength correspond to incremental changes in initial conditions. Just as QRT4 has more initial storm-scale precipitation than QRT3 due to higher initial instability, QRT3 also has more precipitation than QRT2. Likewise, despite the fact that QRT2 is significantly less organized than QRT3 after 36 h (Fig. 4.3), its storm-scale strength follows the general pattern of incremental differences in Fig. 4.7.

In addition to being weaker on the storm scale, QRT2 is significantly weaker than QRT3 on the local scale after about 9 h (Fig. 4.5). The cause of the local-scale weakness is the failure of QRT2 to maintain a predominant VHT (or even a remnant VHT vortex), as in QRT4 (discussed below). An important difference between QRT2 and QRT4, however, is that QRT4 establishes a stronger storm-scale vortex during the first 6-12 h. Even if it produced the same convection after the recovery period (i.e., after 24 h), QRT2 should take longer to re-establish a strong VHT than QRT4 since the storm-scale vorticity in QRT2 is considerably lower (and thus there is less potential for stretching deformation). Not only is the vorticity environment less favorable for strong VHT formation in QRT2, but QRT2 also has less storm-scale convection/precipitation from 24-36 h (see section 4.4). Seeing as how convection clearly contributes to VHT formation (e.g., Hendricks et al. 2004, Montgomery et al. 2006), it appears that differences in storm-scale intensity strongly modulate the ability of QRT2 to develop a stronger VHT after 24 h. The remainder of this subsection will focus on the reasons why the original vorticity tower in QRT failed to maintain itself in the first place.

Surface cold pools ultimately lead to the destruction of the QRT2 VHT, but the precise sequence of events here is somewhat different than in QRT4. Low θ_e air forms on the east side of the circulation center in QRT2 as early as 7 h and has some negative

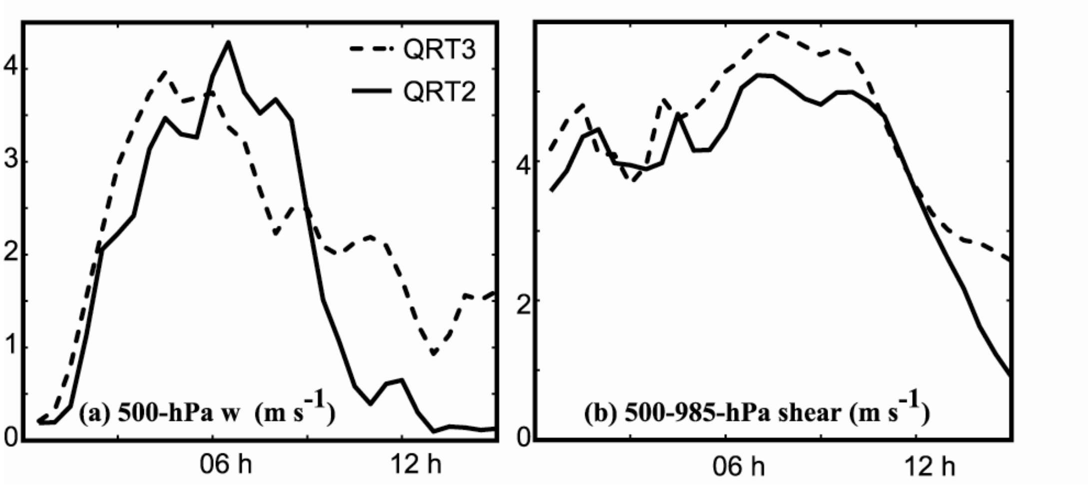

Figure 4.12. The time evolution of (a) maximum 500-hPa vertical velocity (m s^{-1}) within 50 km of the center (smoothed with a 3-point smoother) and (b) 500-985-hPa vertical wind shear (m s^{-1}) averaged in the storm-scale region in QRT2 and QRT3.

impact on the low-level vortex (not shown). However, because this cold pool is to the east of the VHT, the warm inflow from the southwest is not disrupted at this time. It is a few hours later that surface outflow from convection to the southwest of the QRT2 center is well positioned to disturb VHT inflow and suppress updrafts. After 9 h all convection in QRT2 is well southwest of the remnant vorticity center (Fig. 4.11).

The disruption of convection near the center in QRT2 comes at a time when low-level vertical wind shear is fairly high, a factor that leads to the quick demise of the QRT2 VHT. Figure 4.12 shows both the evolution of maximum 500-hPa *w* within 50 km of the center and 700-985-hPa vertical wind shear averaged over the storm-scale region for QRT2 and QRT3. In QRT2, 500-hPa *w* quickly diminishes after 9 h, a time when shear is still fairly high. Figure 4.13, which shows data similar to Fig. 4.10 at 500

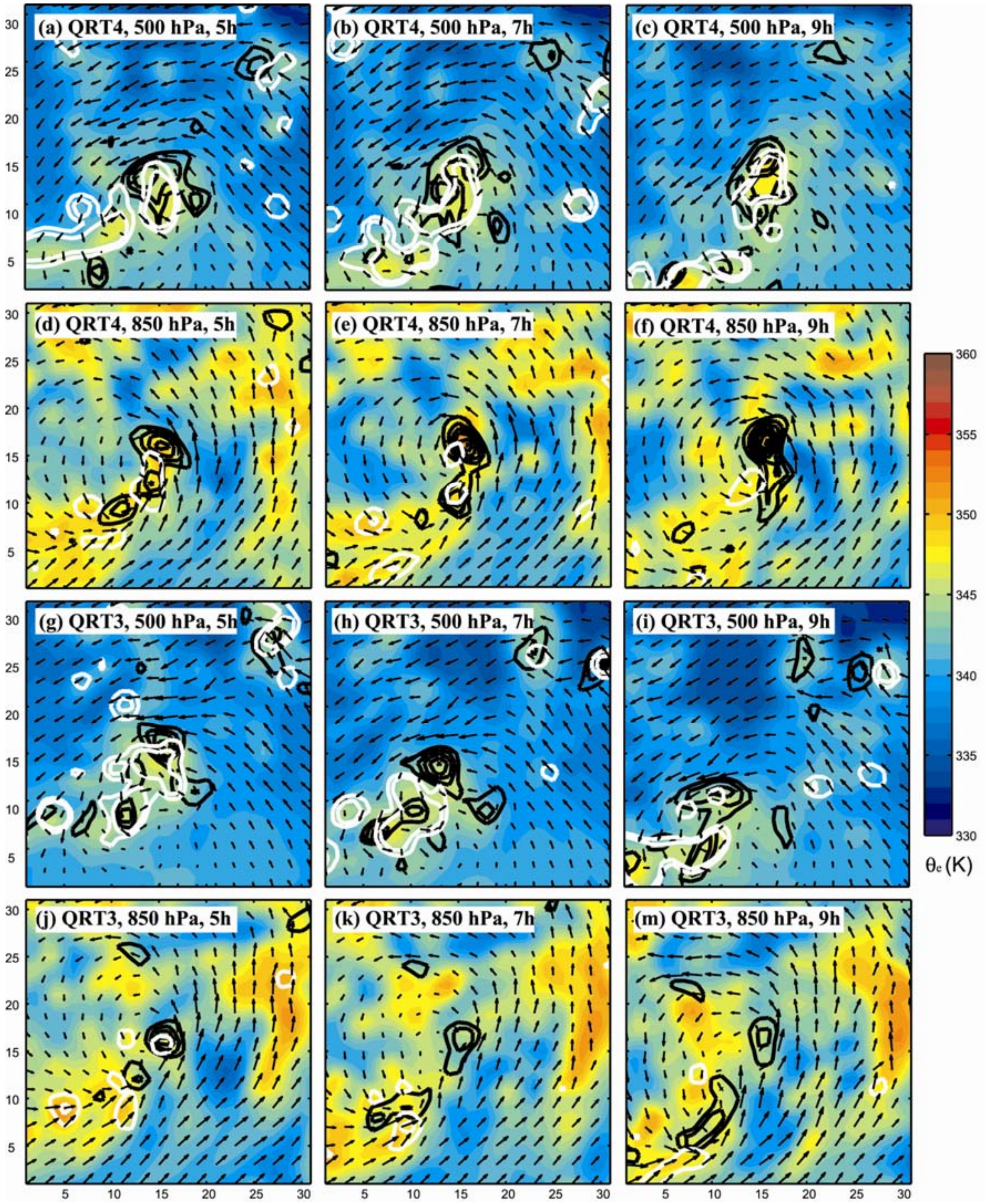

Figure 4.13. As in Fig. 4.4, except that all variables are displayed for the simulation, level, and time indicated at the top of each panel.

hPa and 850 hPa, demonstrates the combined negative effects of surface cold pools and shear in QRT2. The surface cold pool disrupts convection through the vorticity tower, and the last updraft through the tower occurs around 9 h (Fig. 4.13j). Thereafter, the low-level remnant vortex weakens (Fig. 4.13k-m), and the mid-level vortex advects to the southwest under the influence of northeasterly wind shear (Fig. 4.13h-i). Meanwhile, convective updrafts in QRT3 continue to strengthen its VHT well past 9 h (Fig. 4.13a-f) due to continued access to warm surface air from the southwest (as in Fig. 4.11). The VHT-sustaining convection in QRT3 also weakens somewhat (Fig. 4.12a), but it reaches a minimum after wind shear has significantly diminished (Fig. 4.12b). Thus, the low-level vortex in QRT3 remains intact long enough to get into a weaker shear environment, which is more favorable for development. A similar evolution to that seen in QRT2 and QRT3 (i.e., a 'fight' between convection and wind shear for the strength of the vortex) was found in Tory et al. (2007).

In short summary, this section demonstrates that unobservable large-scale initial condition uncertainties may result in strong differences in the intensity and maintenance of VHTs. In QRT2, the destruction of the primary VHT is particularly disastrous for the cyclone's later organization since the larger scale vortex is weaker and less able to support the rapid redevelopment of another strong VHT. In some sense, this and the previous subsection demonstrated that QRT3 is an anomaly since surface cold pools lead to the demise of the principal VHT in QRT2 and QRT4, but not in QRT3. The cyclone in QRT3 seems to enjoy the benefits of more convection than QRT2, but it does not have quite enough convection (or quite the necessary convective mode) to develop the strong cold pool seen in QRT4. With a strong, low-level remnant vortex intact through 24 h, the QRT3 cyclone is primed to establish a very strong central vortex (and well organized core, see Fig. 4.3c). Thus, small initial condition differences can lead to different routes to tropical cyclogenesis (e.g., QRT3 and QRT4) or to differences in whether or not a well-organized tropical cyclone will form (e.g., QRT2 and QRT3). Such randomness in moist convection may ultimately limit the predictability of some tropical cyclones.

4.5.3 Simulations QRT5 and QRT6

Simulations QRT5 and QRT6 behave similarly to QRT4, though they do exhibit hints of QRT3 behavior. Like QRT4, they have strong, cold downdrafts near the initial VHT center, and they both develop a convective line with a substantial cold pool (which is still evident at 9 h in Fig. 4.4). Also as in QRT4, the strongest local-scale vorticity anomaly that develops within the first 6 h of QRT5 and QRT6 is destroyed by the downdrafts. The VHTs in both simulations, which are stronger and more numerous than those QRT4 (see Fig. 4.4 and Fig. 4.5f), incrementally contribute to stronger storm-scale circulations.

The VHT-destroying downdrafts in QRT5 behave similarly to the downdrafts in QRT4 (Figs. 4.9c, 4.11d-f), though the QRT5 downdrafts are colder. A similar convective line to that in QRT4 forms with very low θ_e air behind it, and the initial VHT does not survive (the only trace of it in Fig. 4.4a is the decaying vorticity maximum immediately northwest of A1). However, another VHT (B1 in Fig. 4.4a) advects into the storm-scale region around 6-7 h and is one of the stronger vortices present in QRT5. Updrafts more or less remain over B1 through 13 h, and the remnant vortex stays intact through 24 h and eventually becomes collocated with the storm-scale center. Around 24 h, new convection ignites over B1 at the same time that other strong vortices develop within nearby convection, and the collection of vortices merge to form an even stronger center (not shown).

There are several differences between QRT5 and QRT6. First, initial downdrafts in QRT6 are even colder than those in QRT5. In fact, they are sufficient to extinguish updraft of the primary VHT before the convective line even forms (the VHT remnants are no longer identifiable in Fig. 4.4b). Also, although VHT B2 advects into the storm-scale region of QRT6 similarly to B1 in QRT5, B2 never becomes associated with the storm-scale center. Rather, convection with B2 dissipates after 9 h, and its remnant vorticity decays. The low-level vorticity eventually associated with the system center in QRT6 can be traced back to a VHT that forms to the southwest of the initial QRT6 VHT as it decays around 6 h (not shown). Although its updrafts also diminish, its remnant low-level vorticity (A2 in Fig. 4.4b) becomes collocated with the storm-scale circulation center around 18-20 h.

4.6. Discussion

Through sensitivity experiments of a Gulf of Mexico tropical disturbance, this study highlights limited predictability that can be present in short-term tropical cyclone intensity forecasts given minute analysis uncertainties in the large-scale environment. Whether or not a tropical cyclones forms is found to depend on initial condition differences much smaller than current analysis error. The sensitivity is the result of how initial convection responds to differences in the initial environment from one simulation to the next. The amount of convection early in the simulations, which is modulated by the initial convective instability, is instrumental in forming a deep vortex. Also, widespread cold convective downdrafts that form during the convection subsequently damp convective activity in a period that sees neither vortex growth nor decay. After the boundary layer recovers, convection reignites and stronger vortices strengthen more quickly.

In some ways the large-scale flow sets the tone for small-scale convective details, but randomness in the details of small-scale convection may also lead to differences in storm-scale organization and subsequent error growth to larger scales. For example, there is a tendency to have more small-scale VHTs when there is stronger initial convective instability in the larger-scale environment (despite immeasurable differences in the initial analyses). These VHTs incrementally contribute to the storm-scale circulation in simulations with stronger storms. Yet the details of how the storm-scale vortex is built (i.e., the route to genesis) significantly depend on the same initial condition differences. This is due to chaotic interactions of mesoscale features whose timing and placement significantly vary with slight initial condition differences.

Both storm-scale and local-scale evolution are quite unpredictable in the Gulf low, but the local scales are less predictable than the storm scale. Storm-scale differences vary approximately linearly with the differences in storm-scale initial conditions, which implies some degree of predictability. Yet, the storm-scale evolution is unpredictable from a practical standpoint because unobservable changes in initial conditions result in very large changes in the system evolution. The local scales are less predictable because differences in maximum winds and/or vorticity vary nonlinearly with initial condition differences and depend on the timing and intensity of small mesoscale features such as VHTs and cold pools. This demonstrates that, from a predictability standpoint, the operational “maximum sustained wind” metric is far more difficult to predict than an area-average metric of intensity.

Finally, the strong sensitivity exemplifies the inherent uncertainties in hurricane intensity prediction where moist convection is the key that limits predictability, a result similar to findings regarding extratropical winter snowstorms (Zhang et al. 2002, 2003, 2007) and idealized tropical cyclones (Van Sang et. al 2008). Yet, the current results are apparently limited by how accurately the 3.3-km simulations can faithfully represent the essential dynamics of moist convection. In addition, small-scale uncertainty is not included in the initial conditions of this study. Therefore, future studies should examine how both model error and smaller scale uncertainty may lead to even stronger forecast divergence.

CHAPTER V

CONCLUSIONS

Through methodology unique for tropical cyclones in peer-reviewed literature, this study uses ensemble forecasts and sensitivity analysis to explore how the dynamics of moist convection affects predictability of tropical cyclogenesis in the MM5 and WRF models. The statistical analyses are largely congruent with those of H07, but this study refines their correlation methodology by looking at both large and small scale processes. Additional steps are taken by investigating the sensitivity of predictability and dynamics to cumulus parameterization (model error) and to ensemble initial condition changes that produce weaker and stronger cyclones. Finally, the sensitivity to practically immeasurable changes in initial conditions is analyzed to help understand the intrinsic predictability limit of tropical cyclones.

Chapter II shows that the rate of intensification of a 2004 Gulf-of-Mexico disturbance in an ensemble MM5 forecast depends on the amount of initial convective instability (MUCAPE) and deep moisture in the ensemble. MUCAPE is related to the strength of surrounding quasi-geostrophic lift, and along with mid-level moisture it modulates convective intensity during the first 6-12 h. Differences in convection result in quicker genesis in some ensemble members than others. Thus, these factors are the primary source for ensemble spread by 12 h, and spread is thereafter amplified by differences in convection related to oceanic heat fluxes. Eventually the WISHE mechanism results in even larger ensemble spread. The above results generally hold even in the face of model error (i.e., cumulus parameterization) and changes to the initial ensemble mean, though such changes do alter properties of convection, ensemble spread and the time it takes to exit the CAPE-based intensification regime.

Chapter III is intended as a follow-up study to Chapter II and investigates the intensification of Hurricane Humberto, which made landfall along the upper Texas coast in September 2007. Perhaps the most important result from Chapter III is general confirmation of the results from Chapter II. In the Humberto ensemble, mid-level moisture and MUCAPE again modulate the intensity of convection, which governs the rate of intensification. In this case, MUCAPE variance is related to the proximity and strength of a nearby surface front, and thus varying degrees of interaction between the developing cyclone and the front ultimately cause much of the ensemble spread. As in the 2004 low, strength-dependent heat fluxes and WISHE also act to increase existing ensemble spread. In addition, ensemble members make landfall at different times, which drives spread even higher.

With the mechanism by which spread increases in Chapter II confirmed as generally realistic, Chapter IV returns to the 2004 gulf low to investigate the sensitivity of its genesis to minute changes in initial conditions. Whether or not a tropical cyclones forms is found to depend on initial condition differences much smaller than current analysis error. The sensitivity is the result of how initial convection responds to differences in the initial environment from one simulation to the next. The amount of convection early in the simulations, which is modulated by the initial convective instability, is instrumental in forming a deep vortex.

Both storm-scale and local-scale evolution are quite unpredictable in the Gulf low, but the local-scales are less predictable than the storm scale. Storm-scale differences vary approximately linearly with the differences in storm-scale initial conditions, which implies some degree of predictability. Yet, the storm-scale evolution is unpredictable from a practical standpoint because unobservable changes in initial conditions result in very large changes in the system evolution. The local scales are less predictable because differences in maximum winds and/or vorticity vary nonlinearly with initial condition differences and depend on the timing and intensity of small mesoscale features such as VHTs and cold pools. This demonstrates that, from a predictability standpoint, the operational “maximum sustained wind” metric is far more difficult to predict than an area-average metric of intensity.

In general, this study has pinpointed the source of error in forecasts of two very different tropical cyclones; to the knowledge of the author, this has never before been accomplished. Generally similar results were obtained in spite of differences in storm development, methodology, and uncertainty source. For instance, Chapter II studied a non-developing gulf low with a cold-start MM5 ensemble and found the source of uncertainty to largely stem from uncertainty associated with the quasi-geostrophic circulation. Chapter III studied a formidable landfalling, Category 1 hurricane with a hot-start WRF ensemble and found the source of uncertainty to largely originate from uncertainty in the cyclone’s interaction with a front. Yet in both of these cases, high MUCAPE and mid-level moisture were found to benefit genesis.

The importance of initial deep moisture here agrees with numerous other tropical cyclone modeling and observational studies, but the demonstrated importance of CAPE is new. Montgomery et al. (2006) noted that vertical hot towers (VHTs) appear to "compete" with one another for ambient CAPE, and the results of Chapter IV suggest that higher CAPE in the case of the gulf low generally favors stronger and/or more numerous VHTs. The vorticity in these VHTs incrementally contributes to the system-scale circulation, and their convective cores contribute to system-scale heating.

The strong sensitivity to initial condition differences in both cases exemplifies the inherent uncertainties in hurricane intensity prediction where moist convection is the key that limits predictability, a result similar to findings regarding extratropical winter snowstorms (Zhang et al. 2002, 2003, 2007). The current study implies that the predictability of tropical cyclones may be strongly limited at all time scales, ranging from day 1 to long-term projections. This remains true regardless of whether one uses statistical methods (Hoyos et al. 2006) or numerical weather/climate prediction models (Davis et al. 2008; Houze et al. 2007; Oouchi et al. 2006). The limit of intensity predictability given realistic initial condition and model errors (which are still large at present) in numerical weather prediction models may be alleviated through improving our understanding of dynamics and physics, development of better numerical models, and improved data coverage and assimilation techniques. However, there will always be forecast errors due to the inherent limit of predictability arising from initial errors with amplitudes far smaller than any observation and analysis system; these are errors that society will always have to cope with (Pielke et al. 1997).

Finally, inherent uncertainties in hurricane forecasts illustrate the need for developing advanced ensemble prediction systems to provide event-dependent probabilistic forecasts and risk assessment. In practice, despite an increasing role and demonstrated benefits of using ensembles in aiding deterministic hurricane forecasting (Krishnamurti et al. 1999; Z08), the uncertainty issued with today's operational hurricane forecasts is still based on averaged climatological errors and is not case-dependent. Thus, this study also has strong implications related to how society might better distribute resources to combat future hurricane-related disasters given that the number of hurricanes and their intensity/destructiveness are reportedly on the rise with the warming climate (Emanuel 2005; Webster et al. 2005).

REFERENCES

Aberson, S. D., 2001: The ensemble of tropical cyclone track forecasting models in the North Atlantic basin (1976-2000). *Bull. Amer. Meteor. Soc.,* **82,** 1895-1904.

Arakawa, A. 2004: The cumulus parameterization problem: Past, present, and future. *J. Climate,* **13,** 2493-2525.

Barker, D. M., W. Huang, Y. R. Guo, A. J. Bourgeois, and Q. N. Xiao, 2004: A three-dimensional variational data assimilation system for MM5: Implementation and initial results. *Mon. Wea. Rev.,* **132,** 897-914.

Bender, M. A., I. Ginis, and Y. Kurihara, 1993: Numerical simulations of tropical cyclone–ocean interaction with a high-resolution coupled model. *J. Geophys. Res.,* **98,** 23245–23263.

Bister, M., and K. A. Emanuel, 1997: The genesis of Hurricane Guillermo: TEXMEX analyses and a modeling study. *Mon. Wea. Rev.,* **125,** 2662-2682.

Black, P. G., 1983: Ocean temperature changes induced by tropical cyclones. Ph.D. dissertation, The Pennsylvania State University, 278 pp.

Braun, S., 2006: High-resolution simulation of Hurricane Bonnie (1998). Part II: Water budget. *J. Atmos. Sci.,* **63,** 43-64.

Braun, S., M. T. Montgomery, and Z. Pu, 2006: High-resolution simulation of Hurricane Bonnie (1998). Part I: The organization of eyewall vertical motion. *J. Atmos. Sci.,* **63,** 19-42.

Cohen, C., 2002: A comparison of cumulus parameterizations in idealized sea-breeze simulations. *Mon. Wea. Rev.,* **130,** 2554-2571.

Crook, N. A., 1996: Sensitivity of moist convection forced by boundary layer processes to low-level thermodynamic fields. *Mon. Wea. Rev.,* **124,** 1767-1785.

Davis, C. A., and L. F. Bosart, 2002: Numerical simulations of the genesis of Hurricane Diana (1984). Part II: Sensitivity of track and intensity prediction. *Mon. Wea. Rev.,* **130,** 1100-1124.

Davis, C. A., and Coauthors, 2008: Prediction of landfalling hurricanes with the advanced hurricane WRF model. *Mon. Wea. Rev.,* in press.

DeMaria, M. and J. M. Gross, 2003: Evolution of prediction models. *Hurricane! Coping with Disaster: Progress and challenges since Galveston, 1900,* R. Simpson, Ed., American Geophysical Union, 103-126.

DeMaria, M., J. A. Knaff, and B. H. Connell, 2001: A tropical cyclone genesis parameter for the tropical Atlantic. *Wea. Forecasting,* **16,** 219–233.

DeMaria, M., M. Mainelli, L. K. Shay, J. A. Knaff, and J. Kaplan, 2005: Further improvements to the Statistical Hurricane Intensity Prediction Scheme (SHIPS). *Wea. Forecasting.,* **20,** 531-543.

Doswell, C. A. III, and E. N. Rasmussen, 1994: The effect of neglecting the virtual temperature correction on CAPE calculations. *Wea. Forecasting,* **9,** 625-629.

Dudhia, J., 1993: A nonhydrostatic version of the Penn State-NCAR Mesoscale Model: Validation tests and simulation of an Atlantic cyclone and cold front. *Mon. Wea. Rev.,* **121,** 1493-1513.

Dunion, J. P., and C. S. Velden, 2004: The impact of the Saharan air layer on Atlantic tropical cyclone activity. *Bull. Amer. Met. Soc.,* **75,** 353-365.

Emanuel, K. A., 1986: An air-sea interaction theory for tropical cyclones. Part I: Steady-state maintenance. *J. Atmos. Sci.,* **43**, 585-604.

Emanuel, K. A., 1989: The finite-amplitude nature of tropical cyclogenesis. *J. Atmos. Sci.,* **46,** 3431-3456.

Emanuel, K. A., 2003: A century of scientific progress: An evaluation. *Hurricane! Coping with Disaster: Progress and challenges since Galveston, 1900,* R. Simpson, Ed., American Geophysical Union, 177-204.

Emanuel, K. A., 2005: Increasing destructiveness of tropical cyclones over the past 30 years. *Nature,* **436,** 686-688.

Emanuel, K. A., J. D. Neelin, and C. S. Bretherton, 1994: On large scale circulations in convecting atmospheres. *Quart. J. Roy. Meteor. Soc.,* **120,** 1111-1144.

Frank, W. M., 1977: The structure and energetics of the tropical cyclone. I. Storm structure. *Mon. Wea. Rev.,* **105,** 1119-1135.

Frank, W. M., and E. A. Ritchie, 1999: Effects of environmental flow upon tropical cyclone structure. *Mon. Wea. Rev.,* **127**, 2044–2061.

Frank, W. M., and E. A. Ritchie, 2001: Effects of vertical wind shear on the intensity and structure of numerically simulated hurricanes. *Mon. Wea. Rev.*, **129**, 2249–2269.

Franklin, J. L., 2005: 2004 National Hurricane Center verification report. *Preprints*, 57th Interdepartmental Hurricane Conference, Miami, FL. [Updates are available on the official National Hurricane Center website: National Hurricane Center (NHC), www.nhc.noaa.gov/verification]

Gray, W. M., 1968: Global view of the origin of tropical disturbances and storms. *Mon. Wea. Rev.*, **96,** 669-700.

Gray, W. M., 1975: Tropical cyclone genesis. Dept. of Atmos. Sci. Paper No. 323, Colorado State University, 121 pp. [Available from Department of Atmospheric Sciences, Colorado State University, Ft. Collins, CO 80523.]

Goerss, J. S., 2000: Tropical cyclone track forecasts using an ensemble of dynamical models. *Mon. Wea. Rev.*, **128,** 1187-1193.

Grell, G. A., 1993: Prognostic evaluation of assumptions used by cumulus parameterizations. *Mon. Wea. Rev.*, **121,** 764-787.

Grell, G.A. and D. Devenyi, 2002: A generalized approach to parameterizing convection combining ensemble and data assimilation techniques, *Geophys. Res. Let.*, **29,** 10.1029/2002GL015311.

Grell, G. A., Y.-H. Kuo, and R. Pasch, 1991: Semi-prognostic test of cumulus parameterization schemes in the middle latitudes. *Mon. Wea. Rev.*, **119,** 5-31.

Hakim, G. J., and R. D. Torn, 2008: Ensemble synoptic analysis. *Fred Sanders, Meteor. Monogr.*, in press.

Harr, P. A., R. L. Elsberry, and J. C. Chan, 1996: Transformation of a large monsoon depression to a tropical storm during TCM-93. *Mon. Wea. Rev.*, **124,** 2625-2643.

Hawblitzel, D. P., F. Zhang, Z. Meng, and C. A. Davis, 2007: Probabilistic evaluation of the dynamics and predictability of the mesoscale convective vortex of 10-13 June 2003. *Mon. Wea. Rev.*, **135,** 1544-1563.

Hawkins, H. F., and S. M. Imbembo, 1976: The structure of a small, intense hurricane – Inez 1966. *Mon. Wea. Rev.*, **104**, 418-442.

Hendricks, E. A., M. T. Montgomery, and C. A. Davis, 2004: The role of “vortical” hot towers in the formation of tropical cyclone Diana (1984). *J. Atmos. Sci.*, **61**, 1209–1232.

Hong, S-.Y., J. Dudhia, S.-H. Chen, 2004: A revised approach to ice-microphysical processes for the bulk parameterization of cloud and precipitation., *Mon. Wea. Rev.*, **132**, 103-120.

Houze, R. A., S. S. Chen, B. F. Smull, W. C. Lee, and M. M. Bell, 2007: Hurricane intensity and eyewall replacement. *Science,* **315**, 1235-1238.

Hoyos, C.D., P. A. Agudelo, P. J. Webster, and J. A. Curry, 2006: Deconvolution of the factors contributing to the increase in global hurricane intensity, *Science,* **312,** 94-97.

Islam, S., R. L. Bras, and K. A. Emanuel, 1993: Predictability of mesoscale rainfalls in the tropics. *J. Appl. Meteor.*, **32**, 297-310.

Jones, S. C., 1995: The evolution of vortices in vertical shear: Initially barotropic vortices. *Quart. J. Roy. Meteor. Soc.,* **121,** 821–851.

Jones, S. C., 2000a: The evolution of vortices in vertical shear. II: Large-scale asymmetries. *Quart. J. Roy. Meteor. Soc.,* **126,** 3137–3159.

Jones, S. C., 2000b: The evolution of vortices in vertical shear. III: Baroclinic vortices. *Quart. J. Roy. Meteor. Soc.,* **126,** 3161–3185.

Krishnamurti, T. N., R. Correa-Torres, G. Rohaly, D. Oosterhof, and N. Surgi, 1997: Physical initialization and hurricane ensemble forecasts. *Wea. Forecasting,* **12,** 503-514.

Krishnamurti, T.N., and co-authors, 1999: Improved weather and seasonal climate forecasts from multimodel superensemble, *Science,* **285,** 1548–1550.

Krishnamurti, T. N., C. M. Kishtawal, Z. Zhang, T. LaRow, D. Bachiochi, E. Williford, S. Gadgil, and S. Surendran, 2000: Multimodel ensemble forecasts for weather and seasonal climate. *J. Climate,* **13,** 4196-4216.

Krishnamurti, T.N., S. Pattnaik, L. Stefanova, T. S. Kumar, B. P. Mackey, A. J. O'Shay, and R. J. Pasch, 2005: The hurricane intensity issue. *Mon. Wea. Rev.*, **133**, 1886-1912.

Kumar, T. S. V. V., T. N. Krishnamurti, M. Fiorino, and M. Nagata, 2003: Multimodel superensemble forecasting of tropical cyclones in the Pacific. *Mon. Wea. Rev.,* **131**, 574-583.

Mackey, B. P., and T. N. Krishnamurti, 2001: Ensemble forecast of a typhoon flood event. *Wea. Forecasting,* **16**, 399-415.

Mapes, B. E., T. T. Warner, M. Xu, and D. J. Gochis, 2004: Comparison of cumulus parameterizations and entrainment using domain-mean wind divergence in a regional model. *J. Atmos. Sci.,* **61,** 1284-1295.

McBride, J. L., and R. Zehr, 1981: Observational analysis of tropical cyclone formation. Part II: Comparison of non-developing versus developing systems. *J. Atmos. Sci.*, **38**, 1132-1151.

Mellor, G. L., and T. Yamada, 1982: Development of a turbulence closure model for geophysical fluid problems. *Rev. Geophys. Space Phys.,* **20,** 851-875.

Meng, Z. and F. Zhang, 2007: Tests of an ensemble Kalman filter for mesoscale and regional-scale data assimilation. Part II: Imperfect model experiments. *Mon. Wea. Rev.,* **135,** 1403-1423.

Michaud, L. M., 1996: Comments on “Convective available potential energy in the environment of oceanic and continental clouds”. *J. Atmos. Sci.*, **53,** 1209-1211.

Mitchell, H. L., P. L. Houtekamer, and G. Pellerin, 2002: Ensemble size, balance, and model-error representation in an Ensemble Kalman Filter. *Mon. Wea. Rev.,* **130,** 2791-2808.

Molinari, J., D. Vollaro, and K. L. Corbosiero, 2004: Tropical cyclone formation in a sheared environment: A case study. *J. Atmos Sci.,* **61,** 2493–2509.

Montgomery, M. T., M. E. Nicholls, T. A. Cram, and A. B. Saunders, 2006: A vortical hot tower route to tropical cyclogenesis. *J. Atmos. Sci.,* **63,** 355-386.

NOAA SSD, cited 2008: Satellite services division – Home page. [Available online at http://www.ssd.noaa.gov/PS/TROP/genesis.html.]

Noh, Y., W.-G. Cheon, and S.-Y. Hong, 2003: Improvement of the K-profile model for the planetary boundary layer based on large eddy simulation data. *Bound.-Layer Meteor.*, **107**, 401-427.

Nolan, D. S., 2007: What is the trigger for tropical cyclogenesis? *Aust. Meter. Mag.,* **56**, 241-266.

Nolan, D S., E. D. Rappin, and K. A. Emanuel, 2007: Tropical cyclogenesis sensitivity to environmental parameters in radiate-convective equilibrium. *Quart. J. Roy. Meteor. Soc.*, **133,** 2085-2107.

Olson, D. A., N. W. Junker, and B. Korty, 1995: Evaluation of 33 years of quantitative precipitation forecasting at the NMC. *Wea. Forecasting*, **10**, 498-511.

Oouchi, K., H. Yoshimura, R. Mizuta, S. Kusunoki, and A. Noda, 2006: Tropical Cyclone Climatology in a Global-Warming Climate as Simulated in a 20 km-Mesh Global Atmospheric Model: Frequency and Wind Intensity Analyses. *J. Meteor. Soc. Japan,* **84,** 259-276.

Park, K., and X. Zou, 2004: Toward developing an objective 4DVAR BDA scheme for hurricane initialization based on TPC observed parameters. *Mon. Wea. Rev.,* **132,** 2054-2069.

Persing, J. and M. T. Montgomery, 2005: Is environmental CAPE important in the determination of maximum possible hurricane intensity? *J. Atmos. Sci.,* **62,** 542-550.

Pielke, Jr., R.A., J. Gratz, C. W. Landsea, D. Collins, M. Saunders, and R. Musulin, 2007: Normalized Hurricane Damages in the United States: 1900-2005, Natural Hazards Review, in review.

Raymond, D. J., C. Lopez-Carrillo, and L. L. Cavazos, 1998: Case studies of developing East Pacific easterly waves. *Q. J. R. Meteorol. Soc.,* **124,** 2005-2034.

Reasor, P. D., M. T. Montgomery, and L. F. Bosart, 2005: Mesoscale observations in the genesis of Hurricane Dolly (1996). *J. Atmos. Sci.,* **62,** 3151-3171.

Riehl, H., 1954: *Tropical Meteorology.* McGraw-Hill, 392 pp.

Reisner, J., R. J. Rasmussen, and R. T. Bruintjes, 1998: Explicit forecasting of supercooled liquid water in winter storms using the MM5 mesoscale model. *Quart. J. Roy. Meteor. Soc.,* **124B,** 1071-1107.

Ritchie, E. A., and G. J. Holland, 1997: Scale interactions during the formation of Typhoon Irving. *Mon. Wea. Rev.,* **125,** 1377-1396.

Rogers, R., S. Chen and J. Tenerelli, 2003: A numerical study of the impact of vertical shear on the distribution of rainfall in Hurricane Bonnie (1998). *Mon. Wea. Rev.,* **131,** 1577-1599.

Rotunno, R., and K. A. Emanuel, 1987: An air–sea interaction theory for tropical cyclones. Part II: Evolutionary study using a nonhydrostatic axisymmetric numerical model. *J. Atmos. Sci.,* **44,** 542-561.

Sippel, J. A., J. W. Nielsen-Gammon, and S. E. Allen, 2006: The multiple-vortex nature of tropical cyclogenesis. *Mon. Wea. Rev.,* **134,** 1796-1814.

Snyder, C., and F. Zhang, 2003: Assimilation of simulated Doppler radar observations with an ensemble Kalman filter. *Mon. Wea. Rev.,* **131,** 1663-1677.

Simpson, J., E. Ritchie, G. J. Holland, J. Halverson, and S. Stewart, 1997: Mesoscale interactions in tropical cyclone genesis. *Mon. Wea. Rev.,* **125,** 2643-2661.

Tory, K. J., N. E. Davidson, and M. T. Montgomery, 2007: Prediction and diagnosis of tropical cyclone formation in an NWP system. Part III: Diagnosis of Developing and Nondeveloping Storms. *J. Atmos. Sci.,* **64,** 3195-3213.

Tory, K. J., M. T. Montgomery, and N. E. Davidson, 2006a: Prediction and diagnosis of tropical cyclone formation in an NWP system. Part I: The critical role of vortex enhancement in deep convection. *J. Atmos. Sci.,* **63,** 3077-3089.

Tory, K. J., M. T. Montgomery, N. D. Davidson, and J. D. Kepert, 2006b: Prediction and diagnosis of tropical cyclone formation in an NWP system. Part II: A diagnosis of Tropical Cyclone Chris formation. *J. Atmos. Sci.,* **63,** 3091-3113.

Van Sang, N., R. K. Smith, and M. T. Montgomery, 2008: Tropical-cyclone intensification and predictability in three dimensions. *Quart. J. Roy. Meteor. Soc.,* **134,** 563-582.

Weber, H. C., 2003: Hurricane track prediction using a statistical ensemble of numerical models. *Mon. Wea. Rev.,* **131,** 749-770.

Weber, H. C., 2005a: Probabilistic prediction of tropical cyclones. Part I: Position. *Mon. Wea. Rev.,* **133,** 1840-1852.

Weber, H. C., 2005b: Probabilistic prediction of tropical cyclones. Part II: Intensity. *Mon. Wea. Rev.,* **133,** 1853-1864.

Webster, P. J., G. J. Holland, J. A. Curry, and H.-R. Chang, 2005: Changes in tropical cyclone number, duration, and intensity in a warming environment. *Science,* **309,** 1844–1846.

Williford, C. E., T. N. Krishnamurti, R. C. Torres, S. Cocke, Z. Christidis, and T. S. V. Kumar, 2003: Real-time superensemble forecasts of Atlantic tropical systems of 1999. *Mon. Wea. Rev.,* **131,** 1878-1894.

Wu, C.-C., K.-H., Y. Wang, and Y.-H. Kuo, 2006: Tropical cyclone initialization and prediction based on four-dimensional variational data assimilation. *J. Atmos. Sci.,* **63,** 2383-2395.

Zhang, F., 2005: Dynamics and structure of mesoscale error covariance of a winter cyclone estimated through short-range ensemble forecasts. *Mon. Wea. Rev.,* **133,** 2876-2893.

Zhang, F., C. Snyder, and R. Rotunno, 2002: Mesoscale predictability of the “surprise” snowstorm of 24-25 January 2000. *Mon. Wea. Rev.,* **130**, 1617-1632.

Zhang, F., C. Snyder, and R. Rotunno, 2003: Effects of moist convection on mesoscale predictability. *J. Atmos. Sci.,* **60**, 1173-1185.

Zhang, F., A. M. Odins, and J. W. Nielsen-Gammon, 2006a: Mesoscale Predictability of an Extreme Warm-Season Precipitation Event. *Wea. Forecasting*, **21**, 149-166.

Zhang, F., Z. Meng, and A. Aaksoy, 2006b: Tests of an ensemble Kalman filter for mesoscale and regional-scale data assimilation. Part 1: Perfect model experiments. *Mon. Wea. Rev.,* **134**, 722-736.

Zhang, F., N. Bei, R. Rotunno, C. Snyder and C. C. Epifanio, 2007: Mesoscale predictability of moist baroclinic waves: Cloud-resolving experiments and multistage error growth dynamics. *J. Atmos. Sci.*, **64**, 3579-3594.

Zhang, F., Y. Weng, J. A. Sippel and Z. Meng, 2008: Cloud-resolving hurricane initialization and prediction through assimilation of Doppler radar observations with an ensemble Kalman filter: Humberto (2007). *Mon. Wea. Rev.*, in press.

Zhang, Z., and T. N. Krishnamurti, 1999: A perturbation method for hurricane ensemble prediction. *Mon. Wea. Rev.,* **127**, 447-469.

VITA

Name: Jason Allen Sippel

Address: Department of Atmospheric Sciences
Texas A&M University
3150 TAMU
College Station, Texas 77843-3150

Email Address: jsipp@tamu.edu

Education: B.S., Atmospheric Sciences, Texas A&M University, 2002
M.S., Atmospheric Sciences, Texas A&M University, 2004
Ph. D., Atmospheric Sciences, Texas A&M University, 2008